

On the Reliability of Large-Eddy Simulation for Dispersed Two-Phase Flows

Vom Fachbereich Maschinenbau
an der Technischen Universität Darmstadt

zur

Erlangung des Grades eines Doktor-Ingenieurs (Dr.-Ing.)

genehmigte

D i s s e r t a t i o n

vorgelegt von

Dipl.-Ing. Desislava Nikolova Dimitrova

aus Haskovo (Bulgarien)

Berichterstatter:	Prof. Dr.–Ing. J. Janicka
Mitberichterstatter:	Prof. Dr.–Ing. P. Stephan
Tag der Einreichung:	04. Mai 2010
Tag der mündlichen Prüfung:	07. Juni 2010

Darmstadt 2011

D 17

Abstract

"On the Reliability of Large-Eddy Simulation for Dispersed Two-Phase Flows"

Desislava Dimitrova

This work deals with the numerical description of dilute polydispersed and turbulent two-phase flows. The method used to describe the two-phase flow is based on the EULERIAN-LAGRANGIAN approach. The carrier phase turbulent flow behavior is modeled utilizing Large Eddy Simulation (LES).

Most of the recent DNS investigations attempting to provide insight into particle-fluid interaction mechanisms are performed on simple, mostly homogeneous turbulent flows with very low REYNOLDS numbers. In contrast to this, LES is an opportunity to extend this studies to flows with significantly higher REYNOLDS numbers and to more complex geometries. Moreover, it is less restrictive to flows containing particles, larger than the KOLMOGOROV length scale.

The main objective of this work is to assess the state of the art capabilities of the two-phase LES and to identify weak points. Recommendations for additional model development for increasing the predictive ability are derived. The reliability of transfer of findings from one configuration to others is assessed. The conclusions are based on a systematic variation of relevant flow parameters, such as the REYNOLDS number and the STOKES number, so that a wide range of applications is covered. Therefore, several particle-laden flow configurations (two plane channel flows, a free jet and an evaporating spray at low temperature) are investigated.

Special attention is paid to the prediction of the particle preferential accumulation, because of its importance for simulations of mixing and combustion in turbulent flows. By performing a systematic variation of the particle STOKES number (here defined as the ratio of the particle time scale to the KOLMOGOROV time scale of the fluid) and the flow REYNOLDS number, it is observed that the maximum preferential accumulation occurs at a constant STOKES number and that this number does not depend on the REYNOLDS number. The magnitude of the accumulation, however, depends on the REYNOLDS number of the flow. The effect of an additional sub-grid stress dispersion model on the particle accumulation is found to be less pronounced for particles with characteristic time scales in the order of the KOLMOGOROV scale.

An additional issue of the standard EULERIAN-LAGRANGIAN method in LES context arises due to unphysical particle number densities, when preferential accumulation occurs. In this context, the usage of a model, accounting for natural dispersion due to particle collisions, is inevitable.

The influence of the dispersed phase on the fluid turbulence is considered in a wall bounded and a free shear flow. The improper modeling of the particle-wall interaction mechanisms can lead to different solutions for the particle velocity field and therefore to different levels of turbulence modification in the near wall region. It should be noted that these solutions are not necessarily unphysical, as some experimental investigations confirm. In contrast to this, the turbulence modification in a free shear flow is predicted very well, moreover, the prediction is found to be reliable for different mass loadings of the dispersed phase.

Within the scope of this work, a time efficient non-iterative Fractional Step procedure is applied for the pressure-velocity coupling of the carrier fluid governing equations. The coupling of the method with two-way coupled particle tracking simulations is validated successfully on configurations of isothermal flows and such with low density variation using experimental and DNS data.

Zusammenfassung

"On the Reliability of Large-Eddy Simulation for Dispersed Two-Phase Flows"

Desislava Dimitrova Die vorliegende Arbeit befaßt sich mit dünnen polydispersen turbulenten Mehrphasenströmungen. Das Verfahren, das zur Beschreibung der Zweiphasenströmung verwendet wird, basiert auf der EULER-LAGRANGE Methode. Die Turbulenz in der kontinuierlichen Phase wird mittels Grobstruktursimulation (Large Eddy Simulation, LES) modelliert.

Die meisten Untersuchungen mittels Direkten Numerischen Simulation neueren Datums, die einen Einblick in die Wechselwirkungsmechanismen zwischen Partikeln und umgebendem Fluid gewähren, beschreiben einfache Strömungen, sehr oft mit homogener Turbulenz und sehr niedrigen REYNOLDS Zahlen. Im Gegensatz dazu eröffnet LES die Möglichkeit diese Studien auf Strömungen mit wesentlich höheren REYNOLDS Zahlen und komplexeren Geometrien durchzuführen. Des Weiteren ist das Verfahren weniger restriktiv gegenüber Partikeln, die größer als die KOLMOGOROV Längenskalen sind.

Die wesentliche Zielsetzung dieser Arbeit ist es, den Stand des Wissens bezüglich Zweiphasen-LES einer kritischen Prüfung zu unterziehen und hierbei Schwachpunkte zu identifizieren. Es werden Vorschläge für die weitere Modellentwicklung gemacht, um die Eignung der Methode zur Vorhersage von mehrphasigen Strömungsphänomenen zu steigern. Die Zuverlässigkeit der Übertragung von Erkenntnissen von einer Konfiguration auf andere wird abgeschätzt. Die Schlussfolgerungen sind auf einer systematischen Parameterstudie der relevanten Strömungskenngrößen, wie der REYNOLDS Zahl oder der STOKES Zahl, begründet, und sichern somit einen großen Anwendungsbereich. Hierzu werden einige partikelbeladene Strömungskonfigurationen untersucht. Diese sind: zwei ebene Kanalströmungen, ein Freistrah und ein Freistrah mit verdampfenden Tröpfchen bei einer vergleichsweise niedrigen Temperatur.

Besondere Beachtung findet die Vorhersage der bevorzugten Akkumulation der Partikel in einer turbulenten Umgebung. Diese ist von besonderer Wichtigkeit bei Simulationen von Mischungs- und Verbrennungsvorgängen in turbulenten Strömungen. Mittels einer systematischen Parameterstudie der Partikel STOKES Zahl (hier definiert als das Verhältnis zwischen einer charakteristischen Partikelzeitskala und der KOLMOGOROV Zeitskala) und der REYNOLDS Zahl der Strömung, wird aufgezeigt, dass die maximale bevorzugte Akkumulation immer bei einer konstanten STOKES Zahl auftritt und dass diese STOKES Zahl nicht von der REYNOLDS abhängt. Die Intensität der Akkumulation wiederum ist eine Funktion von der REYNOLDS Zahl. Der Einfluss eines stochastischen sub-grid stress Dispersionsmodells auf die Partikelakkumulation ist bewertet und als unwesentlich für Partikel eingestuft, deren charakteristische Zeitskalen in derselben Größenordnung wie die KOLMOGOROV Zeitskala liegen.

Eine zusätzliche Schwierigkeit für die Zweiphasen-LES ergibt sich aus der Tatsache, dass die Standard EULER-LAGRANGE Methode unphysikalisch hohe Partikelanzahldichten in den Bereichen bevorzugter Konzentration zuläßt, da hier die Partikel-Partikel Kollision nicht berücksichtigt wird. Die Verwendung eines Modells das diese beschreibt, scheint unumgänglich.

Der Einfluss der dispersen Phase auf die Fluidturbulenz wird in einer geschlossenen und in einer freien Scherströmung betrachtet. Die ungenaue Modellierung der Partikel-Wand Interaktion in wandgeschlossenen Strömungen kann zu unterschiedlichen Lösungen für das Partikelgeschwindigkeitsfeld führen, und daher auch zu unterschiedlichen Intensitäten der Turbulenzmodifikation. Es sollte berücksichtigt werden, dass diese unterschiedlichen Lösungen keineswegs unphysikalisch sein müssen, wie auch experimentelle Untersuchungen zeigen. Im

Gegensatz dazu wird die Turbulenzmodifikation in der freien Scherströmung sehr genau vorhergesagt. Darüber hinaus wird gezeigt, dass diese Vorhersage auch für unterschiedliche Massenbelastungen der dispersen Phase zuverlässig ist.

Im Rahmen dieser Arbeit wird ein effizientes nicht iteratives Fractional Step Verfahren für die Druckgeschwindigkeitskopplung der kontinuierlichen Phase verwendet. Die Kopplung dieser Methode mit der Zwei-Wege gekoppelten EULER-LAGRANGE Methode ist erfolgreich für Konfigurationen isothermer Strömungen und solche mit kleiner Dichteänderung validiert, wobei sowohl experimentelle als auch DNS Daten als Referenz verwendet werden.

Acknowledgments

The present work is a result of my doctoral studies, conducted during the last three years, at the Institute of Energy and Powerplant Technology (EKT) at the Darmstadt University of Technology. This would not have been possible without the extensive professional and moreover personal support, I experienced from the head of the Institute Prof. Dr.-Ing. Johannes Janicka. His encouraging manner was always a source of motivation. I would like to express my grateful acknowledgment for his contribution to the present work. In addition I would like to honor his interest in the topic and for his guidance, which was always gladly accepted.

I wish to thank Prof. Dr.-Ing. Peter Stephan for taking over the review of this thesis.

I am especially indebted to Dr. Markus Braun, Team Leader Development at ANSYS Germany GmbH for his unfailing interest for my work. The numerous scientific discussions, far beyond the topic of the project, during the last three years contributed significantly to this work.

Additional professional and personal support I felt, especially in the early years of my employment in Darmstadt, from Prof. Dr. rer. nat. Amsini Sadiki, whose strong contribution is also gratefully acknowledged.

I would like to thank to all my colleagues at the institute for the warm working atmosphere during my time at the university. My thanks go to the development team of ANSYS Germany GmbH in Darmstadt for their kind support during the last three years.

I appreciate very much the effort and the time spent on revising this manuscript and the many useful advises from Boris Popoff and Dr. Lukas Schneider. For the linguistic revision I would like to thank Larissa Moore.

I would like to thank here also to my parents and my sister who gave me safety and support over the long distance and for their enthusiasm and curiosity for my work.

Finally I would like to thank to Boris Popoff for his patience especially during the time of writing this manuscript. In his calm and logical way he never failed to encourage me and keep my motivation even in difficult times.

Desislava Dimitrova
Darmstadt, May 2010

Eidestattliche Erklärung

Hiermit erkläre ich an Eides statt, dass ich die vorliegende Dissertation selbstständig verfasst und keine anderen als die von mir angegebenen Hilfsmittel verwendet habe. Ich erkläre außerdem, dass ich bisher noch keinen Promotionsversuch unternommen habe.

Desislava Dimitrova

Darmstadt, den 30. April 2010

For my sister, my mother and my father

And for B. $\epsilon < 0$

Contents

1	Introduction	1
1.1	State of the Art	2
1.2	Objectives	3
1.3	Outline	4
2	Theoretical Background	5
2.1	Turbulent Flows	5
2.1.1	Flow Classification	5
2.1.2	Physical Aspects	6
2.1.2.1	Governing Equations	6
2.1.2.2	Turbulence	9
2.1.3	Modeling Approaches for Turbulent Flows	11
2.1.3.1	Averaging Techniques	11
2.1.3.2	Direct Numerical Simulation (DNS)	12
2.1.3.3	Simulation Based on Statistical Averaging	12
2.1.3.4	Large Eddy Simulation (LES)	13
2.2	Multiphase turbulent flows	17
2.2.1	Flow Classification	17
2.2.2	Two-Phase Flow Dimensionless Parameters	19
2.2.3	Physical Aspects for Dilute Dispersed Flows	20
2.2.3.1	Equations of Motion for a Single Particle	21
2.2.3.2	Forces Acting on Particles	21
2.2.3.3	Energy transfer	25
2.2.3.4	Mass Transfer	26
2.2.3.5	Effect of Turbulence on the Dispersed Phase Motion	27
2.2.4	Modeling Approaches for Dilute Dispersed Flows	29
2.2.4.1	Major Concepts	29
2.2.4.2	Two-Way Coupling	31
2.2.4.3	Turbulent Dispersion	31
3	Numerical Methods	33
3.1	Numerical Methods for Continuous Flows	33
3.1.1	Discretization of the Governing Equations	33
3.1.2	Pressure-Velocity Coupling	37
3.1.3	Boundary conditions	40
3.1.4	Solving the Linear System	41
3.2	Numerical Methods for Discrete Phase	41
3.2.1	Integration of the Particle Equations of Motion	42

3.2.2	Boundary Conditions	44
4	Reference Configurations	45
4.1	Low Reynolds Number Particle Laden Channel Flow	45
4.1.1	DNS Setup	45
4.1.2	LES Setup	47
4.2	High Reynolds Number, Particle-Laden Channel Flow	49
4.2.1	Experimental Setup and Measurement Technique	50
4.2.2	Numerical Setup	52
4.3	Particle-Laden Jet	55
4.3.1	Experimental Setup and Measurement Technique	56
4.3.2	Numerical Setup	58
4.4	Evaporating Spray in a Confined Circular Chamber	61
4.4.1	Experimental Setup and Measurement Technique	62
4.4.2	Numerical Setup	64
5	Code Validation	70
5.1	Assessment of the single phase flow LES	71
5.1.1	Validation of the basic numerical setup	71
5.1.2	Influence of the pressure-velocity coupling	72
5.1.3	The unsteady inflow boundary condition	73
5.2	Assessment of the two-phase flow LES	75
5.2.1	Validation of particle tracking used with LES	75
5.2.2	Influence of the pressure-velocity coupling on LES using two-way coupling	75
5.2.3	Numerical versus real number of particles in the context of LES	77
6	Results and Discussion	79
6.1	Influence of Turbulence on Particle Motion	79
6.1.1	Particle Velocity Statistics	80
6.1.2	Particle Dispersion and Preferential Accumulation	92
6.1.2.1	Local Particle Accumulation	92
6.1.2.2	Mean Particle Concentration Profiles	99
6.2	Particle Influence on Turbulence	100
6.2.1	Turbulence Modification at a Constant Mean Flow	101
6.2.2	Turbulence Modification due to Mean Flow Variation	106
6.3	Evaporating Spray in a Confined Circular Chamber	110
6.3.1	Previous Large-Eddy Simulations	111
6.3.2	Present Results	111
6.3.2.1	Statistical Properties of the Gas Phase	112
6.3.2.2	Statistical Properties of the Dispersed Phase	113
7	Conclusion	116
	Bibliography	118

Nomenclature

Bold letters denote a vector. For vector and matrices the unit is component related.

Einstein's convention of summation is used upon the indexes i, j , and k .

* denotes equation dependent units.

Uppercase Latin letters		Unit
\dot{X}	species molar flux	mol/m ² /s
\boldsymbol{F}	force	N
\boldsymbol{I}_p	particle inertial moment	N
\boldsymbol{M}	torque	N
A	area	m ²
A	coefficient (Jacobi) matrix	kg/s
C	species concentration	—
C_A	added mass coefficient	—
C_B	Basset force coefficient	—
C_D	drag coefficient	—
C_f	convective flux	*
C_R	rotational coefficient	—
C_S	SMAGORINSKY constant	—
C_{LR}	rotational shear lift coefficient	—
C_{LS}	shear lift coefficient	—
D_f	diffusive flux	*
D_p	turbulent particle dispersion coefficient	m ² /s
D_α	mass diffusivity	m ² /s
D_{th}	thermal diffusivity	m ² /s
E	energy	kg m ² /s ²
$E_{kin,p}$	particle kinetic energy	m ² /s ²
G	filter function	m ^{−3}
I_{rel}	relative turbulence intensity	—
J_{ij}	generic scalar diffusive flux	kg/m ² /s
L	characteristic length	m
M_v	vapor mass flux	kg/m ² s
M_w	molar mass	kg/kmol
N	upper limit of the sum operator or sample number	—
R	universal gas constant	J/kg K
R_p	particle LAGRANGIAN velocity correlation	—
R_s	specific gas constant	J/kg/K
R_{ij}	velocity correlation function	m ² /s ²
S	source term	*

S_{ij}	strain rate tensor	1/s
T	temperature	K
T_{ij}	stress tensor	N/m ²
U	characteristic velocity	m/s
V	volume	m ³
X	species mole fraction	—
Y	species mass fraction	—

Lowercase Latin letters

Unit

\dot{m}	mass flow	kg/s
\mathbf{e}_i	Unit vector, $i = 1, 2, 3$	—
\mathbf{g}	gravitational acceleration	m/s ²
\mathbf{r}	vector in Cartesian space	m
\mathbf{x}, y, z	vector in Cartesian space	m
\mathbf{b}	source term vector	*
a	speed of sound	m/s
c_p	specific heat capacity	J/kg/K
d_p	particle diameter	m
e	coefficient of restitution	—
f	body force	N/m ³
g	gravity	m/s ²
h	channel half height	m
h	enthalpy	kgm ² /s ²
h_{lat}	specific latent heat	J/kg
h_{react}	specific heat of chemical reaction	J/kg
j_i^{sgs}	sub-grid scalar flux vector	*
k_{mass}	mass transfer coefficient	m/s
k_{th}	convective heat transfer coefficient	W/m ² K
l_0	integral length scale	m
l_{mean}	mean free path	m
m	mass	kg
n_i, \mathbf{n}	normal surface vector in Cartesian coordinates	—
n_p	particle number concentration	—
p	pressure	Pa
p_{sat}	saturation pressure	Pa
q_p	volumetric particle heat source	J/s
t	time	s
t_0	integral time scale	s
t_R	residence time	s
t_{eta}	KOLMOGOROV time scale	s
u, v, w	velocity components in Cartesian coordinates	m/s
u_η	KOLMOGOROV velocity	m/s
u_τ	friction velocity	m/s
u_τ	wall friction velocity	m/s
x, y, z	spatial (Cartesian) coordinates	m

Uppercase Greek letters

Unit

Δ	filter width	m
Γ	mixing (diffusion) factor	m ² /s
Ω	relative rotation	—

Lowercase Greek letters

Unit

α	under-relaxation factor	—
α_p	particle volume fraction	—
ϵ	turbulent kinetic energy dissipation rate	m ² /s ³
η	KOLMOGOROV length scale	m
κ	adiabatic exponent	—
κ_w	wavenumber	m ⁻¹
λ	thermal conductivity	W/m/K
μ	dynamic viscosity	kg/m/s
ν_t	kinematic turbulent viscosity	m ² /s
ν	kinematic viscosity	m ² /s
ϕ_p	particle mass loading	—
ψ	solution variable vector	*
ω_p	angular velocity vector	m/s
ψ	arbitrary scalar	—
ρ_{ij}	correlation coefficient	—
ρ	density	kg/m ³
τ	time	s
τ_{ij}^{sgs}	sub-grid-scale tensor	m ² /s ²
τ	characteristic time scale	s
τ_w	mean shear stress at wall	N/m ²
τ_w	mean wall shear stress	N/m ²
τ_{pL}	particle LAGRANGIAN integral time scale	s
ζ, ξ	random number	—

Indexes

1	wall next cell
α, β	index for arbitrary species
η	KOLMOGOROV scales
∞	free stream value
A	added mass
B	Basset
c	cell at channel centerline
CL	centerline
D	drag
e	eddy
f	carrier/fluid phase
f	face (of the computational cell)
h	enthalpy
i, j, k, l, m	natural numbers

Contents

LR	rotational lift
LS	shear lift
m	mass
n	node
nb	neighbor
op	operating (related to pressure)
P	pressure
p	particle phase
rel	relative
s	surface
t	turbulent
th	thermal
u	momentum
v	vapor

Superscripts

'	statistical fluctuation
"	statistical fluctuation
+	normalization using wall friction velocity and wall shear stress

Operators and Symbols

δ_{ij}	Kroneker delta
$\langle \cdot \rangle$	statistical mean value
$()$	REYNOLDS average
∂	partial differential operator
D	divergence operator
G	gradient operator
I	identity operator
$\widehat{()}$	filter
$\widetilde{()}$	FAVRE average
G	gravitation

Dimensionless Numbers

Kn	KNUDSEN number
Le	LEWIS number
Ma	MACH number
Pr	PRANDTL number
Re	REYNOLDS number
Re_p	particle REYNOLDS number
Re_τ	REYNOLDS number based on the wall friction velocity and the channel half height
Sc	SCHMIDT number
Sh	SHERWOOD number
St	STOKES number

Abbreviations

CDS	Central Difference Scheme
CV	control volume
DNS	Direct Numerical Simulation
DNS	direct numerical simulation
FS	Fractional Step Method
FSM	Fractional Step method
FVM	Finite Volume Method
ILU	Incomplete LU decomposition
LES	Large Eddy Simulation
LES	large-eddy simulation
nip, NiP	number (real particles) in parcel
PDA	Phase-Doppler Anemometry
PDE	partial differential equation
Pdf	probability density function
RANS	Reynolds Averaged Navier Stokes
RANS	Reynolds Averaged Navier-Stokes equations
RMS	root mean square
SIMPLE	Semi-Implicit Method for Pressure-Linked Equations
tke	turbulent kinetic energy
URANS	unsteady RANS

1 Introduction

When looking at the current status of power generation in industrial economies all over the globe, the necessity for an increased sustainability becomes evident. This is independent on the individual energy source or mechanism for power generation. It is obvious that, even if there are contradictory estimates of the available remaining resources for fossile fuels, these are finite. Neither oil and gas, nor coal are available for an unlimited period, considering the increasing energy demand and hence accelerating digging rates. Nuclear power generation depends on finite uranium deposits as well as on a speculation about the final storage for nuclear waste in form of burnt down nuclear fuel rods. A realistic timeline to be considered for this measures in the order of several hundred thousand years. So far, no single civilization on Earth lasted for such a period.

In addition to that, there is an enormous demand for mobility, not only in industrial economies. This demand is literally exploding with the emerging of newly industrializing countries like China, India or Brazil, who have together roughly 30 % of the world population and where the car is not adopted yet as an individual means of transport.

A strategy that aims to satisfy the growing demand for energy in a sustainable manner needs to be split into a short-term and a longer term policy. In the longer term the problem of finite resources for fossile fuel combustion and the nuclear waste storage need to be resolved, either by employing alternative energy sources or providing a reasonable resolution to the issues. In the meantime, research resources should be devoted to the exploration of possibilities to make the current technologies more effective. The potential of improving combustion technology, given the progress made in the recent years, seems to be strong. Not least, the computational fluid dynamics (CFD) methods adopted by the industry in the recent years had helped in achieving this. This is the case as well as in turbine manufacturing, as it is in the automobile industry. By reduction of the aerodynamic drag, that a car experiences, considerable savings are achievable. The optimization of the external shape of an automobile is of course secondary to the primary design draft. The evolution under the engine hood, in the area of internal combustion engines, has also made significant steps forward in terms of fuel efficiency. Ten years ago, direct fuel injection and the common rail injection system, were not widespread. Optimization of the evaporating spray flow inside the engine cylinders offers a strong potential for optimization. This is also the case for the combustion chambers of aircraft engines, as well as for stationary gas turbines, used for electric power generation. Simulation, provided it delivers reliable results in a reasonable turnaround time, can provide a significant cost reduction and acceleration of such developments. CFD methods, based on the NAVIER-STOKES equations have proven to be very successful in these areas and have become considerable chalengers to experimental investigations in wind tunnels and test stands, despite the fact that imperfect turbulence models, involving not always comprehensive simplifications, were used. The Large Eddy Simulation method seems to meet the requirement to provide an accurate solution in a reasonable timeframe and still not to be too extensive on the modeling side, so that the model errors are kept of lesser

significance. The application of Large Eddy Simulation to turbulent single phase flows and even to combusting flows has been explored in the recent past. The modeling of multiphase flow using LES is an area yet to be explored for applicability, reliability of predictions and for physical models required.

1.1 State of the Art

The LES technique for single phase flow simulations has made significant progress in feasibility and reliability in the last two decades. The rapid development of computational resources made this possible. The use of the method for simulation of simple flows and for validation (AGARD [1]) has now shifted toward realistic complex configurations of practical relevance (Axerio and Iaccarino [7], EACC [25]). The flexibility of the method, due to its reduced modeling effort, uncovers the potential for the usage of LES on a variety of flow configurations. The method has been successfully extended for the simulation of reacting flows, as reported by Pitsch [72] and Janicka and Sadiki [42] and other recent reviews. Although LES cannot yet maintain the status of an established, predictive tool for real industrial applications, the focus of development has been shifted for the recent years toward quality assessment of the method (Celik et al. [14], Freitag et al. [33]).

Attempts have been made to apply LES or DNS for the simulation of two-phase flows for the last decades as well. The majority of simulations, performed in the early 90^{ies}, were restricted to the usage of the EULERIAN-LAGRANGIAN approach and therefore applicable for dilute dispersed flows only (Squires and Eaton [100], Wang and Squires [112]). For the last ten years the development of LES for prediction of two-phase flows has pursued two main directions. Vance et al. [107], Kuerten and Vreman [45], Vreman et al. [110] and Fede and Simonin [28] conducted research work on fundamental understanding of phenomena in dilute two-phase flows and on the ability of LES to provide reliable results for these. The authors highlight deficits of the standard method with focus on the turbulent dispersion of small particles. This topic has a vital relevance, since the method can be applied to simulate a wide variety of combustion systems with liquid or solid fuels. Mixing processes are still an issue, even in single phase LES based simulations. The additional uncertainties introduced by the consideration of the reactive material as a separate (dispersed) phase can further violate the reliability of the simulation.

A second direction for the development of two-phase LES is outlined by Riber et al. [80], Apte et al. [3] and Boileau et al. [10]. The configurations they presented exhibit complex flow patterns, involving heat and mass transfer, and include swirling or recirculating flows as well as spray combustion. Considering the results reported, it is evident that such simulations lead to reasonable results in terms of statistical properties of the velocity fields for both phases and for the local particle diameter distribution. It should be noted, however, that the experimental data available, beyond velocity fields, is very rare.

The recent research work has shown that the EULERIAN-LAGRANGIAN approach, in the context of two-phase LES, can be applied successfully to simulate complex flow configurations. In addition, two-phase LES can be used as a validation tool, since often experimental investigations are rendered impractical by technical and financial challenges due to the complexity of the application. Boileau et al. [10] and Riber et al. [80] demonstrate an example for such a validation work. The EULERIAN-LAGRANGIAN method is applied as a reference case for the validation of an EULERIAN-EULERIAN technique in the context of LES.

Despite the ability of LES to deliver impressive qualitative results in the field of two-phase flows, there is still a lack of information concerning local and unsteady phenomena and interacting mechanisms between the phases, [28]. Due to the limited experimental data, many investigations are restricted to reference data from DNS, which are performed for flows at very low REYNOLDS number, [53, 55]. In contrast to the methods, developed for quality assessment of LES on single phase flows, the development on controlling mechanisms for quality estimation in the multiphase context is still at the very beginning.

1.2 Objectives

Applying the LAGRANGIAN method for simulation of dispersed two-phase flows brings several advantages: it handles in a natural way dispersed flows simply by solving equations of motion for a mass-point. Based on this method the particle motion as well as mass and energy exchange with the environment are resolved in time for each particle or droplet. This implies that configurations dealing with broad distributions of the particle (droplet) diameter such as sprays can be easily modeled. Furthermore, since every particle path is computed separately and therefore an additional information about the state of other particles is not of essential necessity, the LAGRANGIAN method allows for a fast computation of a large number of particles. In the context of dilute dispersed flows this method in combination with turbulence resolving models for the carrier phase such as DNS and LES represents a powerful tool for detailed investigation of multiphase flow phenomena and especially of mechanisms of phase interaction, [53].

Since the most DNS-related work that attempts to provide insight into particle-fluid interaction mechanisms is performed on simple, mostly homogeneous, turbulent flows with very low REYNOLDS numbers, the LES provides an opportunity to extend such studies to flows with relevance for technical applications, i.e. high REYNOLDS numbers and complex geometries.

Despite the enormous potential of the LAGRANGIAN method, the combination with LES opens diverse questions about the reliability of the simulations. Kuerten and Vreman [45] show for channel flow how disregarding the effect of unresolved turbulent structures on the particle motion leads to inaccurate flow prediction for heavy particles. In contrast to this Armenio et al. [5] and Pozorski and Apte [74] conclude based on their simulations of homogeneous turbulence that the unresolved structures show negligible effect on the particle motion for large particle-to-fluid density ratios. Since the different scientists apply different characteristic scales to describe a particular flow behavior, the comparison of configuration features and results becomes extremely difficult and sometimes even impossible. This is only one example that point out the difficulties for a third author who tries to analyse and compare available data from the literature.

This leads to the first main objective of the present work that utilizes the EULERIAN-LAGRANGIAN approach to describe dilute dispersed two-phase flows in the context of LES: the results of the numerical simulations of various (concerning REYNOLDS number and geometry) configurations performed here will be compared as far as possible using the same normalization and postprocessing techniques. Hence cross comparison and conclusions concerning simulation results will be possible upon a range of physical flow parameters such as STOKES and REYNOLDS number.

Second leading objective of this work is to assess the current capabilities of two-phase LES and to identify weak points. Recommendations for additional model development to increase

the predictive ability will be derived. The reliability of transferring findings from one configuration to another will be assessed. The conclusions are based on a systematic variation of relevant flow parameters, such as the REYNOLDS number and the STOKES number, so that a wide range of applications is covered. Several particle-laden flow configurations (two different plane channel flows, a free jet and an evaporating spray at low temperature) are investigated. The configurations are compared to available reference data from experiments and Direct Numerical Simulations with particle tracking.

One major part of this work is devoted on the prediction of turbulence-driven particle preferential accumulation, because of its importance in simulations of mixing and combustion in turbulent flows. The phenomenon of particle accumulation is investigated for different flow REYNOLDS numbers in a plane channel configuration. The findings are compared to previous investigations on particle accumulation in low REYNOLDS number flows. In addition, the influence of a stochastic dispersion model on particle accumulation and the velocity statistics of the dispersed phase are considered and analyzed. The investigations are span over range of particle classes with different STOKES numbers.

The modification of fluid turbulence due to the presence of particles is investigated in a wall bounded and in a free shear flow. The improper modeling of the particle-wall interaction mechanisms has a major role in the prediction of the flow velocity and the turbulence characteristics in the near wall region.

The last configuration investigated is an evaporating spray at low temperature conditions. Here, the ability of the two-phase LES to maintain reliability in complex flow situations is assessed.

1.3 Outline

The following chapter introduces the fundamental understandings about the two main topics in the scope of this work: turbulence in general and two-phase turbulent flows. Relevant physical aspects are summarized and discussed using their mathematical formulations. Based on them, different modeling concepts for turbulent single and two-phase flows are presented, with special attention on the particular models adopted for the simulations here.

The numerical treatment for the mathematical models applied is outlined in Chapter 3. Since efficiency in terms of time and computer resources are still critical parameters for advanced numerical simulations, some acceleration techniques are discussed in conjunction with the modeling concepts applied.

In Chapter 4 there is a summary of all simulated configurations. Beyond details regarding the reference configurations, the chapter contains a full list of all accomplished simulations with corresponding specifications. Part of the simulations are used to validate the program tool chosen to perform the computations. The results of this validation are presented in Chapter 5.

In order to evaluate the quality of the particular simulation technique, the discussion is divided into two main threads, based on the phase interaction mechanism. The first part of Chapter 6 is dedicated to the particle dispersion phenomenon. The second part of Chapter 6 addresses the influence of the secondary phase on the fluid turbulence. The findings are compared to the theoretical formulations.

Finally, conclusions and ideas on future development close this work in Chapter 7.

2 Theoretical Background

This chapter is a brief summary of fundamental physical aspects, with focus on turbulence in single and in multiphase flows. For every flow type, alternative, commonly used modeling concepts are examined, with an emphasis on the particular methods considered in this work. Special attention is paid to the interaction mechanisms between the different media within a multiphase flow.

2.1 Turbulent Flows

This chapter aims to present basic dimensionless numbers that are used to quantify flows in practical engineering and in theory. The fundamental governing equations describing the behavior of fluids and based on the continuum assumption are presented. Finally, a separate section is devoted to turbulence because of the fundamental relevance of turbulent flows for technical applications.

2.1.1 Flow Classification

To describe the majority of technical flows it is sufficient to perceive the fluid as a *continuum*, whose mass and momentum are conserved, instead of viewing it as a set of discrete molecules. This definition is part of the classification based on the KNUDSEN number (2.1), which is equal to the ratio of the mean free path of molecules λ to a characteristic length of the system L .

$$Kn = \frac{l_{mean}}{L} \quad (2.1)$$

The mean free path denotes the average distance that a molecule covers between two subsequent collisions. $Kn \geq 2$ denotes the limit for *free molecules* flow. In these conditions, it is necessary to trace the state of every single molecule. The limit $Kn \leq 0.01$ denotes a *continuum* flow. The global flow properties can be computed as an ensemble average over all molecules.

Another important physical property, used for fluid classification, is the viscosity. In fluids referred to as NEWTONIAN, the viscosity represents the constant proportionality factor between an arbitrary shear rate and the resulting shear stress. All gases and a large number of liquids can be approximated as NEWTONIAN fluids. In contrast to this, in non-NEWTONIAN fluids the shear stress resulting from a variable shear rate cannot be simply parameterized by the latter together with a proportionality constant. One possible classification of non-NEWTONIAN fluids is given by the categories BINGHAM plastic, pseudoplastic and dilatant fluids.

The MACH number Ma , Equation (2.2), provides a relation between the speed of sound a and a characteristic velocity of the system. a is a function of the fluid state, defined in terms of temperature T , universal gas constant R and the adiabatic exponent κ . According to their

MACH number, flows can be roughly split into incompressible, ($Ma < 0.3$), and compressible flows, ($Ma > 0.3$).

$$Ma = \frac{U}{a} = \frac{U}{\sqrt{\kappa RT}} \quad (2.2)$$

Above the value of 0.3 the amount of compressible effects is differently pronounced and so it is necessary to discern between sub-sonic ($Ma < 0.8$), trans-sonic ($0.8 < Ma < 1.2$) and super-sonic ($Ma > 1.2$) flows. In incompressible flows, the density of the fluid can be assumed to be independent of pressure change at constant temperature.

Within the scope of this work the fluid is assumed to be continuum, NEWTONIAN and incompressible.

One of the most commonly used dimensionless parameters is the REYNOLDS number Re , which represents the ratio of inertial to viscous forces, expressed by a characteristic flow velocity U and a length L and the kinematic viscosity ν of the fluid in Equation (2.3).

$$Re = \frac{UL}{\nu} \quad (2.3)$$

Re makes real life size test rigs obsolete due to the fact that real and scaled facilities based on the same REYNOLDS number behave similarly. The REYNOLDS number depicts the laminar-turbulent transition. For example, in pipe flow it is known that below $Re_D = UD/\nu < 2000$ the flow is laminar, above $Re_D > 5000$ it is fully turbulent if D is the pipe diameter, U the inflow velocity and ν the fluid viscosity. The transition happens in the region $2000 < Re_D < 5000$. Often the critical REYNOLDS is said to be $Re_{D,crit} \approx 2300$, although the exact transition point depends on many factors difficult to control, like the wall roughness is one.

For all the significant discrepancies between laminar and turbulent flow behavior, the physical and mathematical theories developed for laminar flows hold also for turbulent flows.

2.1.2 Physical Aspects

2.1.2.1 Governing Equations

Based on the classical continuum theory (see Truesdell and Toupin [104], Drew and Passman [24]), the conservation of mass and momentum is assumed. The mass and momentum transfer could be written in the form of partial differential equations for an arbitrary volume, as shown in Equation (2.4) and Equation (2.5).

$$\frac{\partial \rho}{\partial t} + \frac{\partial (\rho u_i)}{\partial x_i} = S_m \quad (2.4)$$

$$\frac{\partial (\rho u_i)}{\partial t} + \frac{\partial}{\partial x_j} (\rho u_j u_i) = \frac{\partial}{\partial x_j} T_{ji} + f_i + S_u \quad (2.5)$$

The first term on the left hand side of Equation (2.4) and Equation (2.5) denotes the time derivative, and the second term, the convective transport in the physical space. The indexes i, j, k represent the components of the vector \mathbf{x} in Cartesian coordinates. On the right hand side, the terms S_m and S_u represent mass and momentum source term respectively. f_i denotes a body force, such as the gravity force. The stress tensor \mathbf{T} of a NEWTONIAN fluid can be split into

pressure and viscous terms using known fluid properties, as written in Equation (2.6), where μ is the molecular viscosity, p is the pressure and δ_{ij} is the Kroneker symbol. The formulation of the momentum conservation equation for NEWTONIAN fluids and gases together with the mass conservation equation are known as the NAVIER-STOKES equations.

$$T_{ij} = \mu \left(\frac{\partial u_j}{\partial x_i} + \frac{\partial u_i}{\partial x_j} - \frac{2}{3} \frac{\partial u_k}{\partial x_k} \delta_{ij} \right) - p \quad (2.6)$$

At given temperature and pressure, the system of equations (2.4) and (2.5) together with appropriate boundary conditions, describes the velocity and pressure gradient fields of an arbitrary NEWTONIAN flow. The source terms in both equations need an explicit formulation as well. Flows with heat transfer allow for density and viscosity variation, which is not always trivial. For many applications with heat transfer, where the pressure fluctuation remains small compared to the absolute pressure, the latter can be approximated by a constant value, often referred to as *operating pressure* p_{op} . The ideal gas law can be rewritten as in Equation (2.7), where R_s is the specific gas constant. Consequently, the density can be parameterized by the temperature.

$$p_{op} = \rho R_s T \approx const \quad (2.7)$$

The consideration of heat transfer requires an appropriate description of the energy transfer process within the system. For the sake of simplicity, the transport of an arbitrary scalar ψ is considered first. It is possible to formulate a conservation equation similar to this for momentum or mass. Equation (2.8) outlines the general form of a scalar transport in the physical space. The left hand side expresses the change of ψ in time and the convective transport in space by a given velocity u . The right hand side depicts the diffusive flux J_{ij} and additional source term S_ψ closes the balance.

$$\frac{\partial(\rho\psi)}{\partial t} + \frac{\partial}{\partial x_i} (\rho u_i \psi) = \frac{\partial}{\partial x_i} J_{ij} + S_\psi \quad (2.8)$$

As mentioned above, in the case of energy transfer, the system of equations can be closed by an expression for the balance of the enthalpy h or the temperature T . In the template scalar Equation (2.8) ψ shall be replaced by the enthalpy h . Finally a formulation for the energy flux at the place of J_{ij} and a definition of the energy source term for S_ψ is needed. The energy flux consists basically of heat conduction and enthalpy diffusion due to species transport. The assumption that the enthalpy diffusion due to species transport follows FICK's law leads to the formulation for the enthalpy equation, as written in (2.9):

$$\frac{\partial(\rho h)}{\partial t} + \frac{\partial}{\partial x_i} (\rho u_i h) = \frac{\partial}{\partial x_i} \left(\frac{\lambda}{c_p} \frac{\partial h}{\partial x_i} \right) - \frac{\partial}{\partial x_i} \left(\sum_{\alpha=1}^{N_\alpha} h_\alpha \left(\frac{\lambda}{\rho c_p D_\alpha} - 1 \right) \rho D_\alpha \frac{\partial Y_\alpha}{\partial x_i} \right) + S_h \quad (2.9)$$

The specific heat capacity c_p of an arbitrary mixture can be computed by mass weighted summation of the specific heat capacities of all components N_α , as written in Equation (2.10). Y_α denotes the mass fraction of the mixture component α .

$$c_p = \sum_{\alpha=1}^{N_\alpha} c_{p,\alpha} Y_\alpha \quad (2.10)$$

The relation between the thermal and the mass diffusivity provided by the LEWIS number ((2.11)) can be used to simplify Equation (2.9) further.

$$Le_\alpha = \frac{\lambda}{\rho c_p D_\alpha} = \frac{D_{th}}{D_\alpha} \quad (2.11)$$

Assuming $Le_\alpha = 1$ leads to equal mass diffusion coefficients D_α . This approximation applies well to mixtures, where one component prevails over the remaining components in terms of mass fraction [69]. Moreover, for $Le_\alpha = 1$ the second term on the right hand side of Equation (2.9), denoting the species transport induced enthalpy diffusion, vanishes.

The source term S_h in Equation (2.9) consists of radiation heat together with the heat transfer between the different media. The radiation heat can be neglected for low temperature conditions and in a gaseous environment. The heat transfer between the media with different aggregate state is discussed in Section 2.2.3.3.

Considering the upper outlined assumptions for $Le_\alpha = 1$, the relation between thermal and mass diffusivity applies to $D_\alpha = D_{th} = \lambda/c_p/\rho$. Finally, the enthalpy Equation (2.9) can be simplified to (2.12).

$$\frac{\partial(\rho h)}{\partial t} + \frac{\partial}{\partial x_i}(\rho u_i h) = \frac{\partial}{\partial x_i} \left(\rho D_{th} \frac{\partial h}{\partial x_i} \right) + S_h \quad (2.12)$$

The PRANDTL number is the relation between the fluid viscosity and the thermal diffusivity. It is used to quantifies the proportion of the molecular stress transport to the amount of heat conduction. Pr for air and many other gases at ambient conditions has values around $0.7 - 0.8$.

$$Pr = \nu/D_{th} \quad (2.13)$$

The generic Equation (2.8) can be used to express species mass conservation in the system. Considering mixture of α species leads to $\alpha - 1$ individual conservation equations for all but one components. The overall mass conservation is enforced by the global continuity equation. Applied to species transport, the diffusive flux from Equation (2.8) arises basically from the diffusion due to mass concentration gradients (FICK's law) and the diffusion due to temperature gradients (SORET effect). Formulation of the source term consists in general of a chemical source, which depicts the rate of component generation or consumption due to chemical reactions, and an additive volumetric source, which accounts, for example, for the transfer from or toward another medium. The latter addresses a medium with a different aggregate state. Since the modeling and simulation of reactive flows are beyond the scope of this work, formulation of the chemical source term will not be discussed further. The equation for the mass conservation of the species α can be defined in terms of its mass fraction Y_α as follows in Equation (2.14).

$$\frac{\partial(\rho Y_\alpha)}{\partial t} + \frac{\partial}{\partial x_i}(\rho u_i Y_\alpha) = \frac{\partial}{\partial x_i} \left(\rho D_{\alpha\beta} \frac{\partial Y_\alpha}{\partial x_i} + \frac{D_{\alpha,th}}{T} \frac{\partial T}{\partial x_i} \right) + S_{Y_\alpha} \quad (2.14)$$

$D_{\alpha\beta}$ and $D_{\alpha,th}$ in Equation (2.14) are the binary diffusion coefficient of the species α in β and the thermal diffusion coefficient. The greek indexes denote the items of the species mixture. The mass diffusion in turbulent flows is known to prevail over the thermal diffusion, so the latter is often neglected. Furthermore, it is convenient to consider the relation existing between the mass diffusivity and the fluid viscosity, given by the SCHMIDT number (2.15).

$$Sc = \nu/D_{\alpha\beta} \quad (2.15)$$

For the SCHMIDT number of air in ambient conditions it is known to be 0.7.

2.1.2.2 Turbulence

Since the majority of technically relevant flows are turbulent, the development of mathematical approaches for fluid mechanics simulations is focused on them and the reliability of their prediction. A brief expose of major properties of turbulent flows follows. Several general terms related to turbulence and used for analysis throughout this work are defined.

The general picture of turbulent flow presumes an *irregular fluid motion with random variation in time and space*, i.e. turbulence is always unsteady, three-dimensional and stochastic. Due to its stochastic nature, turbulence characterization relies on statistical description of the various flow quantities, such as velocity components, pressure, temperature and so forth. It is common practice to split an arbitrary quantity ψ into a statistical mean value and an instantaneous deviation from the mean, also called the fluctuating part, (2.16).

$$\psi = \langle \psi \rangle + \psi' \quad (2.16)$$

The mean quantity, denoted by the angle brackets, presumes time or ensemble averaging¹. The splitting procedure is known as REYNOLDS decomposition and is used for the definition of the turbulent quantities below.

Before proceeding, it is worthwhile to recall the definition of two special cases of turbulent flows because of their importance to the following discussion.

Homogeneous turbulence: Statistical quantities, which are invariant to coordinate system translation, are homogeneously distributed. Concerning turbulent quantities, the restriction is made only for the fluctuating part of the velocity field, i.e. mean velocity gradients are not excluded by this definition.

Isotropic turbulence: Statistical quantities, which are invariant of any rotation or translation of the coordinate system, are isotropic.

Richardson [81] describes turbulence as an assemblage of coherent structures (eddies) with different size and velocity, and that larger eddies transfer energy toward smaller eddies. This process is known as *energy cascade*. The smallest eddies dissipate energy due to viscous friction. Kolmogorov [44] proposes his theory based on the energy cascade concept. According to this theory, in every turbulent flow with sufficiently high REYNOLDS number and a characteristic length scale l_0 of the large eddies, the statistical motion of eddies with characteristic size $l \ll l_0$ is isotropic, i.e. the hypothesis postulates that smaller eddies are independent of flow geometry and boundary conditions in contrast to the largest eddies l_0 . This statement is also experimentally proven for boundary layer turbulence. Experiments show that the rate of energy dissipation ϵ scales with u_0^2/t_0 , if u_0 and t_0 are characteristic velocity and time scales of the largest eddies, respectively. Additionally, for very small scales (eddies) the viscous friction within the eddy becomes significant and dominates the energy balance. For this, the 1st Kolmogorov's similarity hypothesis holds: For a high REYNOLDS number flow, the statistics of the small scale turbulent motions $l \ll l_0$ have a universal form, determined by ν and ϵ . Using this, the so called KOLMOGOROV length, velocity and time scales can be formulated ((2.17)).

$$\eta = (\nu^3/\epsilon)^{1/4} \quad u_\eta = (\epsilon\nu)^{1/4} \quad t_\eta = (\nu/\epsilon)^{1/2} \quad (2.17)$$

¹The reader will find a summary of averaging techniques in Section 2.1.3.

u_η is the circumferential velocity occurring. The term length scale could be related to the radius of certain coherent structure. The eddy time scale could be interpreted as the time for one eddy turn.

The last perception comes from the fact that the energy transfer \mathcal{T} from larger to successively smaller and smaller eddies should be of the order of $\mathcal{T} \approx u_0^2/t_0 = u_0^3/l_0$. It is obvious from the upper formulation that the energy transfer and the rate of dissipation are of the same order. This means that for a particular range of scales l with $l_0 \gg l \gg \eta$, the statistical motion of these eddies is universal and uniquely determined by the rate of dissipation and is independent of ν . The latter statement provides the second Kolmogorov's similarity hypothesis. It determines the region, also called the *inertial sub-range*, within the energy cascade where the eddy size is not relevant for the energy transfer. This region is enclosed by the largest turbulent structures on one side and by the smallest structures, for which viscous dissipation becomes relevant, on the other side.

Eddy length scales, as well as eddy time scales, can be estimated from the auto-correlation (two-point velocity correlation) $R(\mathbf{x}, t)$ in the physical space and time, as written in generalized form in Equation (2.18). Equation (2.19) represents the normalized form of the auto-correlation.

$$R_{ij}(\mathbf{x}, t) = \langle u'_i(\mathbf{x}, t) u'_j(\mathbf{x} + \mathbf{r}, t + \tau) \rangle \quad (2.18)$$

$$\rho_{ij}(\mathbf{x}, t) = \frac{R_{ij}(\mathbf{x}, t)}{\sqrt{\langle u_i'^2(\mathbf{x}, t) \rangle} \sqrt{\langle u_i'^2(\mathbf{x} + \mathbf{r}, t + \tau) \rangle}} \quad (2.19)$$

Time and space correlations are often built separately, i.e. $R_{ij}(\mathbf{x})$ or $R_{ij}(t)$ respectively. Finally, the integration of the correlation coefficient ρ_{ij} over \mathbf{x} and t , see (2.20), leads to the integral length scale tensor l_{ij} and the integral time scale tensor t_{ij} , which address the energy containing scales in the flow. For reasons of simplicity, homogeneous isotropic turbulence is considered, where the location x is arbitrary. Furthermore, it can be shown (Pope [73], p.192,196), that for isotropic flows the two-point correlation $R_{ij}(\mathbf{r}, t)$ is completely determined by the longitudinal correlation function $\rho_{11}(\mathbf{r}, t)$, with $\mathbf{r} = \mathbf{e}_1 r^2$.

$$l_{ij} = \int_{r=0}^{\infty} \rho_{ij}(\mathbf{r}, t) dr \quad t_{ij} = \int_{\tau=0}^{\infty} \rho_{ij}(\mathbf{r}, \tau) d\tau \quad (2.20)$$

For homogeneous isotropic turbulence, Equation (2.21) denotes the averaged integral length and time scales.

$$l_0 = \frac{1}{3} l_{ii} \quad t_0 = \frac{1}{3} t_{ii} \quad (2.21)$$

At this point, there is still a lack of information on the distribution of energy over the complete range of length scales. The representation of the velocity auto-correlation by FOURIER series provides more insight. The FOURIER transformation of the spatial auto-correlation, together with some restrictions on directional dependencies, results in the energy density spectrum $E(\kappa_w)$ over the wavenumber space. The wavenumber could be interpreted as an inverse length and expressed as $\kappa_w = 2\pi/l$. Large eddies therefore correspond to low wavenumbers and vice versa. Using logarithmic scales, a sketch of a theoretical energy spectrum is presented in Figure 2.1. The information contained in the Kolmogorov's hypothesis is demonstrated using the

² \mathbf{e}_1 is the unit vector.

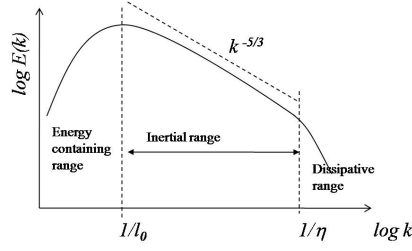


Figure 2.1: Theoretical energy spectrum in wavenumber space.

spectrum. As viewed, the energy containing eddies, addressed by l_0 are not the largest within the flow pattern. Within the inertial sub-range, the spectrum exhibits power-law behavior with an exponent of $-5/3$. This part of the spectrum is also known as the KOLMOGOROV spectrum. A similar representation is possible for the temporal auto-correlation. The resulting spectrum is in the frequency space. The frequency f then has the meaning of an angular velocity $f = 2\pi/t$. In other words, it represents the turnover time of an eddy of size l . It is measured in inverse time units.

2.1.3 Modeling Approaches for Turbulent Flows

As previously mentioned, the equations of mass (2.4) and momentum (2.5) conservation fully describe an arbitrary flow field. In the case of laminar flows, the system of equations together with meaningful boundary conditions has a unique solution. The difficulty in predicting turbulent flows arises from the stochastic nature of the turbulence. In this case, there is an infinite set of velocity and pressure fields, fulfilling Equations (2.4) and (2.5). Prediction of relevant engineering quantities is rendered extremely difficult. There are several ways to capture the instantaneous behavior. Without asserting completeness of all available modeling approaches, the following section consists of commonly used methods for mathematical modeling of turbulent flows.

2.1.3.1 Averaging Techniques

In conjunction with the different mathematical methods and the statistical evaluation of flow properties, it is useful to present several averaging methods first.

Considering a group of samples N related to certain property realizations ψ_i , the value $\langle\psi\rangle$ estimated from Equation (2.22) is the *ensemble* average over all realizations.

$$\langle\psi\rangle_N = \frac{1}{N} \sum_{i=1}^N \psi_i \quad (2.22)$$

For N samples of $\psi(t)$, where the quantity is sampled for a time period $t = T$, the integration over the sampling period leads to the *time*, or REYNOLDS average of ψ . The average is usually denoted with $\overline{(\cdot)}$.

$$\overline{\psi} = \langle\psi\rangle_T = \frac{1}{T} \int_{t=0}^T \psi(t) dt \quad (2.23)$$

Considering distribution of the property $\psi(\mathbf{x})$ in an arbitrary volume V , where \mathbf{x} denotes the position vector, the *volume* average is defined as (2.24)

$$\langle \psi \rangle_V = \frac{1}{V} \int_V \psi(\mathbf{x}) dV \quad (2.24)$$

2.1.3.2 Direct Numerical Simulation (DNS)

Direct Numerical Simulation (DNS) applies the solution of the full Navier-Stokes equations in the physical space. Since all turbulent motions of the eddies over the complete range of turbulent eddy scales are resolved in space and time, the necessity of modeling vanishes. On the other hand, the requirements for the fidelity of the numerical methods and computational resources are rising. In addition, from the definition of the KOLMOGOROV scales in (2.17) and the relation between the rate of energy dissipation ϵ and the large turbulent scales l_0 , the ratio between dissipation and integral length scales can be expressed in terms of the REYNOLDS number .

$$\frac{l_0}{\eta} \approx Re^{3/4} \quad (2.25)$$

It is obvious that the resolution of a three-dimensional domain scales with $Re^{9/4}$. The enormous computational effort limits the application of DNS to such low REYNOLDS number flows that the method is irrelevant from a practical point of view.

For the majority of DNS codes, the solution is based on Fourier-series expansion, which makes the application to complex geometries impossible. In addition, flows with chemical reaction, thus including phenomena such as species mixing, involve mixing scales typically much smaller than the KOLMOGOROV scales. Consequently, either the spatial resolution has to be increased or the use of complementary physical models is inevitable.

It is clear from Section 2.1.2.2 that turbulence is stochastic but correlated in time and space. Because of this, the definition of inlet boundary conditions implies an explicit knowledge of the velocity correlations of the flow. From various measurements in homogeneous and special cases of non-homogeneous turbulence, there is a certain database built on this point. This is not the case for complex flow geometries. Consequently, the application and reliability of DNS is limited to a few well-known configurations.

The main advantage of using DNS is the detailed representation of unsteady three-dimensional motion of the turbulent structures. The method allows for more details than experimental investigations and helps to visualize the connection between local unsteady phenomena and their effect on statistical flow properties. Hence, it remains an excellent tool for development and validation of turbulent models.

2.1.3.3 Simulation Based on Statistical Averaging

Again, due to its stochastic nature, turbulence can be captured by statistical description, using statistical moments of the flow quantities. The representation via moments can extend over several orders (i.e. mean, variance or auto-correlation, triple correlations) and a large number of turbulent models have been developed over the past years. Since turbulence modeling based on statistical averaging remains beyond the main scope of this work, only a brief description of its main features is given here. The books of Wilcox [114] and Pope [73] provide a comprehensive

overview and analysis. All models of this class make use of splitting the instantaneous quantity (velocity, pressure, scalar) into a mean and a fluctuating part, also referred to as REYNOLDS decomposition (Equation (2.16)). The class of models is therefore referred to as *Reynolds Averaged Navier-Stokes* or *RANS* models. Taking the mean of the continuity Equation (2.4) for isothermal turbulent flow leads to Equation (2.26)

$$\frac{\partial \bar{u}_i}{\partial x_i} = 0 \quad (2.26)$$

The incompressible NAVIER-STOKES equations have the following exact expression for the mean flow velocity (2.27).

$$\frac{\partial \bar{u}_i}{\partial t} + \frac{\partial}{\partial x_j} (\bar{u}_j \bar{u}_i - \overline{u'_j u'_i}) = -\frac{1}{\rho} \frac{\partial \bar{p}}{\partial x_i} + \frac{\partial}{\partial x_j} \left[\nu \left(\frac{\partial \bar{u}_i}{\partial x_j} + \frac{\partial \bar{u}_j}{\partial x_i} \right) \right] + \bar{f}_i + \bar{S}_{u_i} \quad (2.27)$$

The third term on the left hand side of Equation (2.27), $\overline{u'_i u'_j}$, is referred to as the REYNOLDS stress. The value of this term is a priori unknown. The basic system for a general flow problem with four governing equations contains more than four unknown quantities: there is a *closure problem*. Consequently, the turbulence modeling focuses on determining the REYNOLDS stress. An important assumption applied in the model derivation is that every unclosed term, containing moments of the quantity ϕ of order $\langle \phi \rangle^n$ can be expressed by known moments up to $(n - 1)^{th}$ order. The variety of models can be classified in terms of order of moments used to determine the REYNOLDS stress.

The majority of commonly used first order models take advantage of BOUSSINESQ's *eddy viscosity concept* proposed in 1877, assuming that the REYNOLDS stress term is similar to the viscous stress term and is proportional to the mean velocity gradient and the proportionality factor is called *turbulent* or *eddy* viscosity, ν_t . Second order turbulent closure models consider the evolution of the REYNOLDS stresses by solving transport equations for the tensor components. The equations contain further unclosed terms of higher order that need to be approximated.

Another crucial assumption of RANS models is that the turbulent flow features can be captured by a single characteristic turbulent length, l_t , and time, t_t , scale. The latter are derived from the turbulent kinetic energy k and its rate of dissipation ϵ , as written in Equation (2.28). The most widely used RANS models, the two-equation models like $k - \epsilon$ or $k - \omega$, on top of that presuppose local isotropy of the turbulent fluctuations, which could be guaranteed for flows at sufficiently high REYNOLDS numbers.

$$l_t = \frac{k^{3/2}}{\epsilon} \quad t_t = \frac{k}{\epsilon} \quad \text{where} \quad k = \frac{1}{2} \overline{u'_i u'_i} \quad (2.28)$$

The advantage of the RANS models is the relatively low computational cost. Since local instantaneous turbulent motions are not resolved, the models are able to predict only global turbulent quantities. In complex flow configurations with significant anisotropy of the flow or low REYNOLDS number regions, additional modeling effort is required.

2.1.3.4 Large Eddy Simulation (LES)

To some extent, the LES approach presented in this section represents a compromise between DNS and RANS models. Within the scope of this work, LES is applied for the fluid modeling

and therefore will be presented in more detail.

The major idea is that, in the best case scenario, all energy containing eddies exhibiting anisotropy properties shall be resolved, i.e. the evolution of their motions in time and space is explicitly computed. The small isotropic scales are approached via a turbulence model. Since the major information on complex flow patterns and unsteady effects is explicitly resolved, often a relatively simple, first order closure model is applied for the unresolved scales. The proposed idea allows for the use of coarser computational grids and larger time steps, hence, the computational cost compared to DNS is significantly reduced.

The splitting of the large from the small turbulent eddies is performed by applying a low-pass filter to the flow field. The filtering operation is defined as the convolution of a particular filter function $G(\mathbf{x}, \mathbf{y}, \Delta(\mathbf{x}))$ with the velocity, as shown in Equation (2.29). $\Delta(\mathbf{x})$ is the filter width, \mathbf{x} and \mathbf{y} are real vectors and V denotes the integration in the three dimensional real space \mathbb{R}^3 .

$$\tilde{u}_i = \int_V G(\mathbf{x}, \mathbf{y}, \Delta(\mathbf{x})) u_i(\mathbf{y}) d\mathbf{y} \quad (2.29)$$

Using the filtered velocity \tilde{u}_i in (2.30) the residual (sub-grid) part is expressed, here denoted with $(\cdot)''$.

$$u_i''(\mathbf{x}, t) = u_i(\mathbf{x}, t) - \tilde{u}_i(\mathbf{x}, t) \quad (2.30)$$

The filter length can be defined as the average box length of the numerical grid $\Delta = (\Delta x \Delta y \Delta z)^{1/3}$, as proposed by Schuman [90]. This form of the filter function is very specific for CFD application based on the Finite Volume Method³. The implicit consideration of the spatial discretization in the filter function definition is referred to as an *implicit* filtering and Equation (2.29) can then be written as follows:

$$\tilde{u}_i = \frac{1}{\Delta^3} \int_{z-\frac{1}{2}\Delta z}^{z+\frac{1}{2}\Delta z} \int_{y-\frac{1}{2}\Delta y}^{y+\frac{1}{2}\Delta y} \int_{x-\frac{1}{2}\Delta x}^{x+\frac{1}{2}\Delta x} u_i(x^*, y^*, z^*, t) dx^* dy^* dz^* \quad (2.31)$$

Equation (2.31) can be interpreted as the spatial average of u_i over the finite volume (see also the corresponding generalized expression in (2.24)).

The filtering operation on the mass (2.4) and the momentum (2.5) conservation equations for single phase, incompressible flows leads to the filtered set of conservation equations below, (2.32) and (2.33). It is taken into account that the applied *box* filter and the derivative operator commute. Furthermore, it is assumed that the error due to the approximation $\widetilde{\nu \partial_{x_i} u_i} \approx \tilde{\nu} \partial_{x_i} \tilde{u}_i$ is negligible.

$$\frac{\partial \tilde{u}_i}{\partial x_i} = 0 \quad (2.32)$$

$$\frac{\partial \tilde{u}_i}{\partial t} + \frac{\partial}{\partial x_j} (\tilde{u}_j \tilde{u}_i) = -\frac{1}{\bar{\rho}} \frac{\partial \bar{p}}{\partial x_i} + \frac{\partial}{\partial x_j} \left[\tilde{\nu} \left(\frac{\partial \tilde{u}_i}{\partial x_j} + \frac{\partial \tilde{u}_j}{\partial x_i} \right) - \tau_{ij}^{sgs} \right] + \tilde{f}_i \quad (2.33)$$

However, if flows with variable density are considered, it is common practice to introduce a density weighted filter operation, also known as FAVRE filtering (2.34).

$$\tilde{\psi} = \frac{\overline{\rho \psi}}{\bar{\rho}} \quad (2.34)$$

³The Finite Volume Method is described in Section 3.1

It utilizes the property that $\overline{\rho\psi'} = 0$ and consequently, the density-velocity correlations vanish in the filtered equations. The governing equations take the form of (2.35) and (2.36), if FAVRE-based filtering is applied.

$$\frac{\partial \bar{\rho}}{\partial t} + \frac{\partial \bar{\rho} \tilde{u}_i}{\partial x_i} = 0 \quad (2.35)$$

$$\frac{\partial \bar{\rho} \tilde{u}_i}{\partial t} + \frac{\partial}{\partial x_j} (\bar{\rho} \tilde{u}_j \tilde{u}_i) = -\frac{\partial \bar{p}}{\partial x_i} + \frac{\partial}{\partial x_j} \bar{\rho} \left[\tilde{v} \left(\frac{\partial \tilde{u}_i}{\partial x_j} + \frac{\partial \tilde{u}_j}{\partial x_i} - \frac{2}{3} \delta_{ji} \frac{\partial \tilde{u}_k}{\partial x_k} \right) - \tau_{ij}^{sgs} \right] + \bar{\rho} \tilde{f}_i \quad (2.36)$$

In both formulations of the momentum equation, (2.33) and (2.36), the unresolved or *sub-grid-scale stress* tensor τ_{ij}^{sgs} needs to be modeled. The sub-grid tensor arises from the filtering procedure of the convective term in the NAVIER-STOKES equations, (2.5). It can be further expressed by Equation (2.37).

$$\tau_{ij}^{sgs} = \widetilde{u_i u_j} - \tilde{u}_i \tilde{u}_j \quad (2.37)$$

Different authors postulate different requirements for the resolution of an LES. Pope [73] suggested that a reliable LES should resolve at least 80 % of the kinetic energy. Consequently and in contrast to the REYNOLDS stress tensor, the sub-grid stress term draws a significantly smaller amount of energy compared to the total kinetic energy in the flow. Secondly, according to the Kolmogorov's hypothesis, the scales represented by this term are nearly isotropic and homogeneous. The latter permits a significant simplification for the modeling of the sub-grid stress. The first model concepts proposed for the sub-grid stress rely on previous methods used for the development of RANS models. In the following, two of the commonly applied sub-grid stress models are presented. The latter are applied for the current simulations as well.

THE SMAGORINSKY MODEL [93] for τ_{ij}^{sgs} is based on the BOUSSINESQ-approximation, Hinze [38]. That means that the sub-grid stress behaves in the same way as molecular gradient diffusion. In the context of LES, the relation is expressed by an eddy viscosity ν_t and the gradient of the filtered velocity field, as shown in Equation (2.38). Since τ_{ij}^{sgs} can be further split into an isotropic and a deviatoric part, the isotropic part, $1/3 \delta_{ij} \tau_{kk}$, can be superimposed with the pressure gradient term in the NAVIER-STOKES equations and is not modeled. For convenience, the notation τ_{ij}^{sgs} is retained but only further addresses the deviatoric part of the sub-grid stress tensor.

$$\tau_{ij}^{sgs} = 2\nu_t \left(\widetilde{S_{ij}} - \frac{1}{3} \delta_{ij} \widetilde{S_{kk}} \right) \text{ where } \widetilde{S_{ij}} = \frac{1}{2} \left(\frac{\partial \tilde{u}_i}{\partial x_j} + \frac{\partial \tilde{u}_j}{\partial x_i} \right) \quad (2.38)$$

The eddy viscosity ν_t can be approximated via the PRANDTL mixing length hypothesis [75] in terms of a characteristic length scale and a velocity. The closest choice of an appropriate length scale is the filter width. Consequently, the eddy viscosity reads as Equation (2.39) with $|\widetilde{S_{ij}}| = \sqrt{2\widetilde{S_{ij}}\widetilde{S_{ij}}}$. The model constant varies in the literature in a wide range from 0.05 up to 0.5.

$$\nu_t = (C_S \Delta)^2 |\widetilde{S_{ij}}| \quad (2.39)$$

Due to the fixed value of the model constant, the eddy viscosity never vanishes. In flow regions with low turbulence or even at laminar conditions (which is the case in wall boundary layers) the model introduces an artificial diffusion.

THE DYNAMIC SMAGORINSKY MODEL is an alternative solution to the issue introduced due to the fixed model constant. Germano et al. [35] and Lilly [51] designed a procedure, that allows for dynamically estimating the SMAGORINSKY constant C_S from the local instantaneous filtered velocity. The theory takes advantage of Kolmogorov's similarity hypothesis for the inertial range of the energy spectrum. The approximation for the sub-grid stress is the same as for the Smagorinsky model. The general idea involves a second, explicit filtering operation (called test filter) of the already filtered equations with a test filter length $\hat{\Delta} = 2\Delta$. The second filtering operation on the convective term leads to a new sub-grid stress, here denoted as T_{ij} :

$$\widehat{\widetilde{u_i u_j}} = \widehat{u_i} \widehat{u_j} + \left(\widehat{\widetilde{u_i u_j}} - \widehat{u_i} \widehat{u_j} \right) = \widehat{u_i} \widehat{u_j} + T_{ij} \quad (2.40)$$

Moreover, the relation between the filtered grid sub-grid stress $\widehat{\tau_{ij}^{sgs}}$ and the sub-grid stress from the test filter T_{ij} , given by the GERMANO identity [35], can be estimated directly from the resolved scales (2.41):

$$L_{ij} = T_{ij} - \widehat{\tau_{ij}^{sgs}} = \widehat{u_i} \widehat{u_j} - \widehat{\widetilde{u_i u_j}} \quad (2.41)$$

As already mentioned, both grid and test sub-grid stress tensors, are approximated by Equation (2.38) and (2.39). The essential feature of the theory is, that the model constant C_S in the eddy viscosity equation (2.39) is independent from the filtering operation, hence, is the same for both sub-grid stress tensors. After substitution of the approximated sub-grid stress tensors in the Equation (2.41), the latter can be solved for the constant. The expression for the model constant obtained from a least square procedure [51] reads:

$$C_S^2 = \frac{M_{ij} (L_{ij} - 1/3 L_{kk} \delta_{ij})}{M_{ml} M_{ml}} \text{ where } M_{ij} = -2 \left(\widehat{\Delta^2 |\widehat{S_{ij}}| \widehat{S_{ij}}} - \Delta^2 |\widetilde{S_{ij}}| \widetilde{S_{ij}} \right) \quad (2.42)$$

The dynamically obtained constant varies in time and space over a wide range. Such variations occasionally lead to numerical instabilities. The common practice, supported by numerous investigations in that field, is to limit the values for C_S^2 . The lower limit is set to zero, since Equation (2.42) could also give negative results, which lead to unphysical, negative viscosity. The upper limit varies in the literature, but mostly it is around a value of 0.3.

Analogous to this, the filtering operation is performed for the scalar Equation (2.8). The filtering leads to an unknown scalar flux term j_ψ^{sgs} .

$$\frac{\partial(\bar{\rho}\widetilde{\psi})}{\partial t} + \frac{\partial}{\partial x_i} \left(\bar{\rho} \widetilde{u_i \psi} \right) = \frac{\partial}{\partial x_i} \widetilde{J_{ij}} + j_\psi^{sgs} + \widetilde{S_\psi} \quad (2.43)$$

The unresolved scalar flux is commonly approximated in a similar way to τ_{ij}^{sgs} according to Equation (2.38). That means that the eddy viscosity approach is applied together with the gradient flux assumption. The turbulent SCHMIDT number Sc_t is introduced, which is a relation between the turbulent viscosity ν_t and the turbulent diffusion coefficient D_t . Following this, the sub-grid scalar flux can be computed from (2.44).

$$j_\psi^{sgs} = - \frac{\nu_t}{Sc_t} \frac{\partial \psi}{\partial x_i} \quad (2.44)$$

2.2 Multiphase turbulent flows

At the beginning it is helpful to build a convention about the meaning of the term *phase* within the scope of this work. A *phase* is a continuous medium, where even the smallest portion, considered here, is much bigger compared to its building units - molecules or atoms. A *phase* is characterized by physical properties, such as density, viscosity, specific heat capacity, etc.. Phase interaction occurs due to transfer of momentum, energy and mass through the phase surface. The *phase* could have a solid, liquid or gaseous aggregate state.

Based on the upper definition one can define the term of *two-* or *multiphase* medium as an ensemble of two or more phases. Since in the current context at least one of the phases is a fluid, gaseous or liquid, it is further intuitive to identify the medium as a multiphase flow.

2.2.1 Flow Classification

The enormous combination variety of different media with different operation regimes makes the postulation of an universal theory for multiphase flow impossible. Common theories are valid for a certain type of flows only. Therefore the need of an appropriate multiphase flow classification is inevitable. One intuitive way to classify such flows is upon the aggregate state of their components as shown in table 2.1. Based on this classification, it is difficult to find out

Table 2.1: Classification of two-phase flows by aggregate state and their technical applications.

Phase Combination	Technical Application
Gas - solid	fluidized beds, pneumatic conveying, cyclone separation
Liquid - solid	hydraulic conveying, particle dispersion in stirred vessels
Gas - droplet	spray cooling, spray combustion
Liquid - droplet	mixing of immiscible liquids, liquid-liquid extraction
Liquid - gas	bubble columns, air-blast atomizer

consistent behavior similarity between flows belonging to the same class. So, for example, the flow in a bubble column is mainly driven by the density ratio of the components, and the flow in an air-blast atomizer is a result of the equilibrium between shear force and surface tension force at liquid surface within the nozzle. More successful classification in that sense seems to be the one, based on flow regime characteristics:

- separated flows: stratified, slug or film flows;
- dispersed flows: one or more phases are presented in form of discrete droplets, bubbles or particles and one continuous phase acts as a carrier for the rest;
- transient flows: transition between regimes, i.g. from liquid to vapor or liquid film atomization.

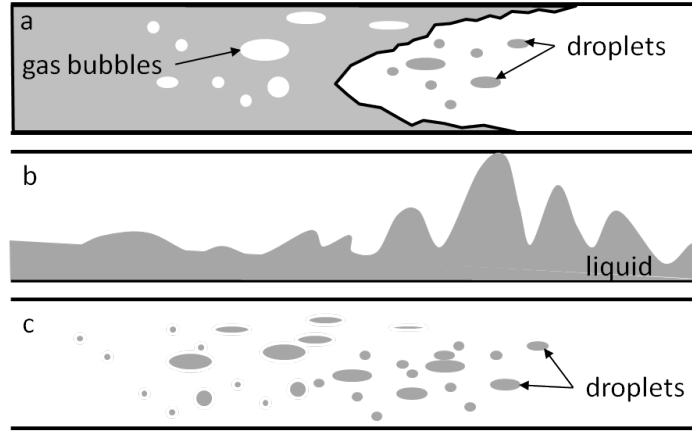


Figure 2.2: Classification of two-phase flows by regime: a) transient, b) separated and c) dispersed flow, [96].

Figure 2.2 gives an overview of possible realizations for two-phase flows based on the flow regime classification. Referring to Figure 2.2 it is obvious, that the volume occupied by both phases could be extremely different depending on the flow regime. This leads to the next important property in the context of multiphase flow - the phase volume fraction α for an arbitrary unit volume V . The formulation in terms of particle volume fraction is given in Equation (2.45). Similar information delivers also the particle number concentration, n_p , defined in Equation (2.46), if the size distribution is known.

$$\alpha_p = \frac{\sum_{i=1}^{N_p} V_{p,i}}{V} \quad (2.45)$$

$$n_p = \frac{\sum_{i=1}^{N_p} 1}{V} \quad (2.46)$$

In both equations, (2.45) and (2.46), N_p is the number of particles present, $V_{p,i}$ is the volume of the particle i and V is the flow volume considered. In the context of dispersed flows the continuous phase is often denoted as *carrier* or *primary* phase. Respectively the dispersed phase is termed as *secondary* phase.

Depending on the volume fraction of the secondary phase in a two-phase flow, the flow behavior is controlled by different physical phenomena. Referring to the dispersed phase volume fraction flows can be split in the following categories as proposed in Crowe et al. [16]:

- Dilute dispersed flows, if $\alpha_p \leq 5 \cdot 10^{-4}$,
 - Primary effect is the particle transport with the aim of the fluid, if $\alpha_p \leq 5 \cdot 10^{-7}$,
 - Active phase interaction from and toward the carrier fluid dominate,
- Dense dispersed flows,
 - Momentum exchange between phases together with particle collisions determine the flow behavior.

Within the first range the amount of the momentum transfer toward the carrier fluid is negligible and does not affect its statistical properties. With increasing volume fraction, the effect of the secondary phase cannot be further omitted. In addition to the fluid influence on the particle

motion, particles determine the fluid motion. Finally in dense two-phase flows the particle-particle interactions contribute significantly to the flow behavior, moreover, the particle-particle correlation of motion increases.

The threshold values of the volume fraction denoted above give only an approximate estimate for the range of the classes. Experimental investigations presented by Kulick et al. [48] in a channel flow and later by Fessler et al. [30] in a backward facing step show clearly that, in addition to the volume fraction of the dispersed phase, the particle density has a significant effect on the feedback amount from the dispersed toward the carrier phase. The authors assert, that even for the particle volume fraction above 10^{-5} the influence of the particles on the carrier flow is negligible for certain densities of the particles. On the other hand, within the high volume fraction range, collision dominated behavior loses relevance with increasing particle diameter, because of the decreasing free path between potential colliding particles.

Within the scope of this work the investigations are restricted to dilute dispersed two-phase flows with bidirectional momentum exchange together with mass and thermal energy transfer.

2.2.2 Two-Phase Flow Dimensionless Parameters

The current section is devoted to several dimensionless quantities, vital for the characterization of two-phase flows.

One of the parameters - the volume fraction α_p - has been introduced in the previous section because of its relevance to the classification of dispersed two-phase flows. As already mentioned, this parameter gives only a rough estimate of the expected flow behavior and acting forces. Another parameter is the STOKES number, St , defined in Equation (2.47).

$$St = \frac{\tau_p}{\tau_f}, \quad (2.47)$$

τ_p is the particle response time and τ_f is a characteristic fluid time scale. The STOKES number St quantifies the response of the particle in terms of acceleration to a certain fluid velocity change within a characteristic time. Snyder et al. [94] defines the particle response time for STOKESIAN flow as a function of particle diameter and density together with flow density and kinematic viscosity, Equation (2.48).

$$\tau_p = \frac{1}{36\nu_f} d_p^2 \left(1 + \frac{2\rho_p}{\rho_f} \right) \quad (2.48)$$

τ_p represents the time, which a particle with zero velocity, released into a viscous fluid with velocity \mathbf{u}_f , needs to accelerate up to 63.2% of the flow velocity. In gas-solid or gas-liquid flows the ratio $\frac{2\rho_p}{\rho_f}$ is very high, and Equation (2.47) is reduced to its more popular form given in Equation (2.49).

$$\tau_p = \frac{\rho_p d_p^2}{18\mu_f} \quad (2.49)$$

According to the definition, for $St \rightarrow 0$ particles behave as tracer in the fluid. They follow the flow motion nearly without any delay. $St \rightarrow \infty$, in the case of heavy or big inertial particles, indicates that particle motion remains independent from the fluid motion. There is a broad range between both limits, for which particles partially respond to certain fluid time scales. It

has been observed that around $St \approx 1$ particles build cluster structures and lose their homogeneous distribution. This effect is known as *preferential concentration* and has been broadly investigated ([31], [53], [70], [45]). This very specific behavior will be discussed in detail later in a separate section.

In the context of two-phase flows a further relevant parameter is the so called *particle* REYNOLDS number,

$$Re_p = \frac{d_p \mathbf{u}_{rel}}{\nu_f}, \quad (2.50)$$

which describes the flow around a particle. Equation (2.50) gives the expression for the particle REYNOLDS number for spherical particles. The characteristic length scale is the particle diameter and the characteristic velocity is the relative velocity between particle and surrounding fluid, \mathbf{u}_{rel} .

In many engineering applications the particle mass loading ϕ_p is used to parameterize the flow conditions. It is a global parameter and is defined as the ratio of the total particle mass flow rate to the total mass flow rate of the carrier fluid, see Equation (2.51).

$$\phi_p = \frac{\dot{m}_p}{\dot{m}_f} \quad (2.51)$$

Mass transport due to evaporation between the phases is partially controlled by gradients in the concentration of the evaporating species, i.e. it depends on the convective transport within the fluid. The SHERWOOD number (Equation (2.52)), is the ratio of the convective mass transfer, approximated with a characteristic flow scale L and a mass flux coefficient k_{mass} , to the mass diffusion coefficient $D_{\alpha\beta}$.

$$Sh = \frac{k_{mass} L}{D_{\alpha\beta}} \quad (2.52)$$

2.2.3 Physical Aspects for Dilute Dispersed Flows

In general the transport equations discussed in Section 2.1.2.1 apply to the dispersed phase in the same way as to the carrier phase. The transport phenomena due to convection and diffusion *within* a single droplet obey the same physical laws as these related to the carrier phase. Only in the case of solid particles the convection term in the momentum equation, 2.5, and in the scalar transport equation 2.8 becomes obsolete.

As mentioned above, in dilute two-phase flows the volume fraction of the dispersed phase is very low and furthermore it implies that the droplets or particles are much smaller compared to the dimension of the technical apparatus. In other words, the integral length scales of the carrier phase, which are mainly determined by the technical geometry, and the length scale of the particles, such as particle diameter, differ by several orders of magnitude. Therefore the overall transport of mass, momentum and energy within the dispersed phase is in general much faster compared to this within the carrier fluid.

Concerning the phase interaction the exchange of momentum, energy and mass can be expressed simplified as shown in Figure 2.3. A discrete particle experiences the external forces from the carrier fluid and the exchange of mass and energy is described by fluxes through the particle surface. A more extended discussion on the phase interaction and its interpretation in terms of physical models is presented in the following part of this section.

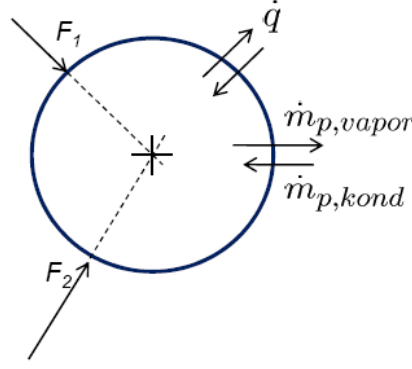


Figure 2.3: Sketch of mass, momentum and energy transfer between a single particle and the surrounding fluid.

2.2.3.1 Equations of Motion for a Single Particle

In general the motion of a single particle within the LAGRANGIAN framework can be described by ordinary differential equations accounting for particle position (2.53) and velocity change in time. These are driven by the particle linear ((2.54)) and angular ((2.55)) accelerations. As obvious from Equation (2.53), the particle position \mathbf{x}_p can be obtained from integration of the particle velocity \mathbf{u}_p in time. The particle velocity on its side, linear, \mathbf{u}_p , and angular, $\boldsymbol{\omega}_p$, is a function of the acting forces \mathbf{F}_i and the torque \mathbf{M}_i respectively.

$$\frac{d\mathbf{x}_p}{dt} = \mathbf{u}_p \quad (2.53)$$

$$m_p \frac{d\mathbf{u}_p}{dt} = \sum \mathbf{F}_i \quad (2.54)$$

$$I_p \frac{d\boldsymbol{\omega}_p}{dt} = \sum \mathbf{M}_i \quad (2.55)$$

2.2.3.2 Forces Acting on Particles

The knowledge of all forces acting on an individual particle is required to integrate Equation (2.54). These appear on the right hand side of the equation. Depending on the flow boundary and operating conditions various forces can act on a particle. From the overall variety only few forces are of significant magnitude and need to be considered for the integration of the particle equation motion.

Drag Force

The force acting on a particle in a uniform pressure field without acceleration of the relative velocity between particle and fluid is known as the steady state drag force, Equation (2.56).

$$F_D = \frac{1}{2} \rho_f C_D A_p (\mathbf{u}_f - \mathbf{u}_p) \quad (2.56)$$

Of vital importance here, are the relative velocity between particle and surrounding fluid ($\mathbf{u}_f - \mathbf{u}_p$) together with the cross section of the particle A_p , normal to the relative velocity vector. The relative velocity, together with the no-slip condition for the fluid velocity at the particle surface,

impose the development of a boundary layer around the particle. Since this remains unresolved by the upper definition for the drag force, the proportionality coefficient C_D , often referred to as *drag coefficient*, accounts for effects arising from it, based on empirical correlations. A summary of experimental works on measuring the drag on a sphere is in Schlichting and Gersten [89]. Crowe et al. [16] confirm the significance of the boundary layer state (turbulent or laminar) for the drag force as shown in Figure 2.4. Within the region $Re_p < 0.5$, known as Stokes region,

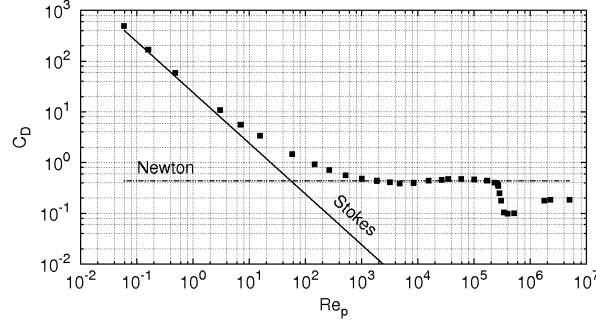


Figure 2.4: Drag coefficient on a sphere as a function of the particle REYNOLDS number.

no flow separation is observed and the drag coefficient corresponds to the relation proposed by Stokes [101], (2.57).

$$C_D = \frac{24}{Re_p} \quad (2.57)$$

For $0.5 < Re_p < 10^3$ with increasing REYNOLDS number the inertial force influence increases. This results in flow separation around the sphere. Above $Re_p \approx 10^3$ the drag coefficient has approximately a constant value of a 0.44 and the flow regime is known as NEWTON-regime. Finally above the critical $Re_p > 2.5 \cdot 10^5$ the coefficient decreases significantly. The effect corresponds to the transition from laminar to turbulent boundary layer around the particle. For typical engineering applications the particle REYNOLDS number seldom exceeds this critical value. Additional effects, such as a turbulent carrier fluid, particle surface roughness, etc., have the effect of shifting the above discussed regions toward lower particle REYNOLDS numbers. Nevertheless, such dependencies are not necessarily linear and in addition not all the effects are investigated in detail.

Based on the experimental results several empirical correlations have been developed to account for changes in the flow characteristics around the particle. One of the most popular empirical approximations for C_D has been proposed by Schiller and Naumann [88]. This mainly extends the STOKES correlation up to $Re_p < 1000$, Equation (2.58).

$$C_D = \frac{24}{Re_p} (1 + 0.15 Re_p^{0.687}) \quad (2.58)$$

For the range $10^3 < Re_p < 3 \cdot 10^5$ the drag coefficient is approximated as a constant $C_D = 0.44$. A more exact approximation of the C_D -curve progression is the polynomial function of Morsi and Alexander [62] according to Equation (2.59). The three constants a , b , c have been adjusted for eight subregions of the particle REYNOLDS number up to $Re_p < 5 \cdot 10^4$.

$$C_D = a + \frac{b}{Re_p} + \frac{c}{Re_p^2} \quad (2.59)$$

For the coefficients a , b and c the following relations hold:

$$a_1, a_2, a_3 = \begin{cases} 0, 18, 0 & 0 < Re < 0.1 \\ 3.690, 22.73, 0.0903 & 0.1 < Re < 1 \\ 1.222, 29.1667, -3.8889 & 1 < Re < 10 \\ 0.6167, 46.50, -116.67 & 10 < Re < 100 \\ 0.3644, 98.33, -2778 & 100 < Re < 1000 \\ 0.357, 148.62, -47500 & 1000 < Re < 5000 \\ 0.46, -490.546, 578700 & 5000 < Re < 10000 \\ 0.5191, -1662.5, 5416700 & Re > 10000 \end{cases} \quad (2.60)$$

Lift Force

Particle as well as fluid rotation induces a force transverse to the particle velocity vector, called lift force. In addition, a particle crossing regions with a high fluid velocity gradient, experiences lift in direction toward the positive gradient. The bigger the particle, the higher the shear lift force F_{LS} acting on it.

$$F_{LS} = \frac{\rho_f}{2} \frac{\pi d_p^2}{4} C_{LS} d_p ((\mathbf{u}_f - \mathbf{u}_p) \times \boldsymbol{\omega}_f) \quad (2.61)$$

The three-dimensional rotation of the fluid in Equation (2.61) is obtained using Equation (2.62).

$$\boldsymbol{\omega}_f = \nabla \times \mathbf{u}_f \quad (2.62)$$

The analytical derivation for the shear lift force F_{LS} , proposed by Saffman [85], is limited to a low shear REYNOLDS number⁴. Therefore, similar to the drag force formulation from Equation (2.61), the shear lift coefficient C_{LS} , proposed by Mei [60], accounts for higher particle shear REYNOLDS numbers. The shear lift coefficient is a function of both particle and shear REYNOLDS number.

$$\frac{C_{LS}}{C_{LS, Saff}} = (1 - 0.3314 \beta^{1/2}) \exp\left(\frac{-Re_p}{10}\right) + 0.3314 \beta^{1/2}, Re_p \leq 40 \quad (2.63)$$

$$= 0.0524 (\beta Re_p)^{1/2} \quad (2.64)$$

In above equation for the factor β the relation holds $\beta = 0.5 \frac{Re_S}{Re_p}$.

On the other hand particle rotation induces deformation of the flow field due to shifting of the stagnation points on the particle. The resulting rotational lift force is called MAGNUS force and acts transverse to the particle velocity vector. The primary expression of the force, derived by Rubinow and Keller [82], has been later modified by Crowe et al. [16], Equation (2.65), to account for higher particle Re_p and particle rotation Re_R ⁵ REYNOLDS numbers,

⁴Shear REYNOLDS number: $Re_S = \rho_f d_p^2 |\boldsymbol{\omega}_f| / \mu_f$.

⁵ $Re_R = \rho_f d_p^2 |\boldsymbol{\Omega}| / \mu_f$

$$C_{LR} = f(Re_p, Re_R).$$

$$F_{LR} = \frac{\rho_f \pi d_p^2}{2 \cdot 4} C_{LR} |\mathbf{u}_f - \mathbf{u}_p| \frac{|\boldsymbol{\Omega} \times (\mathbf{u}_f - \mathbf{u}_p)|}{|\boldsymbol{\Omega}|} \quad (2.65)$$

with

$$\boldsymbol{\Omega} = 0.5 \nabla \times \mathbf{u}_f - \boldsymbol{\omega}_p \quad (2.66)$$

being the local relative rotation of the fluid. It is obvious that for $\boldsymbol{\Omega} = 0$ the rotational lift becomes zero. The following correlation is often used to approximate C_{LR} for $Re_p < 140$:

$$C_{LR} = 0.45 + \left(\frac{Re_R}{Re_p} - 0.45 \right) \exp(-0.05684 Re_R^{0.4} Re_p^{0.3}) \quad (2.67)$$

Basset Force

To obtain the so-called Basset force one needs to integrate in time from the beginning of the particle motion. The force accounts for variations of the particle acceleration in time, i.e. the Basset force accounts for the particle *memory* along its path.

$$F_B = 9 \sqrt{\frac{\rho_f \mu_f}{\pi}} \frac{m_p}{\rho_p d_p} C_B \left\{ \int_0^t \frac{d}{dt} (\mathbf{u}_f - \mathbf{u}_p) \frac{d\tau}{(t - \tau)^{1/2}} + \frac{(\mathbf{u}_f - \mathbf{u}_p)_0}{t^{1/2}} \right\} \quad (2.68)$$

The second term in Equation (2.68) denotes the initial acceleration. The coefficient C_B is estimated from the experiment of Odar and Hamilton [64]. It corrects the force for higher particle REYNOLDS numbers.

Although the Basset force is often neglected because of its time consuming integration (Sommerfeld [95]), Hjelmfeld and Mockros [39] showed for a particle in a forced oscillating flow field that the Basset force can have a significant effect on the particle motion.

Body Forces

The only relevant body force within the current scope is the gravity force, which becomes important with increasing difference between the dispersed and the carrier phase densities.

$$F_G = m_p \mathbf{g} \quad (2.69)$$

For very small particles, with a diameter in order of $d_p < 1 \mu m$, temperature gradients or such in the turbulence intensity become also relevant. These additional body forces are known as the thermophoretic and the turbophoretic force respectively.

Pressure Gradient Force

The local pressure gradient in the flow induce a force collinear to it. The net pressure force acting on a particle is given by

$$F_P = \int_{V_p} -\nabla p dV \quad (2.70)$$

An expression for pressure gradient could be easily derived from the NAVIER-STOKES equation in terms of velocity convection and viscous diffusion. This procedure is omitted here since the relevance of the force remains limited for the case that fluid density is comparable to the particle density or higher.

Added Mass Force

Similar to the pressure gradient force, the added mass force becomes significant for density ratios of $\rho_f/\rho_p \approx 1$ or higher. This is the case in bubbly flows for example. The added mass force represents the momentum consumed for acceleration of the surrounding fluid caused by the no-slip condition at the particle surface, Equation (2.71).

$$F_A = \frac{1}{2} C_A m_p \frac{\rho_f}{\rho_p} \frac{d(\mathbf{u}_f - \mathbf{u}_p)}{dt} \quad (2.71)$$

The coefficient C_A is an empirical quantity ([64]) and accounts for flow regime around the particle that is beyond the STOKES -flow. For practical applications often a value of $C_A = 0.5$ is assumed.

Torque

A rotating particle experiences a torque due to friction with the surrounding fluid. The equation was developed by Rubinow and Keller [82] for a rotating particle in stagnant flow for low particle rotational REYNOLDS numbers of $Re_R < 32$. Later experimental and numerical works ([87], [19]) allow for accurate estimation of the torque up to $Re_R < 1000$.

$$\mathbf{M} = \frac{\rho_f}{2} \left(\frac{d_p}{2} \right)^5 C_R |\boldsymbol{\Omega}| \boldsymbol{\Omega} \quad (2.72)$$

The rotational coefficient for small Re_R is approximated as $C_R = 64\pi/Re_R$. The fluid rotation $\boldsymbol{\Omega}$ is estimated as given in Equation (2.66).

Importance of the different forces

From the formulation of the forces presented above it is obvious that depending on the particle to fluid density ratio or the particle diameter, some forces can be up to several orders of magnitude higher than others. Hjelmfelt and Mockros [39] and Elghobashi and Truesdell [26] performed an analysis to quantify these forces. According to these authors drag, buoyancy and Basset force have the strongest contribution to the particle motion in case of $\rho_p/\rho_f \gg 1$. Furthermore, the Basset force is at least one order of magnitude lower than the drag force. For this reason it is a common practice to consider solely drag and buoyancy effects for the analysis of solid and liquid particle–gas flows .

2.2.3.3 Energy transfer

The governing transport equations for the energy can be imposed from different perspectives of the droplet-gas system. Considering droplets or bubbles, the momentum, mass and energy

transfer within the particle can be expressed by the governing equations already discussed in in Section 2.1.2.1. Often the thermodynamical reality within very small particles is either approximated by empirical correlations or an uniform distribution of the particle internal properties is assumed. This results in several simplifications from mathematical point of view. A spherically symmetric droplet heating and vaporization consider only radial convection. A generalized form of the energy transfer between particle and the environment is given by the ordinary differential equation for the particle temperature T_p (Equation (2.73)). It is further assumed the temperature within the particle is homogeneously distributed.

$$m_p c_p \frac{dT_p}{dt} = k_{th} A_p (T_\infty - T_p) + q_p + \frac{dm_p}{dt} h_{lat} + \frac{dm_p}{dt} h_{react} \quad (2.73)$$

c_p here denotes the specific heat capacity of the particle, k_{th} is the heat transfer coefficient between particle and continuous phase, T_∞ is the local bulk temperature of the continuous phase, q_p a volumetric particle heat source due to radiation, h_{lat} the latent heat of a possible phase change in the particle (i.e. boiling) and h_{react} is the heat of reaction, if such occurs. According to the right hand side of (2.73), the particle temperature is changed due to convective and conductive transport, i.e. due to existing temperature difference between particle T_p and its environment T_∞ . Energy transfer within a droplet due to viscous friction with the fluid is usually neglected.

2.2.3.4 Mass Transfer

The main amount of mass transfer between a particle and the environment occurs due to evaporation (if liquid particles are considered) or due to chemical reaction (in case of solid reacting particles). The latter are beyond the scope of this work and are not further discussed here. A general form of the mass transfer is given by the ordinary differential equation (2.74) for the mass rate evolution.

$$\frac{dm_p}{dt} = -M_{v,i} A_p \quad (2.74)$$

The evaporation rate is changed by the vapor mass flux $M_{v,i}$ through the particle surface A_p . The vapor mass flux is a function of the concentration difference of the vaporized species i at the particle surface $C_{i,p}$ and its concentration in the environment $C_{i,\infty}$. The concentration of vapor at the droplet surface is evaluated assuming that the partial pressure of vapor at the interface is equal to the saturated vapor pressure p_{sat} , at the particle droplet temperature, T_p :

$$C_{i,s} = \frac{p_{sat}(T_p)}{RT_p} \quad (2.75)$$

where R is the universal gas constant. The concentration vapor in the bulk gas is known from solution of the transport equation for species i :

$$C_{i,\infty} = X_i \frac{p}{RT_\infty} \quad (2.76)$$

where X_i is the local bulk mole fraction of species i , p is the local absolute pressure, and T_∞ is the local bulk temperature in the gas. The mass transfer coefficient k_{mass} is calculated from the

SHERWOOD number correlation

$$Sh_{AB} = \frac{k_{mass}d_p}{D_{i,m}} = 2.0 + 0.6Re_d^{1/2}Sc^{1/3} \quad (2.77)$$

where $D_{i,m}$ is the diffusion coefficient for the vapor in the bulk and d_p is the droplet diameter. The SHERWOOD number, as given in Equation (2.77), can be also approximated by the droplet REYNOLDS and the SCHMIDT number, as common for engineering applications ([77, 78]), where the SCHMIDT number gives the proportion of viscous to mass diffusion, $Sc = \nu/D$. The molar flux of the vapor \dot{X}_i can now be expressed as:

$$\dot{X}_i = k_{mass} (C_{i,s} - C_{i,\infty}) . \quad (2.78)$$

2.2.3.5 Effect of Turbulence on the Dispersed Phase Motion

The particle motion in a turbulent flow field has been investigated since the early 60^{ies}. There are numerous experimental investigations on this topic (Torobin and Gauvin [103], Clamen and Gauvin [15], Zarin and Nicholls [117], Rudoff and Bachalo [83]). According to them, turbulence can significantly affect the particle motion. Nevertheless, often due to the significant discrepancy between the quantitative experimental data, up to date in many cases the turbulence effect is neglected when performing numerical integration of the equation of particle motion. To quantify the influence of the turbulence many authors postulate and pursue the correlation between a characteristic turbulent quantity and the drag coefficient, assuming that the drag force is the most relevant force for the particle motion. The relative turbulence intensity, as defined in Equation (2.79), is such a turbulent quantity.

$$I_{rel} = \frac{\sqrt{u_f'^2}}{|\mathbf{u}_f - \mathbf{u}_p|} \quad (2.79)$$

The numerator in Equation (2.79) represents the velocity fluctuation of the carrier fluid. The denominator is the relative velocity between the particle and the carrier phase. The general tendency from the experiments is as follows:

- Increase of the relative turbulence intensity causes an increase of the drag coefficient (Uhlherr et al. [105] and Zarin et al. [117]).
- The higher the relative turbulence intensity, the lower the critical particle REYNOLDS number (Torobin and Gauvin [103] and Clamen and Gauvin [15]) which indicates the transition from a laminar to a turbulent boundary layer around the particle.

The integral turbulent length scale L_f is another suitable turbulent quantity for this purpose. Crowe et al.[16] provide a brief revue of the relevant experimental works. The results outline only a general tendency again. At a certain relative turbulence intensity an increase of the drag coefficient seems to correlate with an increasing ratio of the length scales L_f/d_p .

Nevertheless, due to the broad scale spectrum in turbulent flows, the phase interaction at different length or time scales addresses different physical phenomena. Such are the flow of particles much smaller than the KOLMOGOROV length scale, η , or the evolution of the particle boundary layer for particles bigger than η . The interaction mechanisms are still not fully understood

and for this reason the numerical simulation of such flows is increasingly applied for the last two decades. The rapid acceleration of computing resources in the 90^{ies} additionally supported the application of expensive techniques, such as Direct Numerical or Large Eddy Simulation, to resolve the stochastic structures, typical for a turbulent flow. Thanks to that, in the context of two-phase flow, it was possible to visualize unsteady interaction mechanisms between the discrete phase and turbulent structures.

Squires and Eaton [100], Armenio et al. [5], Fede and Simonin [28] apply DNS of a periodic box of homogeneous isotropic turbulence together with a Lagrangian particle tracking technique to gain insight into the mechanisms controlling the *particle dispersion in a turbulent flow field*. According to their investigations, the turbulent dispersion is mainly driven by the interaction of the particles with energy-containing eddies.

Deutsch and Simonin [20] quantify the particle dispersion in homogeneous turbulence with the particle kinetic energy and the particle LAGRANGIAN integral time scale, Equation (2.80).

$$D_p = \frac{2}{3} E_{kin,p} \tau_{pL} \quad (2.80)$$

The particle LAGRANGIAN integral time scale is defined as

$$\tau_{pL} = \int_0^\infty R_p \tau d\tau, \quad (2.81)$$

where $R_p(\tau)$ is the particle LAGRANGIAN velocity correlation function:

$$R_p(\tau) = \frac{\langle u'_{p,i}(\tau_0, \mathbf{x}) u'_{p,i}(\tau_0 + \tau, \mathbf{x} + \mathbf{u}_p \tau) \rangle_p}{2E_{kin,p}} \quad (2.82)$$

Nevertheless, with increasing STOKES number turbulent particle dispersion decreases.

An additional phenomenon observed in dilute two-phase flows is the *preferential accumulation*, which mainly denotes a deviation from the random distribution of particles in the flow. Preferential accumulation can be detected in form of settling of particles in regions with low vorticity or increased particle concentration in near wall regions. In contrast to the turbulent dispersion of particles, where in general the energy-containing eddies are responsible for the distribution, the accumulation does not seem to correlate with a specific flow scale.

- In homogeneous turbulence field Fessler et al. [31] detected the highest order of non-randomness for particles with τ_p similar to the KOLMOGOROV time scale. Fede [28] again confirmed this findings using Direct Numerical Simulation of homogeneous turbulence field and colliding heavy particles.
- Marchioli and Soldati [53] report of near-wall particle accumulation due to interaction with the streaky structures in the near-wall region. In addition the non-homogeneous velocity fluctuations, typical for near-wall turbulence, force the particle accumulation toward the wall.
- Squires and Eaton [100] identified regions with high strain rate, typical for the regions between macroscopic turbulence structures, where particles retain longer. Longmire and

Eaton [52] was also able to visualize particle preferential accumulation in a field of a periodically enforced round jet, where particles concentrate in the periphery of the macrostructures, generated by the forcing of the flow field.

Considering the bunch of numerical and experimental investigations of the last decades dedicated on the phenomenon *turbulence driven particle accumulation* no unique classification could be found. One main reason for this is that the phenomenon is still not fully understood. An additional barrier for such a classification is the missing unique definition of particle features by the different authors. The choice of the relevant flow time scale included in the STOKES number definition for example depends on the authors preferences. This makes the comparison between results of the variety of works very difficult.

2.2.4 Modeling Approaches for Dilute Dispersed Flows

2.2.4.1 Major Concepts

The major difference between the diverse modeling approaches is upon the representation of the secondary phase. One way to describe the discrete phase is to apply equations 2.4 to 2.14 which assumes continuum properties for the phase. Since the transport of the matter is considered in a global coordinate system, the method is well known as EULERIAN. The common practice of using this method is to represent the *global* behavior of the dispersed phase within the domain of interest. In other words, the properties of the dispersed phase result from an ensemble averaging over a large number of particles in a certain volume and not from the primary material properties of the matter within a single particle (droplet). This extended view on a continuum matter requires a new definition of material properties such as viscosity and density as well as the approximation of the shear stress term in the momentum equation, 2.5. The specification of material properties becomes more complex if the dispersed phase is represented by solid particles. The unclosed shear stress term in the momentum equation requires new constitutive expressions for the material behavior. Numerous relations are derived from the *Kinetic Theory for Granular Materials* as given by Ding and Gidaspow [23] and Boyle and Massoudi [11] and which is build upon very sophisticated theoretical basis. Nevertheless certain assumptions are inevitable in order to close further unknown terms. The latter makes the validation of such closures as shown by Dimitrova and Sadiki [21] very difficult. In addition the usability of the EULERIAN method is limited for dilute dispersed flows. The limitation arises from the underlying theory for the derivation of pseudo material properties. It assumes that sufficient number of discrete particles cross the domain of interest.

An alternative method for representation of the dispersed phase is the so called LAGRANGIAN method. It handles in a natural way dispersed flows, since the equations 2.53 to 2.55, 2.73 and 2.74, presented in the previous sections, can be applied straight forward. All particles are represented by equivalent mass-points. The information concerning particle dimensions and surface properties, such as surface tension, must be explicitly considered. This additional effort is usually covered by empirical correlations. Using this method the particle motion as well as mass and energy exchange with the carrier phase are resolved in time for each particle or droplet. Every particle path is computed separately and therefore an additional information about the state of other particles is not of essential necessity. This makes the method non-conservative. Effects such as particle-particle collisions or the prevention of unphysical particle accumulation

requires an explicit modelling (Yamamoto et al. [115], Dimitrova and Sadiki [22]).

Nevertheless the LAGRANGIAN method allows for fast computation of a large number of particles with different diameters. In the context of dilute dispersed two-phase flow this method in combination with turbulence resolving methods for the carrier phase such as DNS and LES, as described in Section 2.1.3, represents a powerful tool for detailed investigation of multiphase flow phenomena and especially of phase interaction as Marchioli and Soldati [53] showed for particle segregation in a turbulent boundary layer.

Despite the enormous potential of the LAGRANGIAN method, the combination with LES opens diverse questions about the reliability of the simulations. The works of Kuerten and Vreman [45] and Kuerten [46] show that the coupling between carrier and dispersed phase simply through the filtered properties of the carrier phase omits a certain amount of the real inter-phase momentum transfer and eventually leads to inaccurate flow prediction. In addition series of numerical investigations, see Vance et al. [107], Vreman [109], Caraman et al. [13], reveal the importance of inter-particle collisions even for dilute dispersed flows when using LES to model the carrier phase.

The present work adopts the LAGRANGIAN method to model the dispersed phase in combination with large-eddy simulation for the simulation of dilute dispersed two-phase flows. The equations for the dispersed phase are used in the form as defined in Section 2.2.3.1. The momentum applied on a single particle results commonly from drag, gravitational and pressure gradient force. Hence Equation (2.54) takes the form:

$$m_p \frac{d\mathbf{u}_p}{dt} = \frac{1}{2} \rho_f C_D A_p (\mathbf{u}_f - \mathbf{u}_p) + m_p \mathbf{g} - \nabla p V_p \quad (2.83)$$

The fluid velocity in Equation (2.83) denotes the filtered fluid velocity from the LES. In order to investigate the effect of the unresolved turbulent scales on the particle motion a simple dispersion model is applied. The model is described in the following Section 2.2.4.3. For the test cases, which include sub-grid scale turbulent particle dispersion the fluid velocity \mathbf{u}_f denotes the sum of the filtered fluid velocity and a fluctuating component.

Inter-particle collisions and particle rotation are not explicitly considered in the simulations.

The energy transfer from the dispersed phase is computed using Equation (2.73) without consideration of reaction heat and radiation terms. The change of the particle temperature over a specified time Δt reads as follows:

$$T_p(t + \Delta t) = T_\infty + [T_p(t) - T_\infty] e^{-(A_p h \Delta t)/(m_p c_p)} \quad (2.84)$$

The mass transfer, as defined in Equation (2.74), is now integrated again over a time Δt as follows:

$$m_p(t + \Delta t) = m_p(t) - \dot{X}_i A_p M_{w,i} \Delta t \quad (2.85)$$

where $M_{w,i}$ is the molecular weight of the species i ([2]). Within the particle (droplet) a homogeneous distribution of the temperature and species field is assumed. For the modeled configurations the temperature difference between carrier and dispersed phase is very narrow. Therefore it is expected that the error of mass and energy transfer due to the simplified models remains very limited.

2.2.4.2 Two-Way Coupling

The consideration of influence of the dispersed phase on the carrier fluid is referred as to *two-way coupling*. According to the classification proposed in Crowe et al. [16] *two-way coupling* models are required in flows with particle volume fraction $\alpha_p > 5 \cdot 10^{-7}$, i.e. even in very dilute two-phase flow the dispersed phase can affect the behaviour of the carrier fluid. In the mathematical model this influence is expressed due to source terms in the transport equations for the continuum phase.

The momentum balance for the continuum phase includes the effect due to drag. The source term S_m in the momentum equation 2.5 reads as:

$$S_m = -\frac{1}{2}\rho_f C_D A_p (\mathbf{u}_f - \mathbf{u}_p) \quad (2.86)$$

In case of droplet evaporation or particles with volatile components the amount of mass that the particle loses appears as a source term on the right hand side of the continuity and species transport equations for the continuum phase. I.e. according to the notation in Equation (2.14) the source term S_{Y_α} for the species α is:

$$S_{Y_\alpha} = -\dot{X}_\alpha A_p M_{w,\alpha} = -\frac{\dot{m}_{p,0}}{m_{p,0}} \Delta m_p \quad (2.87)$$

In other words, Finally the source term in the energy equation 2.12 for non-reacting flows denotes the energy consumed for the evaporation of Δm_p and the energy diffusion due to temperature gradients between the surrounding fluid and the particle. The index 0 denotes the initial particle state of the time period for which the source term is considered.

$$S_h = -\frac{\dot{m}_{p,0}}{m_{p,0}} \Delta m_p h_{lat} - k_{th} A_p (T_\infty - T_p) \quad (2.88)$$

2.2.4.3 Turbulent Dispersion

The model adopted in the present work has its origin in the concepts described Section 2.2.3.5. It is based on the eddy crossing / eddy life time concept. The fundamental idea is that during the computation of the drag force, a random component is added to the fluid velocity seen by the particle.

$$u_{fl} = \tilde{u} + u' \quad (2.89)$$

Using this modified velocity the particle equation of motion is integrated. In the so called *Discrete Random Walk* model, this fluctuating components are assumed to be piecewise constant in time. The value is kept constant over an interval of time given by the characteristic lifetime of an eddy, modeled by a turbulence model. The prediction of the particle dispersion makes use of the concept of the integral time scale t_L , which describes the time spent in turbulent motion along the particle path, ds :

$$t_L = \int_0^\infty \frac{u'_p(t)u'_p(t+s)}{\overline{u_p'^2}} ds \quad (2.90)$$

The integral time is proportional to the particle dispersion rate. It can be shown that the particle diffusivity is given by $\overline{u'_i u'_j} t_L$. For small "tracer" particles that move with the fluid (zero drift

velocity), the integral time becomes the fluid LAGRANGIAN integral time, t_{0L} . This time scale can be approximated as $t_{0L} = C_L \frac{l}{\varepsilon}$. The model constant C_L is not known a priori and needs to be determined. Usually this is done by assuming that for very small particles that should be the diffusivity predicted by an eddy viscosity turbulence model ν_t/σ . One can obtain

$$t_L \approx 0.15 \frac{k}{\varepsilon} \quad (2.91)$$

Depending on the turbulence model the time scale rule can be adjusted accordingly.

In the context of the Discrete Random Walk model, the influence of a modelled eddy on the particle is estimated. Each eddy is characterized by the GAUSSIAN distributed random velocity fluctuations u' , v' , w' and a timescale τ_e . The values of the fluctuations, that prevail during the lifetime of the turbulent eddy are sampled assuming that they obey a GAUSSIAN probability distribution, so that

$$u' = \zeta (\bar{u'^2})^{1/2} \quad (2.92)$$

where ζ is a normally distributed random number, and the right-hand side of the equation is the local RMS value of the velocity fluctuations. Since the kinetic energy is modelled or can be computed from the turbulence model (e.g. the sub-grid stress model) it can be computed as:

$$(\bar{u'^2})^{1/2} = (\bar{v'^2})^{1/2} = (\bar{w'^2})^{1/2} = \left(2 \frac{k}{\varepsilon}\right)^{1/2} \quad (2.93)$$

Here local isotropy of the components is assumed. This is not necessary when a full stress RANS model is used, but convenient in the context of LES. The characteristic eddy lifetime is defined either as a constant $\tau_e = 2t_L$ or as a random variation about t_L by adopting $\tau_e = -t_L \ln(\xi)$, where ξ is a uniform random number between 0 and 1. The option of using random τ_e usually yields a more realistic description of the dispersion.

The particle eddy crossing time is defined as:

$$t_{cross} = -\tau_p \ln \left(1 - \frac{l_e}{\tau |u - u_p|}\right) \quad (2.94)$$

where l_e is the eddy length scale. The particle is assumed to interact with the fluid phase eddy over the smaller of the two time values: the eddy lifetime or the eddy crossing time. When this time is reached, a new value of the instantaneous velocity is obtained, by applying a new value for ζ .

3 Numerical Methods

This chapter describes the numerical representation of the mathematical-physical governing equations, presented in Section 2, and their solution. The basic strategies are presented for solution of multiphase problems with emphasis on the methods used in the present work.

3.1 Numerical Methods for Continuous Flows

There are several numerical techniques established for the numerical solution of continuum problems. *Finite Difference Method* (FDM), *Finite Volume Method* (FVM) and *Finite Element Method* (FEM) are the three most famous techniques within this scope. All three are based on the discretization of the physical problem (domain) into a finite number of units. The governing equations are redefined and solved for these units. However, they are differently assessed applied to fluid simulations. The FDM represents an efficient method, which is furthermore relative simple to program. In general its application is limited due to the necessity of using structured orthogonal numerical meshes. The conservation of the flow quantities in the sense, as discussed in the previous chapter, is not guaranteed. The FEM is not restricted to regular orthogonal meshes and can be applied for discretization of very complex geometries. The basic idea is to compute the displacement of each numerical point due to balancing the acting forces. For this high order polynomials are applied, the so called form-functions. The method is not conservative and the discretized form of the governing equations leads to a broad band matrices, which need a preconditioning step. Although the method offers a high order discretization, it plays only a minor role for flow problems. The commonly applied method for various flow problems is the FVM. The method is adopted by scientific and commercial codes. The present simulations are preformed in the framework of FVM and the method with its main issues and abilities are presented in the following section. The formulation is based on the computation of integral quantities over an arbitrary volume, allows for non-monotonic evolution of the solution variables and maintains the conservation flow properties.

3.1.1 Discretization of the Governing Equations

The FVM is based on the integral form of the conservation equations. For an arbitrary scalar ψ , the conservation equation can be written in integral form for an arbitrary volume V as shown in Equation (3.1).

$$\underbrace{\int_V \frac{\partial(\rho\psi)}{\partial t} dV}_{\text{accumulation}} + \underbrace{\int_V \frac{\partial}{\partial x_i}(\rho u_i \psi) dV}_{\text{convection}} = \underbrace{\int_V \frac{\partial}{\partial x_i} \left(\Gamma_\psi \frac{\partial \psi}{\partial x_i} \right) dV}_{\text{diffusion}} + \underbrace{\int_V S_\psi dV}_{\text{source}} \quad (3.1)$$

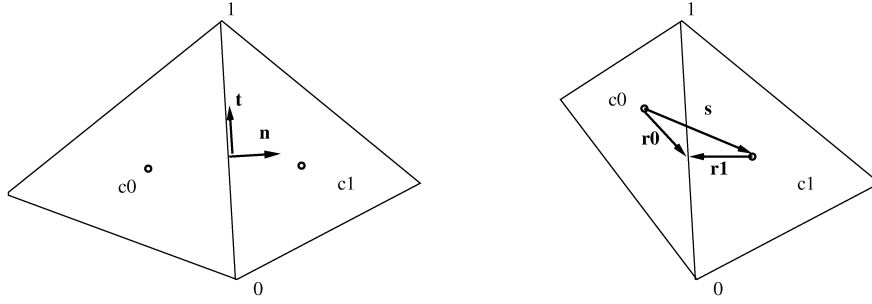


Figure 3.1: Notation for an arbitrary cell.

The GAUSS (divergence) theorem, Equation (3.2), is applied on Equation (3.1).

$$\int_V \frac{\partial \psi}{\partial x_i} dV = \int_A \psi n_i dA \quad (3.2)$$

In the convective and the diffusion term A represents the cell boundary. In the context of the numerical method the control volume is an arbitrary polyhedron and its boundary surface is achieved by the summation over all cell (*faces*). According to this, the surface integral can be split in a sum of integrals of the faces, f . It is assumed that ψ is uniformly distributed over the face and ψ_f is the value of the variable at the face f , estimated for the face centroid. The new form of the conservation equation reads:

$$\frac{\partial(\rho\psi)}{\partial t} \Delta V + \sum_f \rho_f u_{i,f} \psi n_i dA_f = \sum_f \Gamma_\psi \frac{\partial \psi}{\partial x_i} n_i dA_f + S_\psi \Delta V \quad (3.3)$$

The value of the unsteady term and the source term is assumed to be constant over the cell and the volume integrals can be rewritten as shown in Equation (3.3). The time derivative discretization will be discussed in Paragraph Temporal Discretization. n_i is the normal vector of A_f in Cartesian coordinates. For the further procedure is postulated that all flow variables are stored in the cell center. This storage structure is referred to as *collocated*. The cells, if not explicitly defined to be part of a structured mesh, are numerated 0, 1, 2, ... Since all variables are stored in the cell center, the value of the variable at the cell face needs to be approximated. For the notation the symbols are used, as denoted in Figure 3.1. The directed distance between two cell centers is denoted by s , the face normal and tangential vectors are denoted by \mathbf{n} and \mathbf{t} , respectively. In addition, the vectors from the cell centroid to the face centroid are \mathbf{r}_0 and \mathbf{r}_1 for the cell 0 and 1, respectively. For the further estimation of the convective and diffusive fluxes, assuming that the mass flux $\rho_f u_{i,f}$ are known, the values of ψ and $\frac{\partial \psi}{\partial x_i}$ at the face centroid needs to be estimated.

Spatial Discretization

Several discretization schemes are described in the following, referring to their relevance for the present work. The simplest assumption for the face centroid value of ψ_f is the usage of an *upwind* scheme, i.e. the face value adopts the cell center value of the "upwind" cell ($\psi_f = \psi_0$, assuming the *upwind* cell is c_0). The latter is defined from the velocity vector, normal to the

face.

For better approximation of the variable face value, it is recommended to apply a higher order schem, using Taylor series expansion for ψ_0 . For *second order upwind* scheme this expansion has the form as shown in Equation (3.4).

$$\psi_f = \psi + \nabla\psi \mathbf{r} \quad (3.4)$$

The ψ and $\nabla\psi$ are the cell value and the cell gradient in the *upwind* cell, \mathbf{r} is the vector between the cell and face centroids. For this scheme is required the estimation of the cell gradient, which is presented in the next Paragraph "Gradient Estimation". It is possible to obtain higher orders upwind-type schemes if more terms of the Taylor series are retained. Truncating the series after the third term and considering the second derivative leads to the so called QUICK scheme. Further informations concerning upwind schemes can be found in Barth and Jespersen [8]. Another formulation of a second order discretization scheme gives the *Central Differencing Scheme*, (CDS). For this the face value of ψ_f can be interpolated from both neighboring cells. If the notation from Figure 3.1 is used, the expression for ψ_f reads as (3.5).

$$\psi_f = \frac{\psi_0 + \psi_1}{2} + \frac{\nabla\psi_0\mathbf{r}_0 + \nabla\psi_1\mathbf{r}_1}{2} \quad (3.5)$$

On non-orthogonal meshes the consideration of the neighboring cell gradients leads to an improved approximation of the face value compared to the simple distance weighting of the cell values. Its potential to generate oscillations is a limitation of this scheme. Such oscillations which lead to unphysical flow solutions. In the context of LES, the scheme is often applied because of its low magnitude of numerical diffusion. Since the turbulence model supply a very low turbulent viscosity, the solution can become unstable. Therefore, the alternative *bounded CDS*, based on the normalized variable diagram approach [50], will prevent instabilities due to discretization. The general idea is a combination of pure CDS and a blending between CDS and second order upwind scheme based on the convection boundedness criterion.

Gradient Estimation

The gradient $\nabla\psi$ at the cell centroid can be estimated by using the again the divergence theorem for the cell volume c_0 .

$$(\nabla\psi)_0 = \frac{1}{\Delta V} \sum_f \overline{\psi_f} \mathbf{n} A \quad (3.6)$$

The summation is over all faces of the cell. The estimation of the face value, $\overline{\psi_f}$, can be accomplished in several ways. Simple and fast solution is provided by using an arithmetic average of the neighbor cell center values, (3.7), also referred to as *cell based* gradient evaluation.

$$\overline{\psi_f} = \frac{\psi_0 + \psi_1}{2} \quad (3.7)$$

The so called *node based* evaluation offers an alternative method to estimate $\overline{\psi_f}$ as the arithmetic average of N_f node values $\overline{\psi_n}$, (3.8). N_f is the number of the face nodes. The node value $\overline{\psi_n}$ is computed from the weighted average of the surrounding cells values. The node values are

obtained in ANSYS FLUENT by the solving of a constrained minimization problem, which is second order accurate on arbitrary unstructured meshes ([40]).

$$\overline{\psi_f} = \frac{1}{N_f} \sum_n \overline{\psi_n} \quad (3.8)$$

This method provides a more accurate estimation of the cell gradient but is expensive in terms of time.

Diffusive Flux

To integrate the diffusion term, it is necessary to compute the diffusion flux D_f at each face of the control volume.

$$D_f = \Gamma_f \nabla \psi \cdot \mathbf{A} \quad (3.9)$$

Γ_f is here the diffusion coefficient interpolated to the face. The basic idea adopted for non-orthogonal meshes is to split the diffusion flux in to a part which is normal to the face area vector \mathbf{A} and a part which is tangential to the face. Since an implicit treatment based on cell gradients of ψ is not possible because of the dependence of $\nabla \psi$ on all neighbor cells, it is tried to adopt an implicit treatment for the face normal part of the flux. The tangential component is added explicitly. The explicit part is written as difference between the total cell derivative and the normal component.

$$D_f = \Gamma_f \frac{\psi_1 - \psi_0}{ds} \frac{\mathbf{A} \cdot \mathbf{A}}{\mathbf{A} \cdot \mathbf{s}} + \Gamma_f \left(\nabla \psi_f \cdot \mathbf{A} - \nabla \psi_f \cdot \mathbf{s} \frac{\mathbf{A} \cdot \mathbf{A}}{\mathbf{A} \cdot \mathbf{s}} \right) \quad (3.10)$$

The value of the gradient at the face $\nabla \psi_f$ needs to be interpolated to the face based on the neighbor cell gradients. Further details if the overall procedure can be found in Mathur and Murthy [59].

Temporal Discretization

The time derivative can be approximated using, for example, first or second order time discretization as shown in Equation (3.11) and (3.12), respectively.

$$\frac{\partial \psi}{\partial t} \approx \frac{(\rho\psi)^{n+1} - (\rho\psi)^n}{\Delta t} = \frac{1}{\Delta V} \left(\sum_f C_f + \sum_f D_f + S_\psi \Delta V \right) \quad (3.11)$$

$$\frac{\partial \psi}{\partial t} \approx \frac{3(\rho\psi)^{n+1} - 4(\rho\psi)^n - (\rho\psi)^{n-1}}{\Delta t} = \frac{1}{\Delta V} \left(\sum_f C_f + \sum_f D_f + S_\psi \Delta V \right) \quad (3.12)$$

The terms on the right hand side of the upper equations denote the spatial discretized convective, C_f , and diffusive, D_f , fluxes together with the volumetric source term S_ψ . An implicit time integration is achieved if the terms of the right hand side involve the value from the current time step ψ^{n+1} . In the explicit formulation the values available from the previous time step ψ^n are used for the estimation of the convective-diffusive fluxes. The implicit time integration allows in general larger time steps. The storage required for this type of time integration is higher

since the values of ψ for at least two time steps are need to be stored for the computation of the variable in the current time level.

Linearized System of Equations

Since all face values and the face gradients in the discretized equation of ψ_0 are expressed in terms of the cell values of ψ , the terms can be reorganized in the form as given in Equation (3.13).

$$a_0\psi_0 = \sum_{nb} a_{nb}\psi_{nb} + b \quad (3.13)$$

The indexes 0 and nb denote the cell c_0 and its neighbors. The total number of neighboring cells depends on the mesh topology. a_0 and a_{nb} are the corresponding coefficients and b is the source term. The set of linearized equations of all controll volumes leads to the system of equations, Equation (3.14), which is solved using a linear equation solver. The matrix A contains all coefficients, ψ is the solution variable vector, containing all cell values of the solution variable ψ . \mathbf{b} is the source term vector.

$$A\psi = \mathbf{b} \quad (3.14)$$

3.1.2 Pressure-Velocity Coupling

The momentum (2.5) equation is discretized by using the same interpolation methods as discussed above. ψ is replaced by a velocity component in the equation of the generic scalar (3.1). From the discretized momentum equation several issues arise: the velocity is needed to compute the mass fluxes ($\rho_f u_{i,f}$), as well; the pressure gradient is unknown and finally the continuity and the momentum equations are coupled. A special treatment is required for this system of equations. In the following two concepts to resolve this issues are presented.

Evaluation of the Pressure Gradient

In order to complete the discretization of the momentum equation, the pressure gradient needs to be approximated first. If the GAUSS theorem is applied again, following, the pressure gradient is transformed to:

$$\int_V \nabla p \, dV = \int_A p \, n_i \, dA \approx \sum_f p_f n_i A_f \quad (3.15)$$

Here, again, the assumption is made that the face centroid value p_f is the mean face value. Since the pressure is stored at the cell center as the other solution variables, its face value needs to be interpolated. Possible interpolation schemes are: the linear interpolation between the cell centroids of the face adjacent cells; second order schemes similar to these applied for the convective terms. Alternative, the p_f can be interpolated using a weighted average of the neighbor cell center pressure values. As weighting factors the coefficient a_0 and a_1 from the discretized momentum equations of the neighbor cells c_0 and c_1 are used (Rhie and Chow [79]). However, the interpolation method works well only for smooth pressure fields and small body forces. The stability and reliability of the simulation can be further improved if a "staggered" representation for the pressure is used. The method is presented by Patankar [68] for structured

staggered grids. The method can be modified for an unstructured grid.

Discretization of the Continuity and Momentum Equations

The momentum equation in discretized form reads (3.16):

$$a_0 u_i = \sum_{nb} a_{nb} u_{nb} - \sum_f p_f n_i A_f + b \quad (3.16)$$

For the continuity equation the same transformations, as outlined above, are performed. The mass conservation equation, written in integral form according to FVM, yields the form after applying the divergence theorem:

$$\sum_f J_f A_f = 0 \quad (3.17)$$

where $J_f = \rho_f u_f$. The face velocities, in general, are not estimated by standard interpolating scheme used for the convection terms, since it will lead to checker-boarding of the velocity and pressure fields. Instead, the interpolation method, proposed by Rhie and Chow [79], is applied. According to this, the mass flux at the face f is computed as the average of the cell center velocities from the adjacent cells, weighted by the central coefficients of the momentum equation, (3.18).

$$J_f = \rho_f \frac{a_0 u_{0,n} + a_1 u_{1,n}}{a_0 + a_1} + d_f ((p_0 + (\nabla p_0) r_0) - (p_1 + (\nabla p_1) r_1)) \quad (3.18)$$

u_n is the face normal velocity, d_f is a function of the cell coefficients from the momentum equation. The density ρ_f at the face can be estimated from an arithmetic average of the neighboring cell center values.

SIMPLE Algorithm

The SIMPLE algorithm goes through several steps of subsequent pressure and velocity corrections until the requirement for convergence of both equations is fulfilled. The general steps of the algorithm are as follows:

- The momentum equation is solved using a guess pressure p^*
- The new flux J_f^* is computed, according to Eq. (3.18): $J_f^* = \hat{J}_f^* + d_f(p_0^* - p_1^*)$
- J_f^* is corrected by J'_f in a way to satisfy the requirements for mass conservation:

$$J_f = J_f^* + J'_f \quad (3.19)$$

- the correction flux is defined as $J'_f = d_f(p'_0 - p'_1)$
- The pressure correction equation is obtained from the continuity equation after substituting (3.19) in the continuity equation (3.18). p' denotes the cell value of the corrected pressure.

$$a_p p' = \sum_f a_f p'_f + \sum_f J_f^* A_f \quad (3.20)$$

- The iterative solver estimates the value of cell correction pressure p' and updates the actual pressure after the initial guess. In general the pressure correction needs an under-relaxation: $p = p^* + \alpha p'$
- In the final step the fluxes J_f from Equation (3.19) are computed.

Fractional Step Algorithm for Unsteady Simulations

In the Fractional Step method an approximate factorization is used to decouple the continuity and momentum equations [6], [43]. If a second order implicit scheme is applied for the temporal discretization (Equation (3.21)) the momentum equation for the new time step ($n + 1$) reads:

$$\frac{\partial}{\partial t}(\rho \mathbf{u}) = \frac{\rho}{2\Delta t}(3\mathbf{u}^{n+1} - 4\mathbf{u}^n + \mathbf{u}^{n-1}) \quad (3.21)$$

$$\left[\frac{3\rho V}{2\Delta t} \mathbf{I} + \mathbf{A}^* \right] \mathbf{u}^{n+1} + \mathbf{G}p^{n+1} = \frac{\rho V}{2\Delta t}(4\mathbf{u}^n - \mathbf{u}^{n-1}) + \mathbf{S}_u \quad (3.22)$$

\mathbf{I} is the identity operator, \mathbf{A}^* contains the spatial operators for the convective and diffusive terms, \mathbf{G} is the gradient operator and \mathbf{S}_u is the momentum source. Equation (3.22) can be rewritten in the form:

$$\mathbf{A}\mathbf{u}^{n+1} + \mathbf{G}p^{n+1} = \mathbf{r} \quad (3.23)$$

$$\mathbf{D}\mathbf{u}^{n+1} = 0 \quad (3.24)$$

where \mathbf{A} describes the term in the brackets on the left hand side, and \mathbf{r} denotes the term on the right hand side of Equation (3.22). Equation (3.24) is the continuity equation for incompressible flows with constant material properties. \mathbf{D} is the divergence operator. If the pressure change between two time levels is $\delta p^{n+1} = p^{n+1} - p^n$ the latter, applied on Equation (3.23) and (3.24), leads to the following result, written in block matrix form:

$$\begin{pmatrix} \mathbf{A} & \mathbf{G} \\ \mathbf{D} & 0 \end{pmatrix} \begin{pmatrix} \mathbf{u}^{n+1} \\ \delta p^{n+1} \end{pmatrix} = \begin{pmatrix} \mathbf{r}^n - \mathbf{G}p^n \\ 0 \end{pmatrix} \quad (3.25)$$

The matrix equation is approximated by as written in Equation (3.26), where $\Delta t^* = 2\Delta t/(3\rho V)$.

$$\begin{pmatrix} \mathbf{A} & (\Delta t^* \mathbf{A})\mathbf{G} \\ \mathbf{D} & 0 \end{pmatrix} \equiv \begin{pmatrix} \mathbf{A} & 0 \\ \mathbf{D} & -\Delta t^* \mathbf{D}\mathbf{G} \end{pmatrix} \begin{pmatrix} \mathbf{I} & \Delta t^* \mathbf{G} \\ 0 & \mathbf{I} \end{pmatrix} \quad (3.26)$$

The error, introduced by this approximation, is second order and is of the same order as the truncation error of the temporal discretization, applied above. The right hand side of Equation (3.26) is the factored matrix, and the solution steps can be expressed as follows, Equation (3.27):

$$\mathbf{A}\tilde{\mathbf{u}} = -\mathbf{G}p^n + \mathbf{r}^n \quad (3.27)$$

$$\Delta t^* \mathbf{D}\mathbf{G}\delta p^{n+1} = \mathbf{D}\tilde{\mathbf{u}} \quad (3.28)$$

$$\mathbf{u}^{n+1} = \tilde{\mathbf{u}} - \Delta t^* \mathbf{G}p^{n+1} \quad (3.29)$$

- solve the intermediate velocity field $\tilde{\mathbf{u}}$ (3.27)
- solve the pressure correction equation (3.28)
- update the pressure field from $p^{n+1} = p^n + \delta p^{n+1}$
- correct the velocity with the new from the new pressure field (3.29)

Since the method does not need *outer* iterations per time step, it is very efficient in time. It represents a good alternative to the methods using explicit time discretization, moreover, with this method the time step is limited only by the flow problem and its desired temporal resolution and not by the CFL criterion.

3.1.3 Boundary conditions

Before proceeding to the solution of the linearized system of equations, it is necessary to specify the boundary conditions for the considered domain. Depending on the physical geometry, the used models for description of the fluid motion and probably additional conditions, such as heat conduction on walls, or state of the flow due to compressibility effects leads to a large variation of boundary conditions. Within the present context, however, their number can be reduced to four.

Periodic Condition

The periodic type of boundary condition denotes that the flow velocity repeats in space as:

$$\mathbf{u}(\mathbf{r}) = \mathbf{u}(\mathbf{r} + n\mathbf{L}) \quad (3.30)$$

where $n = 0, 1, \dots$ and \mathbf{L} is the periodic distance. For the pressure holds that the pressure drop $\Delta p(\mathbf{r})$ is constant in the periodic direction.

Inflow Boundary

In the context of LES the inflow boundary condition can be defined by a mass flow or a velocity profile in conjunction with turbulent quantities. The mass flow condition does not accounts for an alternating profile at the inlet. This is an issue in LES context, since the computational domain in general does not include the longer supplying sections. The length for the development of a certain state of the turbulent flow is much longer, compared to the modeled domains. This essential flow properties need to be recovered for the simulation.

This represents a DIRICHLET boundary condition. The mean velocity field is defined, in addition turbulent characteristics, such as turbulent intensity, fluctuating velocity etc., can improve the quality of the generated turbulence. The main issue is on the generation of turbulent fluctuations, since the reconstruction of an real turbulent field, without a priori knowledge of the turbulent properties, is not trivial. Different options are presented below.

- The generation of so called *white* noise perturbation of the velocities is mostly insufficient, since they do not obey the energy spectrum as usually exhibited by turbulent flows. These perturbations are dissipated within a relative short distance after their initiation.

- **Generation of LAGRANGIAN vortices:** The method is based on the LAGRANGIAN form of the two-dimensional equation of the vorticity. The particles, used to discretized the vorticity equation, transport the artificial eddies. This eddies are convected randomly away from the inlet plane. The intensity of the vortex is related to a mean turbulent quantities, such as the turbulent kinetic energy. The extension in streamwise direction is defined by using the turbulent mixing length hypothesis

Outflow Boundary

A standard NEUMANN formulation is used for the fluid velocity at the exit boundary. All solution quantities except the static pressure are extrapolated on the boundary face from the boundary adjacent cell. Considering that all simulated configurations deals with subsonic flow regime, the outlet static pressure is known a priori.

Wall Boundary

At walls allpy a DIRICHLET condition for the fluid velocity. Concerning the energy equation an adiabatic wall is modelled such as $\nabla T \cdot \mathbf{An} = 0$ (NEUMANN condition). Otherwise, a heat flux shall be specified.

3.1.4 Solving the Linear System

The equations for an arbitrary scalar, discretized in the manner as shown from the beginning of this section, (3.1), build a set of algebraic equations with a sparse coefficient matrix. The linearized system can be solved using standard solvers, such as ILU or GAUSS-SEIDEL.

The combination of one of the solver with an Multigrid method accelerates the solution of the matrix and prevents instabilities at the beginning of the iterations, if the initial variable field deviates significant from the final solution.

Depending on the way, how the interpolation between the levels of the multigrid solver is performed, there are in general two types of such methods. The first is based on geometrical coarsening and refinement of the various grids. It is, however, restricted to structured mesh type definition. The second type of mutigrid methods accomplishes the prolongation (coarsening) and restriction (refining) operations based on an appropriate interpolation between the matrix coefficients. This method is often applied on unstructured grids and is known as *Algebraic Multigrid*. More information concerning the multigrid method, together with further references can be found in Ferziger and Peric [29].

3.2 Numerical Methods for Discrete Phase

For the simulation of dispersed flows two main groups of methods have gained popularity. The one is based on a continuity assumption and resembles the *Multi Fluid* approach, also known as *Eulerian multiphase*. Such methods treat the dispersed phase as a continuum. Possibly special models for the stress tensor are adopted. Examples for this are models based on kinetic theories, like the Granular theory approach. Such models describe the inter-particle collision based on kinetic assumptions in a very efficient manner. Their limitation arises from the fact, that the

equations can be closed only for a constant particle diameter, which renders the simulation of polydispersed systems problematic. In the recent past, progress was made to overcome this limitation. The developments in the area of population balance methods utilizing (D)QMOM are only mentioned here.

The second main group of methods is based on the LAGRANGIAN frame and hence on the tracking of individual particles. Most often the point particle assumption is adopted, i.e. mass points are tracked and the individual particle extents are ignored. This simplification delivers consistent results for most of the cases of interest here. Nevertheless, when special attention is paid to the particle distribution very close to the boundary and the actual particle size is comparable with a resolved boundary layer thickness, it can become problematic. The deficit of LAGRANGIAN based multiphase models, is that the consideration of inter-particle collisions is difficult and expensive. In the context of DNS and LES most typically hard-sphere collision models are applied for dilute flows. In the situation of very dense particulate flows, operated in the frictional regime, also soft-sphere DEM (Discrete Element Method) is increasingly used. The main difference between soft and hard sphere collision detection is that in the soft sphere method every collision is resolved utilizing a certain number of integration steps and a repulsive force is computed based on the mutual distance of each possible collisional pair of particles. In the hard sphere approach intersecting points of trajectories are detected. This renders the method more efficient for the computation of dilute two-phase flows.

The focus of this work is set on the LAGRANGIAN description of the dispersed phase. The methods for solving the governing equations in the LAGRANGIAN frame are outlined below.

3.2.1 Integration of the Particle Equations of Motion

The trajectory equations for the particles are solved by stepwise integration over discrete time steps. Integration of Equation (2.54) yields the velocity of the particle at each point along the trajectory as given by:

$$\frac{dx}{dt} = u_p \quad (3.31)$$

The equations (2.54) and Equation (3.31) are a set of coupled ordinary differential equations and can be casted into the following form:

$$\frac{du_p}{dt} = \frac{1}{\tau_p} (u - u_p) + a \quad (3.32)$$

where a includes all other forces, except drag force. This set can be solved for constant u , a and τ_p by analytical integration. For the particle velocity at the new location u_p^{n+1} the following holds:

$$u_p^{n+1} = u^n + e^{-\frac{\Delta t}{\tau_p}} - a\tau_p \left(e^{-\frac{\Delta t}{\tau_p}} - 1 \right) \quad (3.33)$$

The new location x_p^{n+1} can be computed from a similar relationship.

$$x_p^{n+1} = x^n + \Delta t (u^n + a\tau_p) + \tau_p \left(1 - e^{-\frac{\Delta t}{\tau_p}} \right) (u_p^n - u^n - a\tau_p) \quad (3.34)$$

In these equations u_p^n and u^n represent particle and fluid velocities at the old location. This formulation is known as the *analytic* integration scheme. Numerical integration schemes can

also be applied to the given set of equations. When applying the EULER implicit scheme, the equation for the new velocity reads:

$$u_p^{n+1} = \frac{u_p^n + \Delta t \left(a + \frac{u_p^n}{\tau_p} \right)}{1 + \frac{\Delta t}{\tau_p}} \quad (3.35)$$

The trapezoidal integration rule yields:

$$\frac{u_p^{n+1} - u_p^n}{\Delta t} = \frac{1}{\tau_p} (u^* - u_p^*) + a^n \quad (3.36)$$

$$u_p^* = 0.5 (u_p^n + u_p^{n+1}) \quad (3.37)$$

$$u^* = 0.5 (u^n + u^{n+1}) \quad (3.38)$$

$$u^{n+1} = u^n + \Delta t u_p^n \cdot \nabla u^n \quad (3.39)$$

The particle velocity at the new location is computed by

$$u_p^{n+1} = \frac{u_p^n \left(1 - 0.5 \frac{\Delta t}{\tau_p} \right) + \frac{\Delta t}{\tau_p} (u^n + 0.5 \Delta t u_p^n \cdot \nabla u^n) + \Delta t a}{1 + 0.5 \frac{\Delta t}{\tau_p}} \quad (3.40)$$

For the implicit and trapezoidal schemes, the new particle location is always computed by a trapezoidal rule.

$$x_p^{n+1} = x_p^n + 0.5 \Delta t (u_p^n + u_p^{n+1}) \quad (3.41)$$

Typically the *Automated Tracking Scheme Selection* is used to carry out simulations involving particle tracking throughout the present work. When this is used, the appropriate scheme will be selected based on an error estimation in order to ensure maximum stability and high accuracy when possible. The approach is considered to deal well with most of the changes in the forces acting on the particle ([2]).

For the computation of the drag force, the fluid velocity at the particle position needs to be estimated. Since in the context of the Finite Volume Method, this is available at the control volume centroids, a second order accurate extrapolation scheme is adopted here. If \mathbf{r} is the vector from the centroid to the particle position, and u_{cell} is the control volume velocity and ∇u_{cell} the velocity gradient vector computed for the control volume, the scheme reads as follows:

$$u_f = u_{cell} + \nabla u_{cell} \cdot \mathbf{r} \quad (3.42)$$

When two-way coupled simulations are applied, a source term accounting for the influence of the dispersed phase on the continuous phase needs to be considered. Here, the computation of the momentum source term is shown, without the loss of generality. For other equations (like for energy transfer), the computation is done in the same way. When a particle enters a new control volume, its state at entrance is saved. When the particle leaves the cell, the new, changed state is compared to the entry state. The difference, here for the momentum is set as a source term to the momentum equation of the continuous phase.

$$S_{mom} = m_{p,1} \mathbf{u}_{p,1} - m_{p,0} \mathbf{u}_{p,0} - \sum_{i=0}^{nsteps} \mathbf{b}_i \quad (3.43)$$

The last term in the equation is the integral over all substeps in the control volume of the body force vector for the particle equation of motion. This has to be subtracted from the source term, since body forces do not originate from the fluid (e.g. the gravity force is due to the mass of the Earth and the particle).

3.2.2 Boundary Conditions

Inlet Boundary

Using the LAGRANGIAN method implies that every parcel injected in the computational domain features its own set of initial position, velocity, temperature, diameter and material properties. This allows for a large flexibility when dealing with dispersed flows with broad or multimodal diameter distribution.

A special account is paid in this work on the generation of instantaneous inlet velocity conditions for the dispersed phase. If available from experiment different correlations and property data for the dispersed phase are taken into account. The particle velocity is randomized around the mean value, where the stochastic variation satisfies the standard deviation of the velocity, Equation (3.44). The random numbers are computed for every particle injection.

$$\mathbf{u}_p = \langle \mathbf{u}_p \rangle + \xi \mathbf{u}' \quad (3.44)$$

where $\xi \in \{-1 : 1\}$ is a normally distributed random number.

In case that no experimental data for the particle velocity are available, it is assumed that particles start with the instantaneous fluid velocity at the position of particle injection.

Outlet Boundary

The particle tracking algorithm aborts the integration when a parcel crosses the outlet boundary. The mass of the parcel is excluded from the total particle mass in the computational domain.

Wall Boundary

For all configurations presented here the interaction of a particle with a wall boundary is expressed as a particle-wall collision. The particle is rejected from the wall when the computed path of the mass point crosses the wall. The angle of reflection is computed as a function of the velocity vector before the collision and the coefficient of restitution, e , where $e = 1$ denotes a fully elastic collision, (Equation (3.45)).

$$u_{n0} = -u_{n1}e \quad (3.45)$$

$$u_{t0} = u_{t1}e \quad (3.46)$$

The indexes n and t denote the particle velocity in wall-normal direction and tangential to wall respectively. The second pair of indexes denote the velocity before, state 0, and after, state 1, the collision with the wall.

4 Reference Configurations

This chapter gives an overview of the configurations to be discussed in Chapters 5, Code Validation, and 6, Results and Discussion. The necessity arises from the arrangement of the following chapters, which discuss mainly phenomenological aspects under different boundary conditions resulting from the different flow configurations.

Together with the exposition of the investigated configurations this chapter contains the numerical setup applied to the simulations.

4.1 Low Reynolds Number Particle Laden Channel Flow

The flow in this configuration is rendered between two parallel plane walls. The extension of the wall boundaries is supposed to be infinite. Therefore, flow inhomogeneities develop only in the wall-normal direction. The carrier fluid is contaminated with small heavy particles. The REYNOLDS number, based on the wall friction velocity and the channel half height, is $Re_\tau = 150$. The intention of this simulation is to investigate the main properties of the dispersed phase, such as particle velocities, particle dispersion and the propensity to accumulate in the near-wall region, depending on particle diameter. Beyond this, the LES results are compared with reference DNS from Picciotto et al. [70].

4.1.1 DNS Setup

In Picciotto et al. [70], Direct Numerical Simulation (DNS) is applied to the carrier phase and the motion of the particles is computed from the NEWTON equation of motion. It should be noted that the DNS is part of a benchmark test of a particle-laden turbulent channel flow, as reported in Marchioli et al. [56].

The fluid is assumed to be incompressible and NEWTONIAN. A sketch of the computational domain, with channel half height h as a scaling parameter, is presented in Figure 4.1.

The properties of the flow and relevant configuration variables are summarized in Table 4.1. The friction velocity is defined as $u_\tau = \sqrt{\tau_w / \rho_f}$, where τ_w and ρ_f are the mean shear stresses at the wall and of the fluid density, respectively. The existing near-wall turbulent structures seem to partially match the characteristic time scales of the chosen particle size and are therefore responsible for the preferential particle concentration in this region.

Re_τ is the REYNOLDS number based on the wall friction velocity u_τ and the channel half height. Re_{bulk} is based on the mean bulk velocity. The behavior of four classes of particles is investigated. The particle properties, also in respect of the specific flow conditions are listed in Table 4.2. Further, the diverse particle classes are addressed by their STOKES number. The St

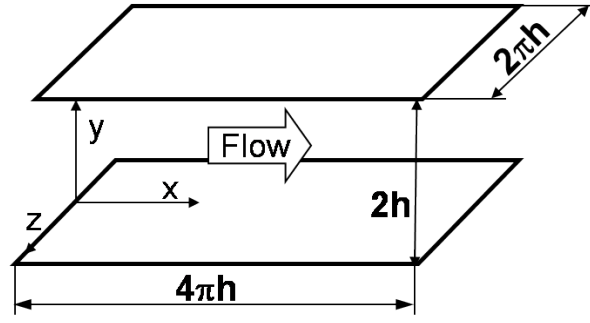


Figure 4.1: Sketch of the channel flow domain for the DNS.

Table 4.1: General configuration and flow properties.

Channel half height, h	0.02	m
Friction velocity, u_τ	0.11775	m/s
Re_τ	150	—
Re_{bulk}	2110	—
Fluid density, ρ_f	1.3	kg/m^3
Fluid viscosity, ν_f	$1.57 \cdot 10^{-5}$	m^2/s
Particle density, ρ_p	$770\rho_f$	kg/m^3

and d^+ are defined as:

$$St = \tau_p \frac{u_\tau^2}{\nu_f} \quad (4.1)$$

$$d^+ = d \frac{u_\tau}{\nu_f} \quad (4.2)$$

where τ_p is the STOKESIAN particle response time, as defined in Equation (2.48).

The NAVIER-STOKES equations are solved using a pseudo-spectral method. Details of the numerical procedure can be found in Lam and Banerjee [49]. The domain for the DNS is discretized with $128 \times 128 \times 128$ nodes in all three directions. In stream- and spanwise directions periodic boundary conditions are imposed on the fluid velocity field, together with a pressure gradient in streamwise direction to retain the flow. A no-slip boundary condition is applied at the walls.

The concentration of the particles is assumed to be low enough to consider one-way coupling conditions, according to the definition in Section 2.2.1. Particle-particle interactions are also neglected. The motion of the ensemble of 10^5 rigid spherical particles is resolved with a set of ordinary differential equations (Equation (2.53) and Equation (2.54)). Since $\rho_p/\rho_f \geq 1$, the only significant forces are drag force and buoyancy (Elghobashi et al. [26]). Gravity is also neglected in this simulation. The drag force includes a standard correction for particle REYNOLDS numbers lower than 1000, as shown in Equation (4.3).

Table 4.2: Particle properties.

$St = \tau_p^+$	$\tau_p (s)$	d_p^+	$d_p (\mu m)$	St_η	St_l
1	$1.13 \cdot 10^{-3}$	0.15	20.4	0.08	0.012
5	$5.66 \cdot 10^{-3}$	0.34	45.6	0.4	0.06
25	$2.83 \cdot 10^{-2}$	0.77	102.0	1.9	0.3
125	$1.42 \cdot 10^{-1}$	1.71	228.0	9.6	1.5

$$\frac{d\mathbf{u}_p}{dt} = \frac{\mathbf{u}_f - \mathbf{u}_p}{\tau_p} (1 + 0.15 Re_p^{0.687}) \quad (4.3)$$

Similar to the fluid boundary conditions, a periodic type of boundary is applied to the particle velocity and position when a particle leaves the domain in a stream- or spanwise direction. Following the standard LAGRANGIAN approximation, particles of finite size are replaced by mass points. The boundary condition for the particle approaching a wall is defined as follows: When the distance between particle position and the wall becomes smaller than the physical radius of the particle, the particle rebound elastically from the wall.

The particle-laden flow is computed for approximately $400 \cdot t_R$, where t_R is the mean flow residence time, defined by the domain length in streamwise direction and the mean centerline velocity. During the last 20000 flow time steps, which corresponds to approximately $17 \cdot t_R$, particle velocity and position data are collected every 50 time steps to build up the database for the particle properties. Finally, from the extracted particle data, one-point statistics for velocity and particle number density are used to analyze the preferential particle accumulation.

4.1.2 LES Setup

Domain and physical properties

The computational domain for the large-eddy simulation is reduced to a quarter of the original domain of the DNS by considering the half length and width of the primary domain. At the relatively low REYNOLDS number the correlation coefficient does not drop to zero. Nevertheless, the domain extension is sufficient to reproduce the fluid and particle one-point statistics, as the comparison with the DNS confirms. The domain axes are as follows: x- in streamwise, y- in wall-normal and z-axis in spanwise direction. The spatial resolution in stream- and spanwise directions is equidistant and in the wall-normal direction, the mesh is stretched using a Poisson function, with growth factor of 1.05. Table 4.3 contains the mesh size normalized by wall variables. Δy_c^+ denotes the grid size in the centerline plane of the channel, and Δy_1^+ - the size of the wall next cell. In addition to the two-phase flow simulation, for the purpose of validating, the simulation of the single phase flow is carried out on three different numerical meshes.

The two-phase LES is performed on the *medium* grid. The current two-phase flow simulation setup computes 15 times more particles than those for the reference DNS. The number of the

Table 4.3: Mesh resolution for the large-eddy simulation .

Grid label	Grid points	Δx^+	Δy_1^+	Δy_c^+	Δz^+	Grid points below $y^+ = 10$	Time step, s
<i>coarse</i>	$58 \times 60 \times 58$	16.2	0.6	11.7	8.0	9	$5e - 3$
<i>medium</i>	$72 \times 74 \times 72$	13.0	0.5	10.7	6.5	15	$1e - 3$
<i>fine</i>	$88 \times 90 \times 88$	11.0	0.6	7.7	5.4	15	$5e - 4$

particles does not change the two-phase flow behavior since inter-particle collisions are neglected and only one-way coupling is considered. Therefore, the simulated time and thus the time for sampling particle properties is shorter. The full details concerning the differences of the DNS vs. the LES are summarized in Table 4.4. As defined in Chapter 4.1.1, t_R denotes the flow residence time.

Table 4.4: Summary DNS vs. LES setup.

Case	Physical domain	Numerical method	STOKES number, St	Particles number	Simulated time	Sampled time
DNS	$4\pi h \times 2h \times 2\pi h$	pseudo-spectral	1, 5, 25, 125	10^5	$400 \cdot t_R$	$17 \cdot t_R$
LES	$2\pi h \times 2h \times \pi h$	finite-volume	1, 5, 25	$15 \cdot 10^5$	$400 \cdot t_R$	$4 \cdot t_R$

Boundary and initial conditions

Periodic boundary conditions are applied in streamwise and spanwise directions for both the continuous and the dispersed phases. Particles are reflected elastically when the particle center reaches the wall. Pressure gradient in x-direction is applied to retain the flow. The initial field of the air flow is taken from a steady state $k - \epsilon$ simulation. The averaged velocity field has been superimposed with random fluctuations to accelerate the development of the turbulent field in the large-eddy simulation. The two-phase flow simulation starts from the fully developed turbulent single phase flow. The particles are initially homogeneously distributed within the domain. Initial particle velocity is the fluid velocity interpolated at the particle position. Since only one-way coupling is considered for the LES, similar to the reference DNS, the number of particles does not have an influence on the particle distribution and accumulation, whereas larger number of particles accelerate the convergence of the statistical particle properties, such as mean and rms¹ velocity or particle number density. Hence, significantly larger number of particles compared with the reference DNS setup are simulated (Table 4.4).

¹root mean square

The numerical procedure

The solution of the NAVIER-STOKES equations for the continuous phase is based on the Finite Volume Method. A second order spacial discretization scheme, CDS, is applied for the convective terms in the momentum Equation (2.5) and the PRESTO! scheme for the face pressure interpolation in the pressure-correction equation together with a node based procedure for the gradient approximation. For details of the numerical procedure see, Section 3.1. The time integration is performed by a second order implicit scheme. The pressure-velocity coupling is realized via a Fractional Step method. The latter is discussed in detail in Section 3.1.2. The sub-grid stress tensor, within the scope of the large-eddy simulation, is modeled using the Smagorinsky model with dynamic estimation of the model constant.

Particle tracking is initialized after the single phase flow has reached a statistically steady state. Particle motion is controlled by the drag force, assuming that the $Re_p < 1000$. A second order interpolation scheme is used to determine the fluid velocity at particle position. The integration in time of the particle equation of motion is evaluated applying an adaptive scheme, which switches between a 1st order EULER implicit and 2nd order trapezoidal scheme. Details of the numerical methods for particle tracing can be found in Section 3.2.

4.2 High Reynolds Number, Particle-Laden Channel Flow

The experimental setup for this case has been developed and used for numerous measurements of particle-laden turbulent channel flows using various parameters, such as particle diameter, particle mass loading and channel wall roughness. The REYNOLDS number based on the wall friction velocity and the channel half height, is $Re_\tau = 644$. The experimental investigations in a vertical channel gas-solids flow by Kulick et al. [48] and Fessler et al. [31] are used as a reference case. The experiment focuses on particle dispersion by examination of different STOKES numbers and on turbulence modification due to STOKES number variation combined with mass loading variation.

As a potential simulation task some important features of the configuration require special attention:

- $Re_{U_{CL}} = 13800$ significantly higher than the configuration in Section 4.1
- Moderate particle mass loading, which affects the carrier phase properties:
 - Importance of two-way coupling,
 - Particle size vs. volume of the numerical cell in the near-wall region,
- Effect of the gravitational force,
- Further specific properties of the experiment:
 - Wall roughness,
 - Stage of development of the statistically steady two-phase flow up to the test section,

- Particle diameter distribution instead of single diameter class,
- Experimental errors.

4.2.1 Experimental Setup and Measurement Technique

Experimental facility

A vertical square duct is used to deliver the particle-laden gas flow. The vertical part of the wind tunnel includes a 5.2 m development section. The particle feeder and the flow conditioning section are placed above the vertical part of the channel. The specially designed belt feeding system delivers for homogeneous particle distribution in the transverse direction. The particle-laden flow goes through a channel contraction before entering the development section, with dimensions of the cross section of $0.04 \times 0.457\text{ m}$, which results in an aspect ratio of $1 : 11.4$. The acrylic test section has a length of 0.635 m .

Physical properties

The flow is operated with air at ambient temperature and at a REYNOLDS number of 13800, based on the channel half height (0.02 m) and the centerline velocity. Further important gas phase parameters are summarized in Table 4.5. The KOLMOGOROV length scale and the turbu-

Table 4.5: Gas flow parameters.

Channel half hight, h	0.02	m
Centerline velocity, U_{CL}	10.5	m/s
REYNOLDS number, $Re_{U_{CL}}$	13800	—
Shear wall velocity, u_τ	0.49	m/s
Shear REYNOLDS number, Re_τ	644	—
Viscouse length scale	31	μm
Dissipation, ϵ , centerline	2.8	m^2/s^3
Kolmogorov length scale, η , centerline	190	μm
Kolmogorov time scale, $(\nu/\epsilon)^{1/2}$, centerline	2.3	ms

lence dissipation are estimated from a $k - \epsilon$ simulation, [31].

The dispersed phase is represented by solid particles of different material and size. Thus, the variation of the particle's STOKES number is controlled by two parameters - particle density and diameter. One of the main purposes of the experimental investigation is to examine the turbulence modification in the fluid arising from the presence of the particles. Therefore, the particle mass fraction, as a key parameter for turbulence modulation, is also varied within a given set of particle parameters. Table 4.6 presents the setup variations for the two-phase flow . The corrected particle relaxation time is calculated by integrating the particle equation of motion for

Table 4.6: Particle parameters.

Mean diameter (Std. dev.), d_p	μm	28(—)	50(± 3)	70(± 12)	90(± 4.5)	150(± 10)
Material		Lycopodium	glass	copper	glass	glass
Density, ρ_p	kg/m^3	700	2500	8800	2500	2500
Mass loading, ϕ	%	3	2, 20	2, 20	2	20
Averaged volume fraction, α_p	—	$5.25 \cdot 10^{-5}$	$9.8 \cdot 10^{-6}$, $9.8 \cdot 10^{-5}$	$2.7 \cdot 10^{-6}$, $2.7 \cdot 10^{-5}$	$9.8 \cdot 10^{-6}$	$9.8 \cdot 10^{-5}$
STOKES τ_p	ms	1.7	19	130	63	167
Corrected τ_p	ms	1.7	18	95	43	94
St_η	—	0.74	8	41	19	40.8
St_L	—	0.05	0.57	3	1.4	3
Case label		$d28\phi03$	$d50\phi02$, $d50\phi20$	$d70\phi02$, $d70\phi20$	$d90\phi02$	$d150\phi20$

a particle in a uniform unbound flow, assuming $Re_p < 100$.

Experimental technique

A single-component Laser Doppler Anemometry (LDA) is applied to measure the streamwise and spanwise velocity components of the continuous and dispersed phase. The optical path for measuring of the streamwise velocity component was oriented in a spanwise direction (along the long side of the channel cross section) in case there was low particle mass loading, which ensures a very good spatial resolution near the wall. With increasing particle mass loading, the signal-to-noise ratio decreases and the optical axes are aligned with the direction of short side of the channel cross section (in this work, this is referenced as wall-normal), which results in poorer spatial resolution near the wall.

Particle velocity is measured without using a tracer in the air flow. Gas-phase velocity in particle-laden flow is measured by amplitude discrimination, since the amplitudes of the laser Doppler bursts of the scattered light from large and small particles are very different. Titanium dioxide powder with mean diameter of $1\mu m$ was used as a flow tracer.

Data rates for the air flow velocity range from 3000 Hz for the single phase and lowest particle mass loading down to 100 Hz for the highest mass loading of 80% . Particle velocity data rates increase with the mass loading and are between 20 and 40 Hz . For the spectral analysis of the gas flow, the data rate is increased to 6000 Hz by setting the seed flow rate to its maximum. The minimum spatial resolution is defined by the cylindrical measurement volume, which has a diameter of $78\mu m$ and a length of $562\mu m$.

According to the authors of [47, 31], considering directional bias, gradient broadening, velocity bias, ensemble statistical errors and alignment uncertainties, the combined experimental uncertainty is estimated as 2% in the mean and 5% in the standard deviation of the velocity. Interphase cross-talk error is 1% in the mean velocity and 3% in its standard deviation. The error in the particle velocity is caused by the varying particle diameter. For the glass particles (Table 4.6), it results in a standard deviation in the velocity of approximately 0.03 m/s and 0.2 m/s for the copper particles.

Particle concentration and possible preferential accumulation are analyzed using quantitative estimation of the particle distribution in the channel central plane from photographs. For this reason, particles are illuminated by a laser sheet with a thickness of 1 mm , parallel to the plane defined by the span- and streamwise axes, and placed at channel half height. The photographs represent an area of $30 \times 40\text{ mm}$. Depending on the mass loading and particle diameter, the number of particles per photograph is in the order of 3000. 10 – 15 photographs are used for the concentration estimation. A detailed description of the experimental technique and estimation procedure is in [31].

4.2.2 Numerical Setup

Domain and physical properties

The high aspect ratio of the real channel cross section allows approximation of the real flow such as the assumption of a two-dimensional flow between two endless flat planes, where its behavior in spanwise and streamwise direction is supposed to be periodic. This assumption

allows for an artificial but significant reduction of the volume reproduced in the numerical simulation. The domain extensions are $2\pi h \times 2h \times \pi h$, where $h = 0.02\text{ m}$ represents the channel half-height. The domain axes are as follows: x - in streamwise, y - in wall-normal and z -axis in spanwise direction. Two discretizations in the wall-normal direction aim to investigate the effect of the resolution of the wall boundary layer on the particle properties. The first grid allows for a standard resolution (in LES context) of the boundary layer, where the wall next point is below $y^+ = 1$. The second grid has an equidistant cell distribution in wall-normal direction, so that the wall next point is at $y^+ = 15$ and additional modeling of the wall generated turbulence is required. Details for the two numerical grids are summarized in Table 4.7. Δy_c^+ denotes the grid size in y -direction of the centerline plane in the channel, and Δy_1^+ - the size of the wall next cell.

Table 4.7: Numerical grid parameters

Case	Grid points	Δx^+	Δy_1^+	Δy_c^+	Δz^+	Grid point below $y^+ = 10$	Time step, s
Wall-resolved	$129 \times 100 \times 129$	31	0.6	33	15	9	$5.e - 5$
Wall function	$129 \times 83 \times 129$	31	15	15	15	-	$5.e - 5$

The physical properties for air and particles are kept as defined for the experiment, except for the assumption that each particle class is mono-dispersed. The particle size is set to the mean diameter of the particular particle set.

Boundary and initial conditions

Periodic boundary conditions are applied in streamwise and spanwise directions for both the continuous and dispersed phases. For the periodic boundaries on the fluid side, the chosen domain extensions are supposed to be large enough that the two-point velocity correlation becomes zero within the domain. The pressure gradient in streamwise direction retains the flow parallel to the gravity vector. Gravity also acts on the dispersed phase, together with the drag force induced by the carrier fluid. The influence of the dispersed phase on the fluid properties, i.e. two-way coupling, is considered by utilizing a source term in the momentum Equation (2.5). No additional treatment is applied to model the influence on the subgrid-scale tensor. A no-slip condition is applied at the wall for the air flow. Particles reflect elastically when the particle center reaches the wall. The effect of inelastic collision is investigated in the case of copper particles by setting the restitution coefficient in wall-normal direction to 0.5. It is important to note that, the value of the restitution coefficient chosen here is a very rough estimation because of missing data for the colliding material pair, glass - copper. For comparison, the estimated restitution coefficient for the pair copper-copper is approximately 0.22 and for the pair glass-glass it is about 0.94.

The initial field of the air flow is taken from a steady-state $k - \epsilon$ simulation. The averaged velocity field has been superimposed with random fluctuations to accelerate the development

of the turbulent field in the large-eddy simulation. The two-phase flow simulation starts from the fully developed turbulent single phase flow. The particles are injected with a homogeneous distribution into the domain, with velocity equal to the fluid velocity at the particle position. This is computed using a second order interpolation based on the CFD grid centroids velocity data.

The numerical procedure

In general, the numerical procedure followed is the same as that outlined in Section 4.1.2. The effect of the pressure-velocity coupling on the simulation quality is investigated by comparing of the Fractional Step method with the standard SIMPLE coupling procedure. To retain as much similarity with the experiment as possible, the gravitational force is considered for both the air flow and the dispersed phase.

Configurations

The choice of the simulated setups allows the investigation of the potential of large-eddy simulation coupled with LAGRANGIAN particle tracking in two key aspects: particle preferential concentration and particle influence on fluid turbulence characteristics. Modification of turbulence due to the presence of particles is referred to as turbulence modification. The results from the simulations are split into two groups, as shown in Table 4.8, based on their fundamental interaction phenomenon. One group focusses on the preferential concentration of particles as induced by the turbulent flow. The second targets the turbulence modification by the particulate flow. The results of the two groups are discussed in separate sections in Chapter 6.

Table 4.8: Topic map of the simulated cases.

Topic	Relevant Configuration
Particle preferential concentration	$d28\phi03$, $d50\phi02$, $d70\phi02$, $d90\phi02$
Turbulence modification	$d50\phi02$, $d50\phi20$, $d70\phi02$, $d50\phi20$, $d150\phi20$

Detailed information about the simulation conditions for the single and two-phase flows are listed in Table 4.9. t_R denotes the residence time, here defined as the ratio of channel length to centerline mean streamwise velocity, $2\pi h/U_{cl}$. As well as the configurations performed in the experiment due to variation in particle diameter, material or mass loading, a number numerical variations are also performed. These are listed in Table 4.9 as well. The first variation considers the number of real particles per numerical particle (also denoted as a parcel):

- Every numerical particle represents only a small fraction of a real particle, ($< 10\%$ depending on material and mass loading). The following injection procedure is applied: Particles are released from a plane normal to the main flow direction, with 129×100 homogeneously distributed injection positions. The particles are injected at equidistant time intervals, so that the final particle distribution throughout the domain is nearly homogeneous. The duration of the injection is governed by the desired number of numerical particles. In this case, the limit is set to 516000 numerical particles.

Table 4.9: Simulation parameters.

Case label	Simulated time	Sampled time	Parcel number $\times 10^3$	Number in Parcels
single phase	$160 t_R$	$80 t_R$	—	—
$d28\phi03$	$160 t_R$	$80 t_R$	1362.8	1
$d50\phi02$	$160 t_R$	$80 t_R$	516	0.0008
$d70\phi02$	$160 t_R$	$80 t_R$	516	0.008
$d70\phi20$	$160 t_R$	$80 t_R$	516	0.08
$d70\phi20 - nip1$	$160 t_R$	$80 t_R$	47.06	1
$d70\phi20 - \epsilon0.5$	$160 t_R$	$80 t_R$	47.06	1
$d90\phi02$	$100 t_R$	$50 t_R$	516	0.005
$d150\phi02$	$100 t_R$	$50 t_R$	250	0.02
$d70\phi20 - simple$	$132 t_R$	$80 t_R$	47.06	1

- One numerical particle represents exactly one real particle. To achieve this, particles are released from the same cross-sectional plane as above but in accordance with the mass flow and the additional restriction that, every parcel contains the mass of one real particle. The duration of the injection is limited by the averaged volume fraction, estimated by the particle and mass loading case. Particle positions are randomized for every injection event using a normal distribution to achieve a nearly homogeneous particle distribution throughout the domain.

The effect of the number of numerical particles on flow characteristics has been investigated for the configuration of copper particles at 20 % mass loading.

The second numerical variation considers the choice for pressure-velocity coupling algorithm. The case $d70\phi20$ has been computed using the Fractional Step method and the standard SIMPLE method, referred to as $d70\phi20 - simple$, and compared for fluid and particle properties. The choice of the configuration is based on the expectation that higher particle mass loading can affect the stability and convergence of a simulation in a negative manner when considering the two-way coupling. It needs to be proven that the Fractional Step method, which includes various numerical simplifications and thus is computationally much more efficient, is nevertheless capable of dealing with the higher mass loadings.

4.3 Particle-Laden Jet

Particle and fluid behavior are investigated for an unconfined air jet flow with and without particles. This configuration is an application of interest for several reasons:

- The phase interaction is not a function of the geometrical rig, (no wall effects),

- Variation in the characteristic time and length scales within the flow, i.e. the local STOKES number changes,
- The carrier fluid demonstrates a strong response to the dispersed phase and changes its behavior significantly compared to the single phase case.

For this reason, fluid and particle velocity as well as the particle concentration distribution function are the focus. Spatial and temporal autocorrelation functions of the fluid velocity and their spectral representation give an insight into the mechanisms of phase-interaction.

Another important feature of this configuration is its similarity to a broad range of industrial applications. A number of examples from industrial praxis include a two-phase jet flow, related to a spray. Such are the fuel injection in combustion chambers, spray painting or chemical units. Since the dispersed phase in the present case of interest is represented by solid particles, the phase-interaction here is limited to momentum exchange. The study of the isolated phenomenon should facilitate better understanding.

The following sections give an overview of the experimental rig built and investigated by Hardalupas et al. [37], as well as a summary of all numerical simulations performed that relate to this configuration.

4.3.1 Experimental Setup and Measurement Technique

Experimental facility

The experimental rig is oriented vertically, referred to here as the z -axis, and the main flow direction is parallel to the gravity vector. A pressure regulator keeps a constant air flow rate for the jet, independent of fluctuations in the supplied pressure. Rotameters control the flow rate of the glass beads and the tracer particles. Streams of particles and air flow are mixed upstream in a vertical duct, which, transformed via smooth contraction, ends in a development section. The latter is a stainless steel pipe with diameter $D = 0.015 \text{ m}$ and length of $L = 100D$. The flow exits into ambient air. A flow collection hopper is placed 50 pipe diameters further downstream. Measurements are performed between axial positions of $x/D = 0.1$ and 28.

Physical properties

Table 4.10 and summarize the physical properties of the carrier fluid and 4.11 those for the dispersed phase.

Table 4.10: Gas flow parameters at $x/D = 0$.

Jet diameter , D	0.015	m
Centerline velocity, U_0	14.7	m/s
Bulk REYNOLDS number, Re_{bulk}	13000	—
Integral time scale, t_0	1.15	ms

Table 4.11: Particle parameters.

Mean diameter, d_p	μm	40	80
Diameter range	μm	37 – 44	60 – 95
Density, ρ_p	kg/m^3	2420	2420
Mass loading, ϕ	%	13	23, 86
Averaged volume fraction at $x/D = 0$, α_p	—	$6.37 \cdot 10^{-5}$	$1.12 \cdot 10^{-4}$, $4.3 \cdot 10^{-4}$
STOKES τ_p	ms	11.9	47.6
St_{l_0}	—	10.3	41.4
corrected τ_p	ms	11.1	45.7
$St_{l_0,corr}$	—	9.65	39.7

Two particle residence times are denoted in Table 4.11. τ_p assumes Stokesian flow and its corrected value of is estimated using the empirical correlation as given by Schiller and Naumann [88] for particle $Re_p < 1000$. The correlation is provided in Equation (2.58). The STOKES number in Table 4.11 is based on the fluid integral time scale. The characteristic time scales of the particles are significantly higher than the integral time scale of the flow at the jet inlet. Therefore, the particles will not respond to the fluid motion. According to Hardalupas et al. [37] the centerline integral time of the flow increases quadratically, i.e. at thirty diameters downstream, the l_0 approximates $1.35 ms$. The change in the local STOKES number along the centerline is less than 15% of the initial value at $x/D = 0$, (Table 4.11).

Experimental technique

The one-point Phase-Doppler-Anemometry (PDA) experimental technique is used to measure spray and carrier fluid. The Phase-Doppler anemometer is mounted on a three-dimensional traversing system, and is used to measure the axial and radial velocity components in space. The position of the receiving module is 30° off-axis from the main scattering direction. The receiving module is mounted on the same traversing system as the transmitting rig. The cylindrical measuring volume seen by the receiving optic has a length of $1.13 mm$ (imaged length $200 \mu m$) and a radius of $52 \mu m$. Involving three photomultipliers guarantees that the phase difference and the estimation of the particle diameter is unambiguous. Various refractory powders, such as kaolin and titanium dioxide, are used as a seeding material. The nominal size of the powders before agglomeration is $\approx 1 \mu m$. The seeding particles are assigned to a phase window of 40° .

The estimation of the axial mean and rms velocity relies on approximately 3000 total samples. The largest portion of the random error due to the size of the data sample set is appraised to 1 % for the mean and 3 % for the rms velocity for particles and gas flow. The measurement of the particle mass flux includes about 3 % random uncertainties. A discussion of the error sources and the error magnitude is in Hardalupas et al. [37].

4.3.2 Numerical Setup

Domain and physical properties

According to the sketch of the computational domain in Figure 4.2, the main flow direction is the x -axis. Using the jet diameter D at the jet inlet, $x/D = 0$, as a parameter, the main computational domain represents a cylinder with a radius of $10D$ and length of $30D$. A fragment of the development section with length of $5D$ is included in the simulation. From totally 1.320 million cells, 1.1445 million are in the main computational domain. The inlet pipe section is discretized with approximately 0.175 million cells. Within the inlet pipe section, ten prism layers are used to resolve the wall boundary layer. The wall next cells are placed at $y^+ = 6.6$ (the distance is normalized using wall units). The complete domain is discretized with hexahedra. 90 % of all hexahedra have an aspect ratio less than 10. The grid is stretched in x -direction by a factor of 1.01. The grid generation is based on the *cooper* algorithm, which is available in the meshing tool GAMBIT. The main advantage of the technique is that only one surface needs to be meshed manual. The computational volume is discretized automatically by sweeping the prepared surface mesh. Geometrical functions control the minimum and maximum cell volume, together with the growth rate of the cells.

The physical properties for air and particles for the simulation are kept as defined for the experiment, except for the assumption that all particle classes are mono-dispersed and have a mean diameter of $40\ \mu\text{m}$ and $80\ \mu\text{m}$ respectively. Details can be found in Tables 4.10 and 4.11.

Boundary and initial conditions

Figure 4.2 presents a sketch of the computational domain together with the boundary conditions prescribed. A DIRICHLET boundary condition for the air velocity is applied at the pipe inlet,

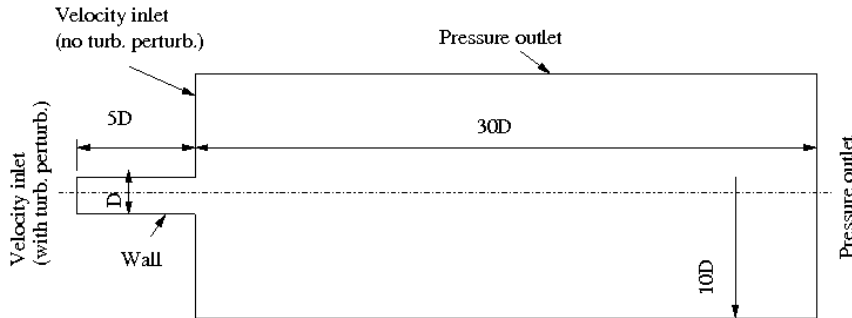


Figure 4.2: Boundary conditions: continuous phase.

where the velocity components normal to the main flow direction are set to zero. In order to induce a turbulent flow within the short pipe section, velocity fluctuations are generated using a LAGRANGIAN Vortex Method. For details of the method see [58] and Chapter 3.1.3). The fluctuation generation is based on the information for the turbulent flow state provided by profiles for the turbulent kinetic energy and dissipation or the turbulent intensity. Profiles for the velocity and turbulent quantities are taken from a preliminary steady-state $k - \epsilon$ simulation of a pipe flow with the same REYNOLDS number as for jet at $x/D = 0$. The profiles of the axial mean velocity and turbulent kinetic energy used at the inlet for the LES and the velocity data

from the experiment of the single phase flow measured at $x/D = 0.1$ are compared in figure 4.3.

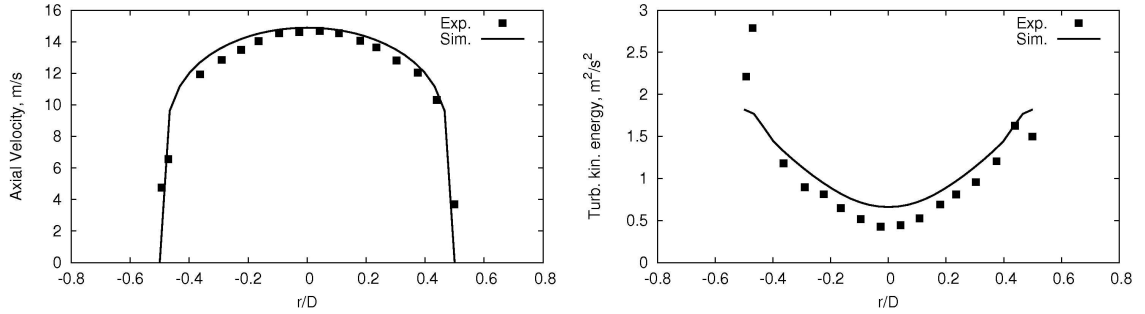


Figure 4.3: Radial profiles of axial velocity and turbulent kinetic energy from the $k - \epsilon$ simulation, used for inlet condition for the LES, vs. experimental data at $x/D = 0.1$.

The second region with Dirichlet boundary type for the velocity has the function of a coflow. In the main flow direction (z-axis), the flow velocity is set to 0.2 m/s to prevent a numerically induced backflow and hence to increase the numerical stability. No additional flow perturbations are set to generate turbulence. For both the outlet boundaries in axial and radial directions, a pressure condition accounts for the zero gauge pressure and zero gradient condition for the velocity field.

The dispersed phase is injected continuously at the pipe inlet at $x/D = -5D$. Particles enter the domain homogeneously distributed. Their starting positions for every time step are randomly staggered at the inlet plane. Particles are injected with the condition number in parcel (NiP) being unity, i.e. one numerical parcel represents one real particle. The restriction was made after preliminary calculations with $40 \mu\text{m}$ particles at $NiP < 1$. These have shown that the number of the parcel increases above 10 million even before the statistically steady state has been reached. The opposite option $NiP > 1$ was found to generate a too low number of particles, which will increase the computational time required to collect a sufficient number of samples for statistical evaluation. The particle velocity is set equal to the fluid velocity interpolated to the starting particle position. The particle axial velocity component is corrected by a factor less than unity in such a way that the ratio of the particle to fluid axial velocity is very close to that obtained from the experiment at $x/D = 0.1$. The factor was set to a constant value within the particle injection plane. The computed particle velocity at the first measurement position matches the experimental profile well. For this reason, no further adjustment for the particle inlet velocity profile was found to be necessary. The factors for the different configurations are listed in the last column of Table 4.13.

Within the inlet section, particles rebound elastically from the wall. Particles crossing an outlet boundary are marked as escaped and finally excluded from the tracking procedure.

For the single phase flow simulation, the solution of a steady-state $k - \epsilon$ calculation is applied as initial flow state. All two-phase simulations start from the statistically steady solution of the single phase LES.

The numerical procedure

In general the numerical procedure is the same as that outlined in Section 4.1.2. For quality assessment of the LES also simulations applying the SIMPLE algorithm are compared with the primary results to verify the validity of the Fractional Step method and its simplifications for this case.

The action of gravity is included for both phases. Two-way coupling is accomplished via source term in the gas momentum equation.

Configurations

The first set of calculations concerns the validation of the single phase flow simulation. The investigations span in three directions: domain resolution, dependence on the pressure-velocity coupling and dependence on the inlet boundary conditions. Details are summarized in Table 4.12.

Table 4.12: Simulation parameters: Single phase flow simulations.

Grid	Case	Total time	Sampled time	min. / max. CV, m^3	max. cell aspect ratio
1.320 Mil. CV	FS ¹⁾ - U_{const}	$18 t_R$	$8 t_R$	$4.e - 11 / 2.45e - 7$	20
	FS- $U_{profile}$	$11^2) t_R$	$8 t_R$	see above	see above
	SIMPLE- U_{const}	$8^2) t_R$	$6 t_R$	see above	see above
1.762 Mil. CV	FS- $U_{profile}$	$6^3) t_R$	$4 t_R$	$1.5e - 10 / 1.1e - 7$	6

1) FS – Fractional Step algorithm

2) initial field from FS- U_{const} run

3) initial field from FS- $U_{profile}$ run

Two-phase flow simulations are primarily used to study particle dispersion along the jet in terms of the local STOKES number. They are also used to investigate the influence of particles on fluid motion. The coarser grid according to Table 4.12 is used for all two-phase flow simulations. With the corresponding case FS- U_{const} , simulations concerning the coarse particle class are performed also utilizing the two concurring types of pressure velocity coupling: SIMPLE and Fractional Step. The focus here is on investigating the stability and quality of the LES, when a significant amount of inter-phase momentum exchange occurs. Table 4.13 lists detailed information related to the two-phase flow simulations. The sampling procedure for statistical estimation of the two-phase simulations begins after the particle concentration, integrated over the entire domain, reaches its quasi-stationary value. Depending on particle diameter and mass loading, the initial time range is different for the different configurations, as evident in Figure 4.4. The time axis is normalized with the flow residence time t_R , which is defined as the ratio of the domain length $L = 30D$ to the mean jet centerline velocity U_{CL} at $x/D = 0$. As expected, the mass concentration of the larger particles converges toward an asymptotic value faster than

the concentration of the lighter particles. These respond faster to the fluid motion. The resulting increase in the particle lateral dispersion leads to longer particle residence times within the computational domain. Finally, the statistically steady state of the particle concentration is reached when the injected and the domain-leaving particle number reaches its equilibrium state. Variation of the mass loading in case $d80\phi23$ and case $d80\phi86$ affects only the magnitude of the total concentration, not time passing until this value is reached.

Table 4.13: Simulation parameters: Two-phase flow simulations.

Case	Pressure - Velocity Coupling	Total time	Sampled time	Particle num- ber $\cdot 10^3$	$\frac{u_{ax,p,bulk}}{u_{ax,f,bulk}}$
single phase	FS	$18 t_R$	$8 t_R$	—	—
	SIMPLE	$10 t_R$	$8 t_R$	—	—
$d40\phi13$	FS	$18 t_R$	$10 t_R$	550	1
$d80\phi23$	FS	$16 t_R$	$10 t_R$	62	1
	SIMPLE	$10 t_R$	$8 t_R$	62	1
$d80\phi86$	FS	$16 t_R$	$10 t_R$	248	0.75
	SIMPLE	$6 t_R$	$4 t_R$	248	0.75

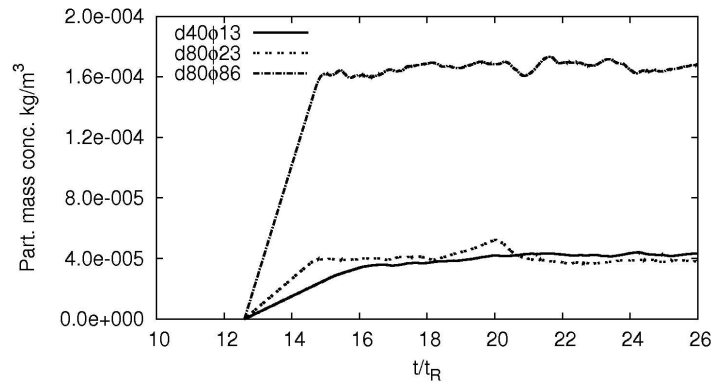


Figure 4.4: Particle mass concentration within the computational domain as a function of time.

4.4 Evaporating Spray in a Confined Circular Chamber

Additional aspect of interest are high fidelity simulations of combustion systems with liquid fuels. Being successful in these implies an accurate prediction of droplet dispersion and evaporation. In order to investigate this particular phenomenon, the next configuration is chosen, as experimentally investigated by Sommerfeld and Qiu [99]. The experiment exhibits some

similarity with technical applications, where liquid fuel evaporation is one of the leading mass and energy transfer mechanisms. Nevertheless, it has to be emphasized that a low-temperature spray problem is investigated in the present configuration. Hence, the vaporization rate is not the limiting factor for species mixing as is usual in common spray combustion.

Within the scope of the present work, the configuration contains three major aspects of interest: First, the diameter distribution of the spray covers a range of three orders of magnitude, starting from two micrometers. The mesh requirement for a high fidelity LES leads to a locally very fine grid resolution, especially for higher Reynolds numbers of the flow. Using the Lagrangian approach for the dispersed phase in the case of a two-phase simulation, the numerical grid issue often conflicts with the assumption that the discrete particles are small compared to the volume of the computational cells. Secondly, near the spray injection plane the particle volume fraction is significantly higher compared to all previously discussed configurations in this work. Finally, the process of evaporation is an additional issue that needs to be modeled.

The particular charm of the setup is the detailed database of the inlet spray and air conditions. It contains besides one point statistics for velocity, mass flux and temperature, probability density functions (PDF) of droplet diameters and diameter - droplet velocity correlations at several radial positions close to the nozzle exit. Further, there is an extensive database of the gas and liquid velocity fields from measurements at several axial and radial positions.

4.4.1 Experimental Setup and Measurement Technique

Experimental facility

A sketch of the core experimental setup with the test section, as developed and investigated by Sommerfeld and Qiu [99], is presented in Figure 4.5, left view. The facility contains a variable speed blower, an electrical heater and a pressure vessel for the supply of the liquid before the test section. A cooling trap after the test section recovers the test liquid. In the vertical cylindrical chamber, gravity acts in the main flow direction, here the z -axis. Preheated air enters from an annulus gap (with an outer diameter of 64 mm and a gap height of 12 mm) into the test section with an inner diameter of 200 mm . Due to the sudden expansion at the end of the inlet tube, the air flow is forced to recirculate. A pressure atomizer for the spray is mounted into a hollow cone in the center of the inlet tube. The nozzle exit position is 5 mm above the cone edge, i.e. before the beginning of the test section, which allows for liquid break-up within the hollow cone. The first axial position of measurement is at 3 mm downstream from the expansion edge.

Radial profiles of velocity, liquid mass flux and droplet diameter are available for a total of seven axial positions flow downstream. In addition the change of the test chamber wall temperature in axial direction is recorded.

Physical properties

The physical properties for the hot air entering the test section at temperature of 373 K and the isopropyl alcohol spray, injected at temperature of 300 K are summarized in Table 4.14. Thermodynamic properties of liquid and vapor isopropyl alcohol, published in Sommerfeld and Qiu [98], and additional data from [106] are presented in 4.14 as well. The binary diffusion coefficient for isopropyl alcohol in air is obtained from the correlation 4.4 fitted to the experiments

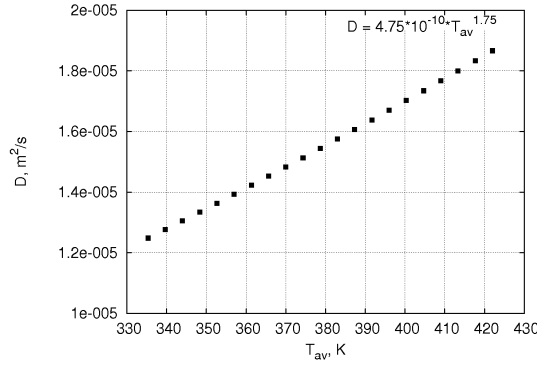


Figure 4.6: Fit of the binary diffusion coefficient D for isopropyl vapor in air according to the experimental data of Vargaftik [108].

Experimental technique

The one-point Phase-Doppler-Anemometry (PDA) experimental technique is used to measure both, the spray and carrier fluid. The phase-Doppler anemometer was mounted on a three-dimensional traversing system. The position of the receiving module, consisting of two detectors, at 30° off-axis from the main scattering direction allows for high scattering intensities even for very small droplets. The measuring volume has a radius of $200 \mu m$ and length of $12.6 mm$ (imaged length $194 \mu m$). Further parameters concerning dimensions and characteristics of the PDA system are discussed in [99]. The estimation procedure for the particle mass flux was developed by Qiu and Sommerfeld [76] to permit accurate flux and concentration measurements in conjunction with the one-point PDA technique. Sommerfeld and Qiu [97] reported from validation measurements an error concerning the mass flow of up to $\pm 10 \%$.

The gas velocity measurements by PDA are performed using glass beads as the seeding material, where only the Doppler signal from beads smaller than $3 \mu m$ is sampled. The gas velocity measurement is omitted for the spray operated case. The air-inlet area is scanned with a thermocouple to get a profile of the mean temperature for the air flow. The outer wall temperature along the test section is measured via fixed thermocouples.

4.4.2 Numerical Setup

Domain and physical properties

A sketch of the computational domain in terms of the inner annular tube diameter can be seen on the right hand side of Figure 4.5. The length of the test section was set to $15.5D$. The domain length is sufficient to minimize the influence of the outlet boundary condition on the relevant quantities used for comparison with the experiment, which was shown by computing numerical setups with different extents. The last measured axial position is at $z/D = 10$. Data from the single phase calculation are used for the assessment. For details see Section xxx ERGEBNISSE. The computational domain is discretized with 1.646 million cells, where approx. 0.5 million cells are within the core chamber region of radius $0.032 m$ and length of $0.15 m$, or

Table 4.14: Physical parameters.

Air		
Molar mass , M	28.84	$kg/kmol$
Density at 373 K, ρ	0.9329	kg/m^3
Critical temperature, T_{crit}	132.5	K
Critical pressure, P_{crit}	37.7	bar
Heat capacity at 373 K, c_p	1.012	$kJ/kg/K$
Isopropyl alcohol		
Molar mass , M	60.09	$kg/kmol$
Density (liquid) at 300 K, ρ_{liq}	780	kg/m^3
Critical temperature, T_{crit}	508.3	K
Critical pressure, P_{crit}	48.2	bar
Heat capacity (liquid), c_p	2.67	$kJ/kg/K$
Latent heat at 300 K	687	kJ/kg
Boiling temperature, T_{boil}	355.25	K
Binary diffusion coeff. at 350 K	$1.36e - 5$	m^2/s

in non-dimensional form, $D/2$ and $z/D = 3.75$. Minimum and maximum characteristic cell lengths² are respectively $2.08e - 4 m$ and $3.5e - 3 m$.

The *incompressible ideal gas law approximation* is used to compute the densities of the air and isopropyl vapor. If p_{op} is the operating pressure defined, this reads:

$$\rho_f = \frac{p_{op}}{\frac{R}{M_w} T} \quad (4.6)$$

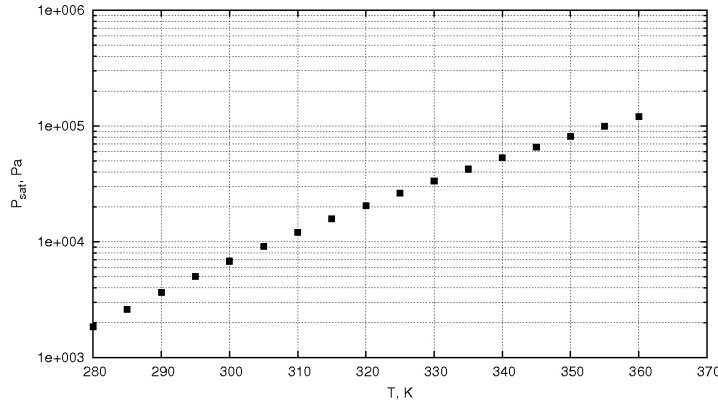
The other quantities in Equation (4.6) are the universal gas constant R , molecular weight of air M_w and the local temperature T . For more details see [2]. This approximation is widely used since it introduces a dependency of the density on the local temperature, but decouples it from the local pressure and hence, from the local velocity. It allows the usage on an inexpensive incompressible pressure-velocity coupling algorithms and is accurate if the flow does not involve strong compressibility effects, such as shocks.

The specific heat capacity of the air is set to a constant value at 373 K as given in VDI-Wärmeatlas [106]. The air viscosity, as well as the viscosity of the isopropyl vapor, are approximated with linear functions within the temperature range of 298 – 373 K. The data originate again from [106]. The specific heat capacity and the thermal conductivity of the liquid isopropyl

²The characteristic cell length is defined as $V_{cell}^{1/3}$, where V_{cell} is the volume of the computational cell.

Table 4.15: Flow conditions.

	Volume flow rate	Mass flow rate	Initial temperature
	m^3/s	kg/s	K
Single phase	0.032	0.029	373
Two-phase flow:			
Air	0.031	0.0283	373
Isopropyl alcohol	$5.8 \cdot 10^{-7}$	0.00044	307


Figure 4.7: Saturation pressure for Isopropyl alcohol as a function of the droplet temperature.

are set to the measured constant values at 300 K in accordance with [106]. The time averaged maximum droplet temperature as achieved from the LES do not exceed 305 K , which relieves the restriction assuming constant droplet properties. The saturation pressure p_{sat} varies within a relatively narrow temperature range by several order of magnitude as shown in Figure 4.7.

p_{sat} is approximated using the exponential function 4.7 as proposed by Daubert and Danner [18]. The coefficients can be found in Table 4.16.

$$p_{sat} = e^{A+B/T+C\ln T+DT^E} \quad (4.7)$$

The resulting saturation pressure is in *bar* units. The function and the coefficients hold for the

A	B	C	D	E
81.42207	-8177.1	-10.031	$3.9988e - 6$	2

Table 4.16: Coefficients of Eq. 4.7 for Isopropyl alcohol according to [18].

range between the material melting and the critical point.

Boundary and initial conditions

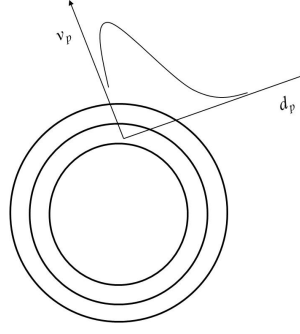


Figure 4.8: Sketch of the droplet inlet section.

For this configuration, both the continuous and dispersed phases, have different inlet positions and properties. The inlet for the air flow is defined at $z = -2.5D$, as shown in Figure 4.5. At the inlet plane, the axial velocity component is set to a constant value. The length of the annular tube is enough to ensure that the profile of the mean axial velocity at the first measurement position of $z/D = 0.075$ reproduces the experimental profile. In addition, the LAGRANGIAN Vortex Method [58] is applied to generate spatially correlated velocity fluctuations, which are superimposed with the axial velocity at the inlet. The turbulent velocity fluctuation generation is based on 4 % turbulent intensity and the hydraulic diameter of the annular tube at the inlet plane. The air is assumed to enter the domain at a constant temperature of 373 K and the isopropyl-vapor mass fraction is set to 0.

Since the spray nozzle is not included in the simulation and the inlet spray properties are adopted from the measurements at the first axial position at $z/D = 0.075$, the spray outlet from the cone is replaced in the simulation by a wall. As already mentioned, the inlet for the dispersed phase is artificially defined at $z/D = 0.075$. The droplet velocity is defined using the detailed database from the experiment in terms of diameter-velocity correlations. Furthermore, the droplet diameter distributions, measured at ten radial positions for the same plane, are used for initial distributions of the two-phase flow simulation. A sketch of the particle inlet is depicted in Figure 4.8. The droplet temperature at the inlet is set to a constant value of 307 K.

At the wall boundaries, a no slip boundary condition is applied for the air momentum equation, and zero gradient condition, i.e. adiabatic wall, concerning the temperature field. Droplets that reach the walls are marked as escaped and deleted from the simulation. Due to the high air temperature and the relatively small droplet diameters it is expected that a droplet-wall collision will be a rare event. Therefore, the application of a more sophisticated boundary condition that accounts for effects such as droplet splashing, would be redundant.

At the outlet boundary, a pressure outlet condition accounts for zero gauge pressure and zero gradient condition for air velocity and temperature. Particles which cross the outlet boundary are marked as escaped and excluded from the tracing algorithm.

The numerical procedure

In addition to the general numerical setup, as described in Section 4.1.2, the simulation includes the solution of transport equations for energy (Equation (2.9)), and for the isopropyl-vapor mass fraction, see Equation (2.8). The convective terms of both equations are discretized with the second order upwind scheme.

The numerical model assumes uniform temperature distribution within a droplet. The model applied in the LAGRANGIAN frame resolves only mass and energy transfer at the particle surface. From Equation (2.78) it is obvious that the mass transfer continues until the droplet's volatile mass fraction is completely consumed. In this case the volatile fraction is 100% and assumes calculation of vapor transfer until the droplet diameter becomes zero. In numerical calculations the common practice is to set an cut-off diameter of $d \ll 10^{-6} \text{ m}$ to approximate a zero diameter. However, experimental measurements are restricted to a cut-off diameter of $d \approx 3 \cdot 10^{-6} \text{ m}$. The cut-off diameter of the smallest tracked droplets is set to 10^{-8} m . In order to compare the influence of the cut-off diameter on droplet characteristics, such as diameter, mean or Sauter mean, and velocity, the particle data are exported every 25^{th} timestep and analyzed via an external postprocessing tool developed for this purpose. The particle data set contains coordinates of the particle's position, velocity components, temperature and diameter. Further details of the evaporation process are in Sections 2.2.3.3 and 2.2.3.4.

Table 4.17: Simulation parameters.

Case	Total time	Sampled time	Particle number $\cdot 10^6$	Time step, s
single phase	$18 t_R$	$10 t_R$	—	$5e - 6$
two-phase	$8 t_R$	$3 t_R$	3.74	$5e - 6$

Configurations

One single phase and one two-phase flow large-eddy simulation are performed for the current configuration. Parameters concerning the simulations are summarized in Table 4.17. The residence time t_R is defined as the ratio of the chamber length of 0.62 m and the mean averaged maximal air velocity at the chamber inlet of 18 m/s . The carrier phase velocity from the

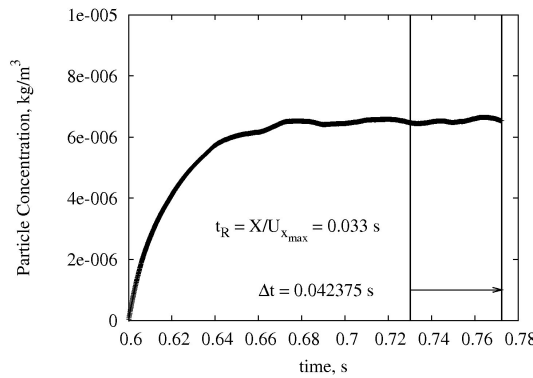


Figure 4.9: Particle mass concentration as a function of the time.

calculation of the single and the two-phase flow LES showed very similar profiles despite the significantly shorter sampling period for the two-phase flow LES. For this reason, the sampling period of $3 t_R$ for the two-phase LES is found to be sufficient to achieve converged statistical

properties for the carrier fluid. The results are discussed in detail in Section 6.3.

In Figure 4.9 the total droplet mass concentration is plotted as a function of the physical time. The latter is normalized with the flow residence time, as defined above. The droplet concentration reaches a statistically steady state after approximately $2.5 t_R$. For the last three flow residence times, t_R , statistics are collected for the dispersed phase as well. The time for the statistical sampling is found to be sufficient.

5 Code Validation

This chapter constitutes the basic prediction ability of the CFD code for single and two-phase flows when employing LES. Computation results from the simulation of a particle-laden plane channel flow are presented for validation purposes. In addition, some aspects of two-phase flow LES are discussed in the context of a particle-laden free jet flow. The LES results are compared with reference DNS and experimental data, and are related to the configurations presented in Section 4.1, 4.2 and 4.3.

Several aspects of the simulation need assessment. These lead to the following topic sub-division considered below:

- Assessment of the single phase flow LES
 - Validation of the basic solver
 - Effect of the pressure-velocity coupling algorithm
 - Unsteady inflow boundary condition
- Assessment of the two-phase flow LES
 - Validation of the particle tracking in conjunction with LES
 - Effect of the pressure-velocity coupling algorithm in two-way coupling
 - Numerical versus real number of particles in the LES context

Before proceeding, some of the characteristic features of the CFD tool used in this work will be listed.

FLUENT is a general purpose CFD simulation environment, commercially distributed by ANSYS Inc., Southpointe. The underlying flow simulation algorithm is based on the Finite Volume Method, formulated for arbitrary unstructured non-orthogonal grids. The core solver is efficiently parallelized based on the domain decomposition concept utilizing a variety of communication libraries, like MPI® or PVM®. Next to advanced dynamic mesh capabilities, heavily used for the simulation of internal combustion engines, involving mesh motion, dynamic remeshing and others, modules for the simulation of turbulence, multiphase flows, compressible flows, reacting flows, radiating heat transfer, solidification and melting and others are included. The FLUENT solver includes two fundamentally different flow solution algorithms for solving the mass and momentum conservation equations. The difference is in the choice of an independent variable for the mass continuity equation, density on the one hand, pressure on the other hand. Both allow for the assembly of a coupled matrix consisting of the linearized mass and momentum equations. In the case of the density based solver, since its main design target is the simulation of high speed compressible external aerodynamic flows, the energy equation is also included in this matrix, delivering the highest possible degree of implicit equation coupling. In the pressure based solver, in addition to that, segregated approaches like SIMPLE, SIMPLEC, PISO or fractional step methods are implemented allowing for faster time marching in transient simulations.

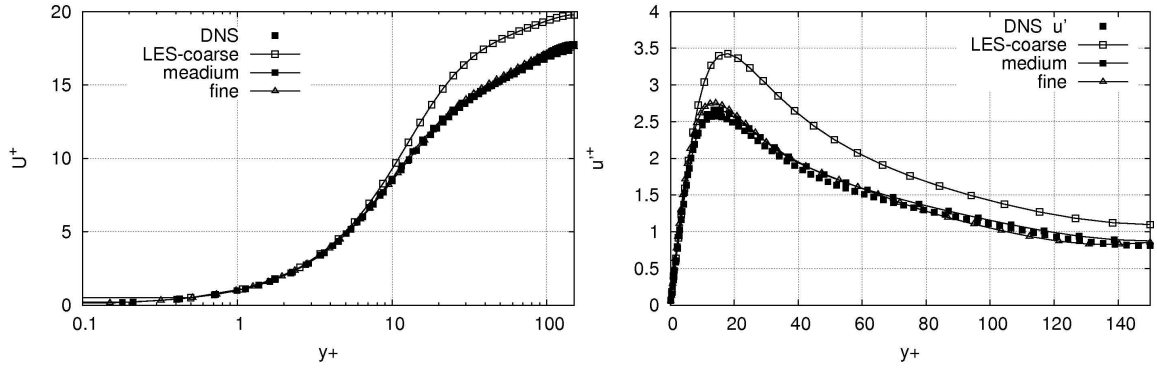


Figure 5.1: Channel Flow, $Re_\tau = 150$. Profiles in wall-normal direction of the streamwise mean velocity and the streamwise velocity fluctuations. Comparison between the LES and the DNS of Picciotto et al. [70].

5.1 Assessment of the single phase flow LES

5.1.1 Validation of the basic numerical setup

The majority of the simulations presented in this work, share the same basic numerical setup. A second order implicit time-advancement scheme is applied to the NAVIER-STOKES equations using the finite-volume discretization. The solution of the system of equations, derived in Section 3.1, relies on a segregated pressure based solver. For the type of pressure-velocity coupling, it was found that the Fractional Step Method (FSM) for transient problems preserves the required second order accuracy of the time advancement scheme. Secondly, the method abstains by definition from the global iterations between the continuity and the momentum equation within a single time step. Consequently, the solution can accelerate up to several times compared to commonly used iterative time advancement methods, such as SIMPLE, SIMPLEC or PISO. Due to the equation decoupling the method is more sensitive to rapid change of the solution variables and to density variation.

To investigate the reliability of the FSM for LES, results of a standard test case, a plane channel flow, are provided below. A second order central differential scheme is used for the spatial discretization.

The computational results from the LES are compared to the DNS database for the low REYNOLDS number channel flow. The flow has a frictional REYNOLDS number $Re_\tau = 150$, based on the friction velocity u_τ and the channel half height. A comprehensive compilation of the numerical setup for both the present Large-Eddy and the reference Direct Numerical Simulations, as proposed by Picciotto et al. [70], is in Section 4.1. The subgrid stress tensor τ_{sgs} is approximated by the Smagorinsky model [93] together with the dynamic procedure proposed by Lilly [51] for the estimation of the model constant.

Figure 5.1 shows a plot of the mean and fluctuating velocity components of the channel flow. The x-axis is the normalized distance from the wall $y^+ = y u_\tau / \nu$. The mean and rms velocity components are normalized with the friction velocity. The coarse grid has 20 % less grid cells in every direction compared to the medium grid. The fine grid on its side has 20 % more grid cells per spatial direction than the medium grid. Further details of the discretisation are listed in Table 4.3.

From the one-point statistics in Figure 5.1, it becomes obvious that the discretization error de-

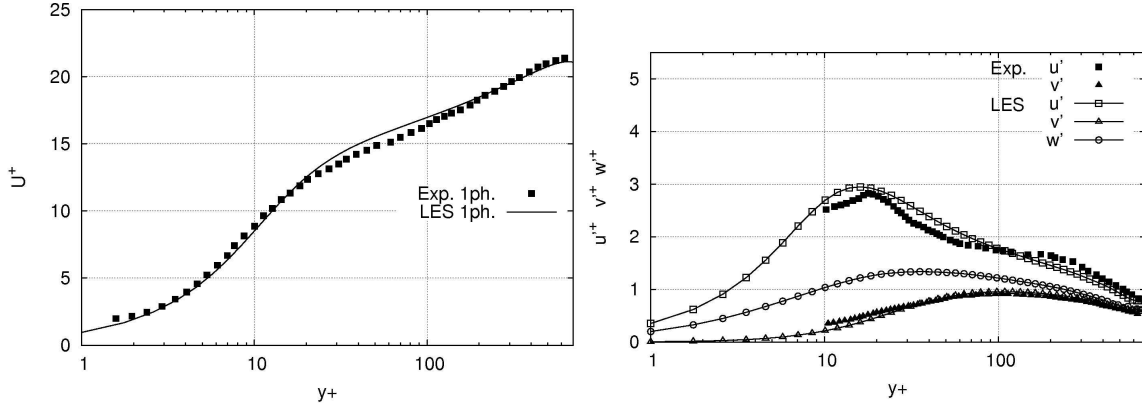


Figure 5.2: Channel Flow, $Re_\tau = 644$. Profiles in wall-normal direction of the mean and fluctuating velocities. Comparison between the LES and the experiment of Kulick et al. [48].

creases significantly with an increasing number of grid points. This behavior can be related to the fact that the near wall region for $y^+ < 10$ is resolved with more than 10 points in the case of the two finer grids. The conclusion is in accordance with the common resolution requirements for boundary layers in wall bounded flows quoted in [86, 34].

Results from the wall resolved LES on a high REYNOLDS number channel flow (Section 4.2) are presented as well. The simulation addresses a flow with $Re_\tau = 644$ based on the friction velocity and the channel half height. This corresponds to a bulk REYNOLDS number of 13800 based on the mean centerline velocity. Figure 5.2 presents the simulation results together with the data from the reference experiment by Kulick et al. [48]. The comparison confirms the very good quality of the simulation presented here. Considering the total estimated error from the experiment given by Kulick et al. [48] (3 % for the mean velocity and 5 % for the velocity fluctuations) the simulation qualifies as reliable.

5.1.2 Influence of the pressure-velocity coupling

The FSM currently available has been extensively validated on numerous standard transient laminar flows (Kim and Makarov [43]). These authors present a comparison to a DNS of a channel flow with $Re_\tau = 180$ as proposed by Moser et al. [63], in conjunction with the LES method and turbulent flows. To inquire about the effect of the pressure-velocity coupling on high REYNOLDS numbers flows, the results from computations employing the non-iterative Fractional Step [43] and the standard iterative SIMPLE method have been conducted. In terms of velocity statistics, the results from a single phase flow LES on the free jet flow with $Re_{bulk} = 13000$ (presented in Section 4.3), are compared to the experimental measurements proposed by Hardalupas et al. [37]. The LES data discussed below addresses the jet flow configurations FS- U_{const} and SIMPLE- U_{const} performed on the coarser grid with ≈ 1.3 million computational cells. Their setup is outlined in Table 4.12.

In Figure 5.3 radial profiles of the axial mean jet velocity at three axial positions are presented. Hardalupas et al. [37] provide an error estimation of 1 % for the mean velocity and 3 % for the rms part of the velocity. The total error of both the LES simulations remains very similar, despite the fact that the error magnitude for this particular configuration is larger than the channel flows discussed above. With the aid of a subsequent LES with a finer grid resolution and

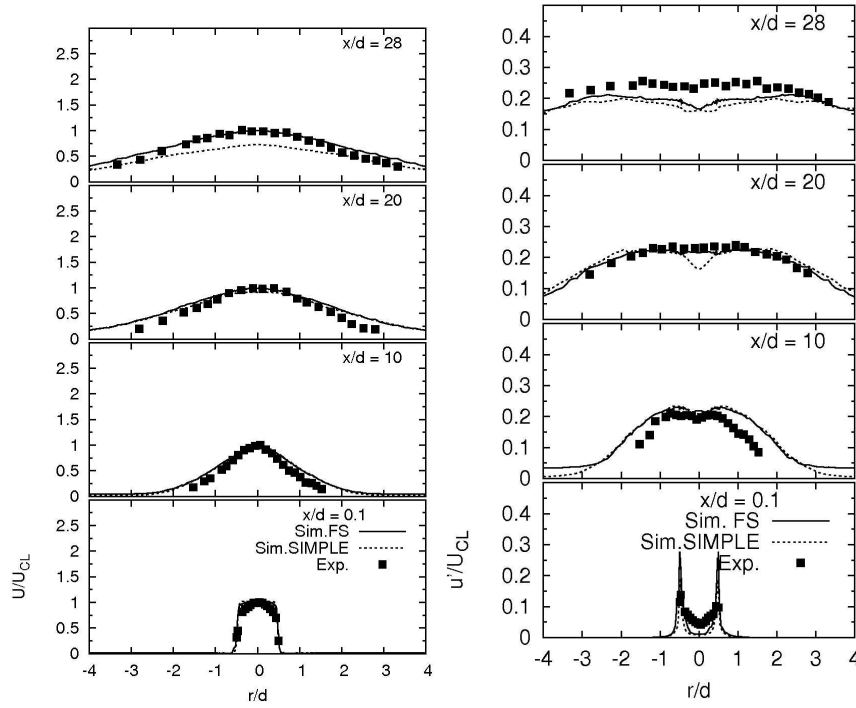


Figure 5.3: Free jet flow, $Re_{bulk} = 13000$. Radial profiles of the axial mean and rms velocity. Comparison between FS- U_{const} , SIMPLE- U_{const} and experimental data proposed by Hardalupas et al. [37].

with the FSM, an improvement in the overall velocity field prediction is made. For turbulent flows with moderate REYNOLDS numbers, the Fractional Step Method provides reliable results for a reasonable computational effort in terms of time units. Beyond that, comparison of the computational time taken by both simulations reveals a speedup of ≈ 7 when using the FSM. The calculations are performed on a 64 bit AMD architecture using domain decomposition parallelization on 32 CPU's.

5.1.3 The unsteady inflow boundary condition

The LAGRANGIAN Vortex method used in the this work to generate unsteady velocity fluctuations at the inlet boundary has been comprehensively validated and presented in the work of Mathey and Cokljat [58]. Details of the mathematical and physical background are outlined in Section 3.1.3. The following test is applied to validate the inlet conditions for the full-scale test case of a particle-laden jet flow, and is discussed later in this work.

Turbulent flow in a pipe with $Re_{bulk} = 13000$ is simulated as a prior step to the simulation of a free jet flow. Computation of the latter includes modeling a segment of the flow supplying pipe to represent the inlet flow behavior more accurately.

Two sets of inflow conditions are investigated for this purpose. The first approximation for the inlet is a block (top-hat) profile for the mean axial velocity, with a magnitude of 18 m/s and a turbulent intensity of 4 %. The intensity magnitude setting choice was based on the measured axial velocity fluctuation on the main axis of the pipe. Isotropic turbulence is also assumed. The second setup considers profiles corresponding to a fully developed pipe flow for the mean

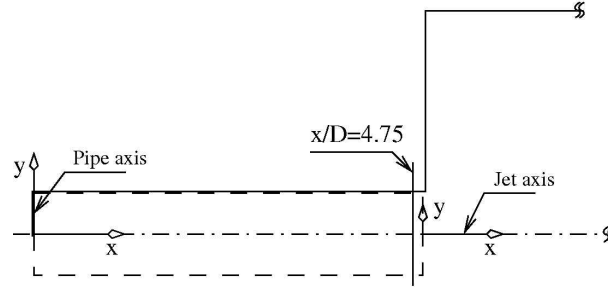


Figure 5.4: Pipe flow, $Re_{bulk} = 13000$. Sketch of the computational domain, superimposed with the domain of the full scale test (dashed line). Axial position of the LES and the corresponding experimental profiles.

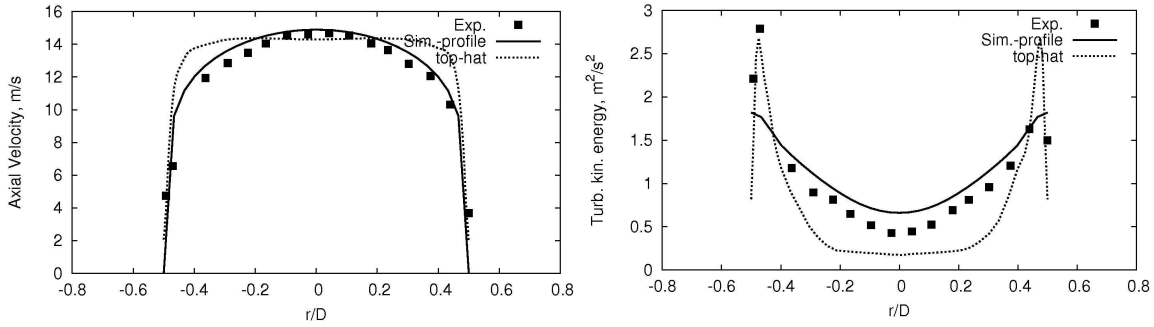


Figure 5.5: Pipe flow, $Re_{bulk} = 13000$. Radial profiles of the axial mean velocity and the corresponding fluctuations. LES profiles at $x/D = 4.75$. Results from the setup with top-hat velocity profile and turbulent intensity at the inlet and from the setup with profiles corresponding to a fully developed pipe flow for U_{ax} , k and ϵ . Experimental data from [37] at $x/D = 0.1$.

axial velocity, the turbulent kinetic energy and the dissipation rate for the latter. The profiles are computed from a preliminary steady state $k - \epsilon$ simulation on periodic pipe flow at the same bulk REYNOLDS number.

The computational domain has a length of $5D$, where $D = 0.015\text{ m}$ is the pipe diameter. $2 \cdot 10^4$ hexahedron control volumes are used for the domain discretization. The near wall region is resolved with six prism layers. However, the intention is not to perform a wall-resolved LES. Moreover, the discretization of the pipe is similar to those used for other configurations in the literature, where part of the supplying rig is included in the computational domain ([66]). Both setups of inlet velocity conditions are used, in conjunction with the Vortex Method, for which 200 vortices are initialized. A no-slip condition is applied at the wall and a pressure outlet at the outflow boundary. The velocity profiles from the simulations correspond to axial position $z = 4.75D$. The mean axial velocity and the corresponding fluctuations are compared to experimental results obtained at the first axial position of the jet flow. The sketch of the computational domain in Figure 5.4 shows the positions of the profiles from the LES and the reference experiment. Within the coordinate system used, the position of the experimental data corresponds to $z = 5.1D$. The velocity plots can be seen in Figure 5.5. The velocity components are normalized with the maximal velocity at the centerline.

As expected, the second setup matches the experimental profiles more accurately due to the application of realistic profiles at the inlet. Nevertheless, an important observation of the first setup (with a top-hat profile at the inlet) is that turbulence develops even within a short distance.

Obviously, the length of the pipe is not sufficient to achieve a fully developed turbulent flow until its end. This is important for configurations where explicit profiles for diverse flow quantities are not available and the boundary conditions need to be approximated from global quantities, such as mass flow rate or pressure. In addition, better domain resolution has a positive effect on the development of the profiles, as shown in the studies of Mathey and Cokljat [58] and Olbricht [66].

5.2 Assessment of the two-phase flow LES

5.2.1 Validation of particle tracking used with LES

The low REYNOLDS number channel flow configuration, as presented in Section 4.1, is used to validate the particle tracking technique. Three different particle sizes were investigated in the reference work of Picciotto et al. [70], employing Direct Numerical Simulation together with LAGRANGIAN particle tracking, under consideration of one-way coupling.

The validation in this thesis is related to the basic setup of the Large-Eddy Simulations in conjunction with the LAGRANGIAN particle tracking: The continuous phase motion is resolved due to Large-Eddy simulation employing a second order implicit time advancement scheme together with the non-iterative Fractional Step method. Second order, central differencing scheme is applied for spatial discretization. The integration of the particle equation of motion utilizes an *automated tracking scheme selection*, which combines the low order implicit Euler with the high order trapezoidal schemes. The error from the integration of the particle equation is assessed for every time step and the optimal scheme is used. A description of the accuracy control procedure can be found in Section 3.2.1.

Furthermore, one-way coupling is assumed for the current configuration. All additional parameters related to these simulations are summarized in Section 4.1.2.

The streamwise mean and rms velocities of the dispersed phase are presented in Figure 5.6. The particle velocity profiles are plotted in a wall-normal direction. The quantities of both axes are normalized using the fluid friction velocity, the channel half height and the fluid kinematic viscosity. The particle classes are denoted in terms of their STOKES number, as defined through the STOKES particle response time τ_p and the KOLMOGOROV time scale. There is a very good approximation of the mean particle velocity. In contrast to this, the fluctuating streamwise component is slightly overestimated by the LES.

Another observed behavior, also typical for this configuration, is the preferential accumulation of particles in wall-bounded flows within the near wall region. The results from the LES match this behavior very well for all three particle classes. An extensive investigation of this behavior is one of the main topics of this research and the prediction ability of LES will be discussed in Section 6.1.

5.2.2 Influence of the pressure-velocity coupling on LES using two-way coupling

From the numerical point of view, two-way coupling is more difficult to handle in simulations. The source term that considers momentum, mass or heat transfer from the dispersed toward the continuum phase has an inevitable impact on the convergence behavior of the system of

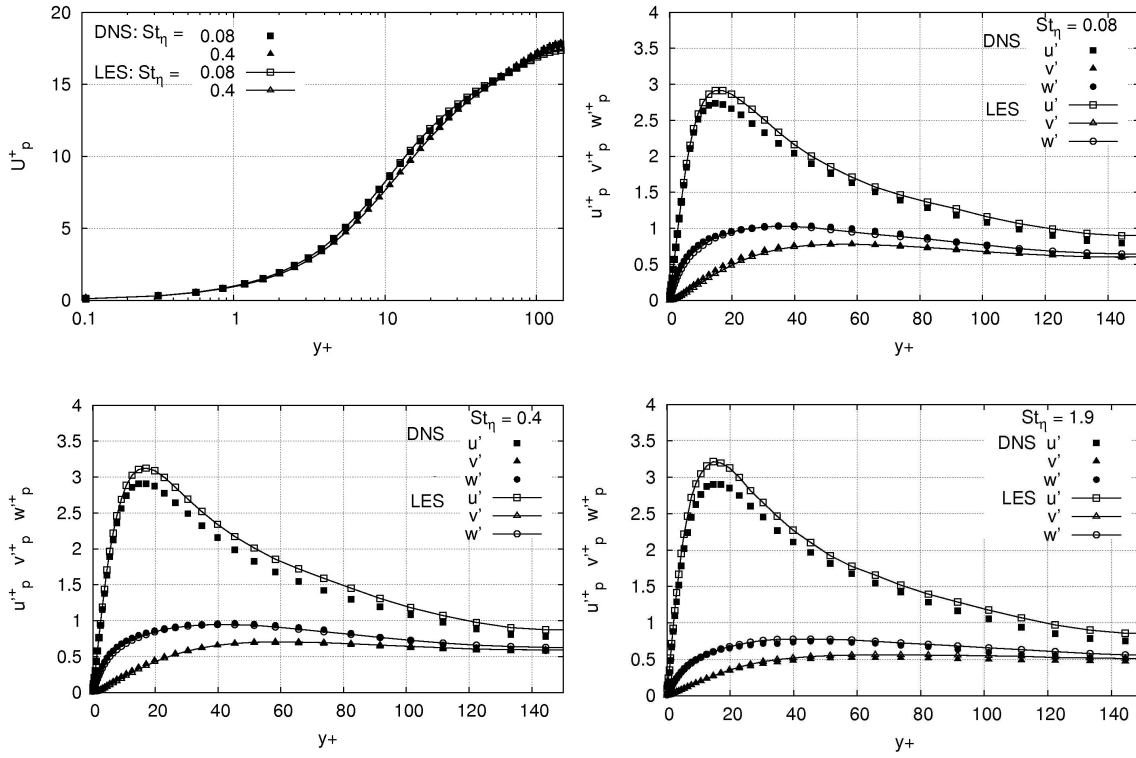


Figure 5.6: Channel Flow, $Re_\tau = 150$. Profiles in wall-normal direction of the mean and rms particle velocity. DNS data from [70].

partial differential equations. For this purpose, the fluid statistical properties are captured by employing again both the non-iterative Fractional Step Method and the standard iterative SIMPLE method. The comparison is performed based on simulations of a particle-laden jet flow with 86 % particle mass loading. The setup for the two-phase LES is related to the configurations *d80φ86-FS* and *d80φ86-SIMPLE*, as denoted in Table 4.13 of Section 4.3.2.

The results from the computations using the alternative pressure-velocity couplings are shown in Figure 5.7 in terms of the axial fluid velocity. Radial and axial profiles of the fluid velocity develop in very similar ways. The momentum source term that arises from the combination of high particle mass loading and fairly heavy particles is accomplished well by the FS method. This is demonstrated by a comparison with the experiment of Hardalupas et al. [37]. The flow computed with the SIMPLE method seems to develop unphysical behavior in the surrounding domain. For the SIMPLE-based LES computation is performed with 20 iterations per time step. The residuals at the end of the time step are in the order of 10^{-5} for the continuity and 10^{-8} for the momentum equations.

The plots corresponding to the axial fluctuating velocity confirm the impression gained from the mean velocity results. Despite the fact that the overall magnitude of the velocity fluctuation within the jet is the same for both simulations, the significant discrepancy between the SIMPLE-based LES and the experiment lead to the observation, that 20 iterations per time step are not sufficient. On the other hand, the results from the FSM-based LES agree very well with the experimental findings.

The promising results achieved with the FSM for different flow conditions are convincing

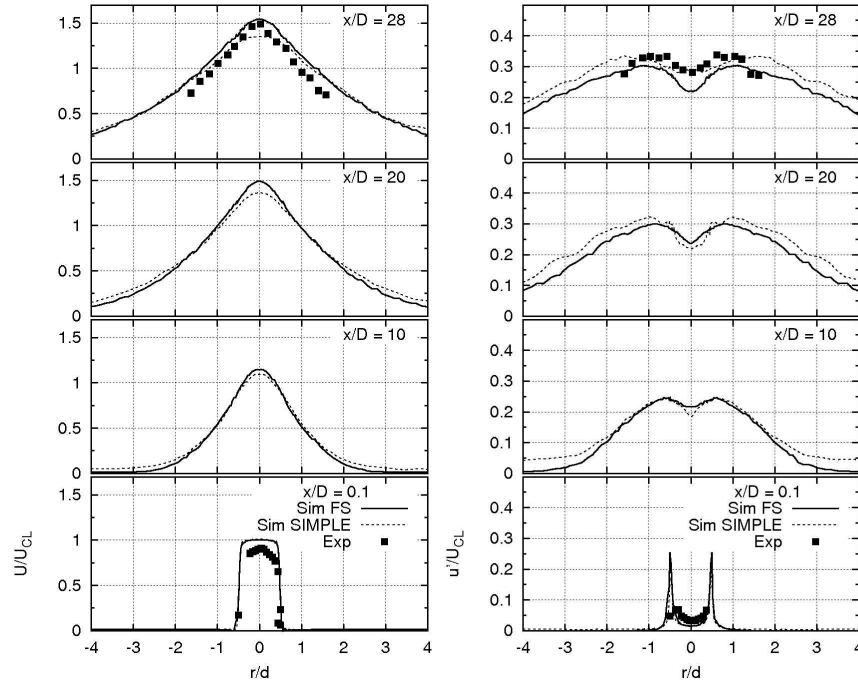


Figure 5.7: Free jet flow, $Re_{bulk} = 13000$. Radial profiles of the fluid axial mean velocity at 80 % particle mass loading. Comparison between a non-iterative FSM-based LES, an iterative SIMPLE-based LES and experimental data from [37].

enough to use the method for the main simulations in the present in this thesis.

5.2.3 Numerical versus real number of particles in the context of LES

The representation of the coupling term, considering the influence of the dispersed phase on the carrier fluid, reveals additional numerical issues. Since the LAGRANGIAN approach deals with mass points the resulting source term toward the continuum phase is also point-wise. Each numerical particle represents a number of real particles. This number can be less than, equal to or greater than one. The latter provides an artificial phase interaction, which leads in some cases to unphysical representation of the two-phase flow behavior. To gain more reliable simulation results it is important that the source term per time step and computational cell is derived from a sufficient number of particles. In the context of LES, where the computational cells are much smaller than the integral length scale, the issue is in satisfying the upper condition. One possible solution is to involve more numerical than real particles. These represent only a small fraction of a real particle to retain the real particle mass flow rate.

The substitution of the real number of particles by an artificially higher number is followed by two intuitive questions. First, what is the effect on the particles' properties, such as velocity, concentration or dispersion? Second, what is the effect of spatial splitting of the source term on the carrier fluid, i.e. does the splitting compensate for the far field effect of the source term, as observed in real flows (according to Burton and Eaton [12])? Since the second question is related to the reliability of the two-phase LES and is one of the main topics investigated here,

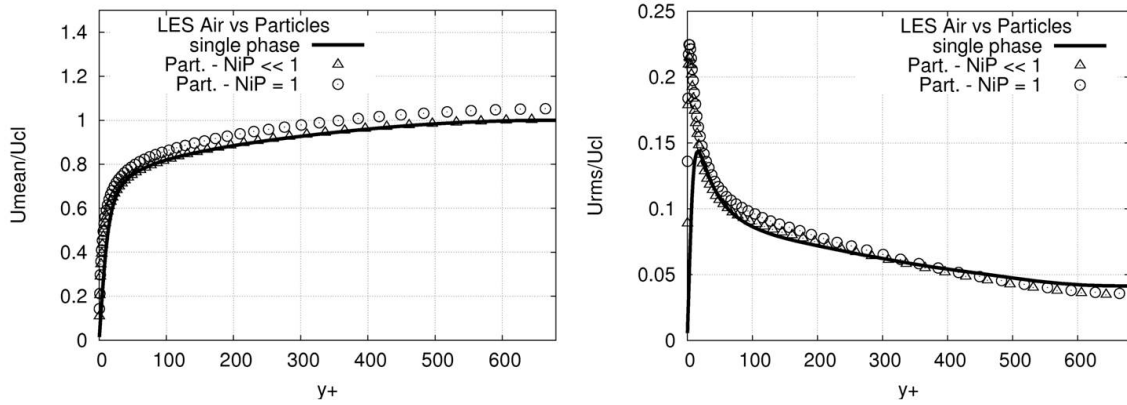


Figure 5.8: Channel Flow, $Re_\tau = 644$. Profiles in wall-normal direction of the streamwise mean and rms particle velocity of the $70 \mu m$ particles at 20 % mass loading. Real particles number in parcel is $NiP = 0.09$ for case $d70\phi20$ and $NiP = 1$ for case $d70\phi20 - nip1$. Experimental data from [48].

a more comprehensive discussion is presented in Section 6.2. This section simply ensures that the particle's behavior, in terms of velocity and concentration statistics, is not damaged by the particle splitting. This is demonstrated with the aid of results from two-way coupled two-phase LES of the channel flow configuration at $Re_{CL} = 13800$, as described in Section 4.2.

The results presented here in Figure 5.8 correspond to the configurations $d70\phi20$ and $d70\phi20 - nip1$, as denoted in Table 4.9. The different number of particles tracked in this case does not affect the mean and the rms of the streamwise particle velocity. The same behavior is also valid for the concentration of the dispersed phase, except for the near wall region at $y^+ < 1$.

Consequently, the number of parcels does not affect the statistical quantities of the particle properties in the dispersed phase. At this stage, it can be concluded that the only limiting parameter for using more numerical particles than real ones is available memory resources.

6 Results and Discussion

This section is divided into three main parts. The first two parts are devoted to bidirectional momentum transfer in two-phase flows in the context of isothermal and incompressible turbulent two-phase flows. In other words, the particle motion affected by turbulence (6.1) and the turbulence modification due to the presence of particles (6.2) are investigated. The results from Large-Eddy simulations on the first three configurations, as outlined in Chapter 4 (Reference Configurations), are studied and discussed. The last part of this section provides an analysis of the prediction capability of the two-phase LES when applied to a more complex application, such as an evaporating spray (6.3).

The four basic configurations involved in the following discussion are referred to as *low REYNOLDS number channel flow*, presented in Section 4.1, *high REYNOLDS number channel flow* (Section 4.2), *jet flow* (Section 4.3) and *evaporating spray flow* (Section 4.4).

6.1 Influence of Turbulence on Particle Motion

Particle distribution due to turbulent structures in the carrier fluid has several physical phenomena. Turbulence augments particle dispersion. Another effect is the preferential accumulation of particles in low vorticity or low turbulence regions, which depends on the ratio of the characteristic scales of the fluid and the dispersed phase. Another well-known phenomenon is the accumulation of particles in the near wall region.

To quantify the prediction of these physical phenomena using the LES method, the discussion is based largely on the channel flow configurations (low REYNOLDS number and high REYNOLDS number channel flow). Since two of the particle classes used in both configurations have similar time constants, it is useful to compare the overlapping findings on particle behavior in flows having different REYNOLDS numbers. In addition, the study of the particle motion in the jet flow shows phase interaction mechanisms free from wall influence. In the following, several perspectives on the available results are presented.

- The particle velocity field is investigated and compared with reference data.
- Instantaneous particle data are applied to demonstrate typical concentration patterns for particles with different time constants. With the aid of particle number distributions, the amount of preferential accumulation is quantified.
- Particle accumulation in the near wall region is analyzed for concentration profiles in the wall-normal direction.

6.1.1 Particle Velocity Statistics

Particle dispersion due to turbulence implies an effect on the particle velocity field. According to the earlier experimental works discussed in Section 2.2.3.5, the turbulent particle dispersion in dilute two-phase flows, quantified by the change of the drag coefficient C_D , seems to correlate with the relative turbulent intensity I_{rel} , Equation (2.79), and with the ratio of the fluid integral length scale to the particle diameter. Both relations amount to the same conclusion - the smaller the particle, the more perceptible the effect of turbulent dispersion on it. Using I_{rel} to parameterize the phenomenon, this conclusion is also true for particles with a small time scale τ_p , which also directly includes the particle density. It can be further expected that lighter particles will disperse more intensive than heavy particles.

Before proceeding with the discussion, the procedure for calculating the statistical quantities of the particles is described below. For every sampling step, the ensemble average for the desired quantity is estimated per cell volume from all particles, crossing the particular volume within the defined sampling step. The length of the sampling step is defined by the fluid time step. Thus, the averaging procedure accounts for particles crossing more than one fluid cell, i.e. if a particle for the time of one fluid time step crosses two fluid cells, all particle properties are accumulated for both fluid cells and weighted by the corresponding residence time of the particle per fluid cell. The averages are accumulated for the duration of the sampling period and a time averaging is applied to obtain the statistical moments of the particle properties. Depending on the configuration, a final averaging is applied in a periodic or axis-symmetric direction.

Comparing particle properties to results from a DNS (low REYNOLDS number channel flow) is beneficial in several ways. First, the forces acting on the dispersed phase are well known. In the DNS, only the drag force is considered. Secondly, the interaction between the phases is governed by one-way coupling. The simulations discussed are performed on the *medium* grid (Table 4.3). Particle velocity data (mean and fluctuations) from the DNS [70], together with those from the LES are plotted in Figure 6.1. The three particle classes with different STOKES numbers, based on the KOLMOGOROV flow scale $St_\eta = 0.08, 0.4, 1.9$, are compared. The velocity profiles are in a wall-normal direction and the coordinate is normalized in the conventional way using wall units. The same normalization technique is followed for the velocity mean and fluctuation components. Quantities corresponding to the dispersed phase are denoted by the index p . The streamwise, wall-normal and spanwise velocities are denoted by u , v and w , respectively. It is evident from the plots that the particle mean velocity is not affected by the STOKES number. Considering the fluctuating velocity components, the main observation is that LES tends slightly to overestimate the streamwise components compared to DNS. In contrast, the underestimation of the spanwise and wall-normal components is almost negligible. It is important to note here, that the fluid velocity computed on the same grid (Figure 5.1) has very similar behavior in its fluctuating velocity components in both the LES and DNS. Considering the very low STOKES number, the intuitive conclusion is that the fluid significantly controls the particle's motion appears intuitively. Confirmation of this can be found in the LES results presented by Kuerten and Vreman [45]. The authors consider a very similar setup of a channel flow at $Re_\tau = 180$ and particles with $St^+ = 5.4$. They report a deviation of the particle fluctuating velocity in wall-normal direction of up to 25 % compared to the DNS. The fluid velocity in the same simulation deviates in a very similar way from the DNS velocity field as the dispersed phase does.

The most significant difference between the LES here and the one in Kuerten and Vreman [45]

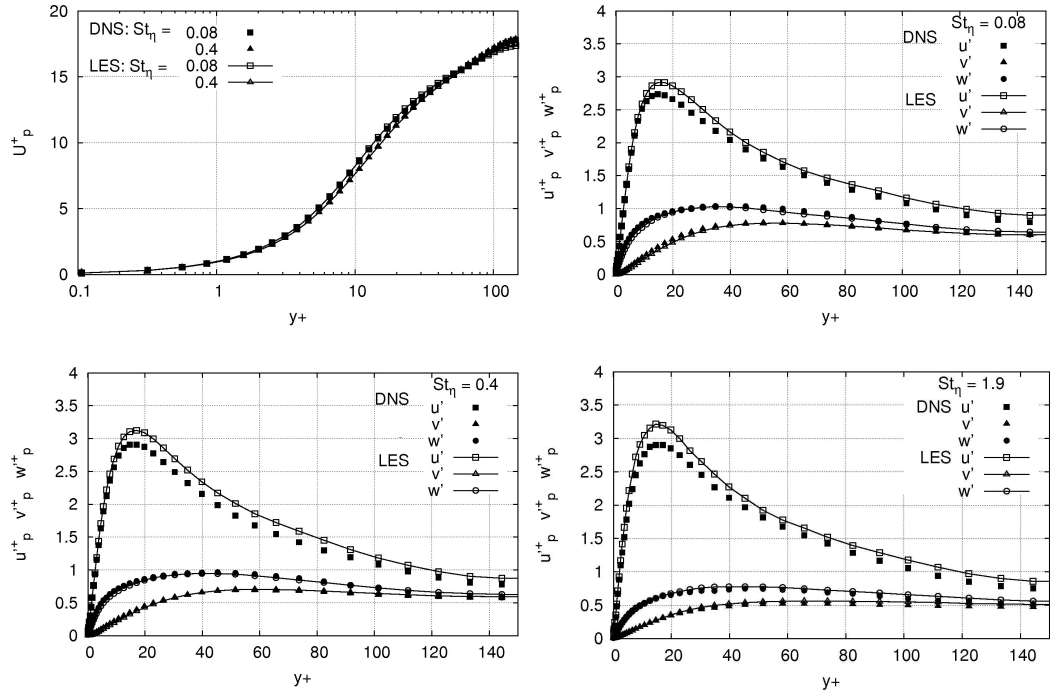


Figure 6.1: Channel flow $Re_\tau = 150$: Stream-wise particle mean velocity (left column) and particle fluctuating velocity components (right column) for STOKES number $St_\eta = 0.08, 0.4, 1.9$ in wall-normal direction. DNS data from [70].

is the domain resolution. The estimated integral length scale for the setup here is $l^+ = 65$ along the center line. The resolution used here is in a streamwise and spanwise direction $\Delta x^+ = 13$ and $\Delta z^+ = 6.5$ respectively. The corresponding resolution for the channel flow LES in [45] is $\Delta x^+ = 71, \Delta z^+ = 17$, where the integral length scale is expected to be only marginally larger. Therefore, the resolution of the large scales is essential for accurate prediction of the particle velocity, when the particle time constant is comparable to the KOLMOGOROV time scale. According to the classification proposed by Young and Leeming [116], which presents the relation between St_η and the particle deposition velocity in turbulent flows, the investigated particles belong to the *inertia-moderated* regime.

A closer examination of the streamwise particle fluctuations u_p' shows that the particles always lead the air flow. This is also true in the case of the smallest particles ($St_\eta = 0.08$) and is supported by the DNS data in Picciotto et al. [70] and Marchioli et al. [56]. With increasing particle time constant, the discrepancy becomes larger.

In the following, the particle behavior from the high REYNOLDS number channel flow simulation is presented and discussed. Particular properties of this flow will be emphasized to highlight several parameters which are of general interest here. The integral scale for the high REYNOLDS number channel flow is $l^+ = 793$ along the centerline of the channel. The corresponding maximum resolution in the streamwise direction is $\Delta x^+ = 31$ and $\Delta z^+ = 15$ in the spanwise direction. The separation of the time scales was estimated as $t_0/\tau_\eta = 23$, which is approximately a factor of four higher than in the low REYNOLDS number flow. The complete characteristics of the flow and the computational grid are summarized in Table 4.5 and 4.7. This study includes results from computation of the flow with 2 % mass loading. The particle

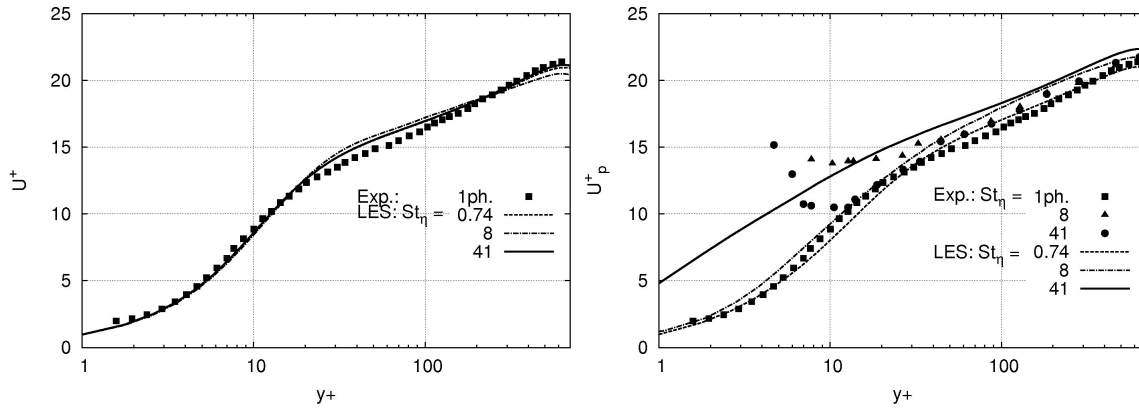


Figure 6.2: Channel flow $Re_\tau = 644$: Air (left) and particle (right) streamwise mean velocities for the flows with 2 % mass loading. The different particle classes in the flow are $28\ \mu\text{m}$ Lycopodium ($St_\eta = 0.74$), $50\ \mu\text{m}$ glass ($St_\eta = 8$) and $70\ \mu\text{m}$ copper ($St_\eta = 41$). y^+ is the wall-normal coordinate. Experimental data are taken from Kulick et al. [48].

types considered are $28\ \mu\text{m}$ Lycopodium, $50\ \mu\text{m}$ glass particles and $70\ \mu\text{m}$ copper particles. The smallest particle class has a STOKES number based on the KOLMOGOROV time scale of 0.74, which is comparable with two of the particle time constants from the low REYNOLDS number configuration. The other particles from the current configuration (the glass and copper particles) exhibit significantly larger time scales, $St_\eta = 8$ and $St_\eta = 41$, respectively. The volume fraction for the glass particles averages 10^{-5} and for the copper particles $3 \cdot 10^{-6}$, hence, the feedback from the particles to the fluid can be neglected and the focus remains on one-way coupling mechanisms. To assess this effect for a mass loading of 2 %, simulations with and without two-way coupling are performed and show negligible deviations. Nevertheless, the results presented below are from Large-Eddy Simulations considering two-way coupling. Further information concerning the dispersed phase properties can be found in Table 4.6.

Figure 6.2 presents the mean velocity in streamwise direction of both phases. The quantities are again normalized using wall units. Quantities corresponding to the dispersed phase are denoted by the index p . The streamwise, wall-normal and spanwise velocities are denoted by u , v and w , respectively. The plot demonstrates that the mean velocity field of the particle-laden fluid is not significantly affected by the particles, which is also due to the fairly low mass loading. On the other hand, the mean velocity profiles of the dispersed phase show extremely different behavior. Since velocity measurements for the Lycopodium particles are not available, they are compared to the velocity field of the single phase flow. Two aspects of the particle behavior require comment. First, within the inner channel region according to the experiment, the different particle types denote very similar behavior, which is not supported by the simulation. The velocity of the copper and glass particles is overestimated. The second and more significant discrepancy is within the near wall region for $y^+ < 30$. The characteristic plateau observed for the two heavier particle classes and the subsequent velocity increase very close to the wall is totally mismatched by the simulations.

A theory concerning this particular behavior, especially in the case of the copper particles, is given by the authors in [48]. They ascribe the near-wall velocity increase to particles coming from the middle of the channel with much higher velocity. Fast particles from the inner part of the channel hit the wall and, due to elastic rebound, most of their streamwise momentum

is retained. A more practical insight into the processes in this region is provided by the work of Benson and Eaton [9]. The authors report a significant influence of the wall roughness on the particle velocity characteristics. The experimental rig used in [9] is the same as in Kulick et al. [48], which is used here for validation of the LES. Benson and Eaton [9] attest that the wall roughness of the test section in [48] is comparable to the rig investigated by them with an artificial roughness.

It is also interesting to consider the development of the velocity fluctuations. They are presented for both phases in Figure 6.3. The plots in the left column present the fluctuations of the gas phase and the right side, the particle velocity fluctuations. Here again the simulation results from the LES using Lycopodium particles are plotted against the measurements for the single phase flow.

It is apparent that the air fluctuations from the simulations are in reasonable unison with the experiments. In contrast, the particle fluctuations estimated from the LES deviate significantly from the experimental data. For all classes, the LES profiles of the particle streamwise fluctuations reproduce the experimental data closely for distances from the wall of $y^+ > 100$. For $y^+ > 100$, the Lycopodium particles lead the air flow. A direct comparison with an experiment for these particles is not possible. However, when taking into account the similar particle characteristics investigated in the context of the low REYNOLDS number flow, several parallels can be drawn. First, it is necessary to assume that Lycopodium does not exhibit the same complex near wall behavior as the heavier particles. The very similar result obtained by Wang and Squires [112], who carried out an LES using the same configuration, supports this assumption. According to the findings from the low REYNOLDS number simulation, the LES confirms the tendency of the DNS of Picciotto et al. [70], i.e. even the smallest particles denote higher fluctuations in streamwise than the air flow. Furthermore, the amount of the particle fluctuations prevalence is proportional to their characteristic time. Therefore, it can be assumed that the results for this class are reliable. Nevertheless, the question of a proportionality factor between the flow REYNOLDS number and the particle fluctuations at given STOKES number remains unanswered.

Considering the fluctuations of the glass particles (Figure 6.3), it appears that the streamwise component is well captured. The wall-normal component lags the experimental value across the complete channel height. The tendency augments for the copper particles. The low wall-normal velocity fluctuations can be interpreted as the reason for the higher particle mean velocity, which leads to the proposition, that the particles have a negligible interaction with the walls. According to the simulation, the maximum of the streamwise velocity fluctuations of the copper particles occurs much closer to the wall than the position observed in the experiment ($y^+ \approx 20$). Kulick et al. [48] report a bimodal particle velocity distribution at $y^+ \approx 12$, and for this, the fluctuations cannot be interpreted as the squared variance of a GAUSSIAN distribution. The bimodal velocity distribution was not confirmed by the recent simulations. Moreover, the particle velocity distribution was also studied in the region around the maximum predicted by the LES.

Benson and Eaton [9] investigated the influence of the wall roughness on the near wall particle velocity distribution for glass particles. In smooth wall conditions the bimodal particle velocity distribution vanishes. In addition, the mean particle velocity profile develops much more similarly to that of the carrier fluid. Nevertheless, the experiment in [9] does not explicitly investigate the effect of particle rotation (common for real particles) on the statistical properties

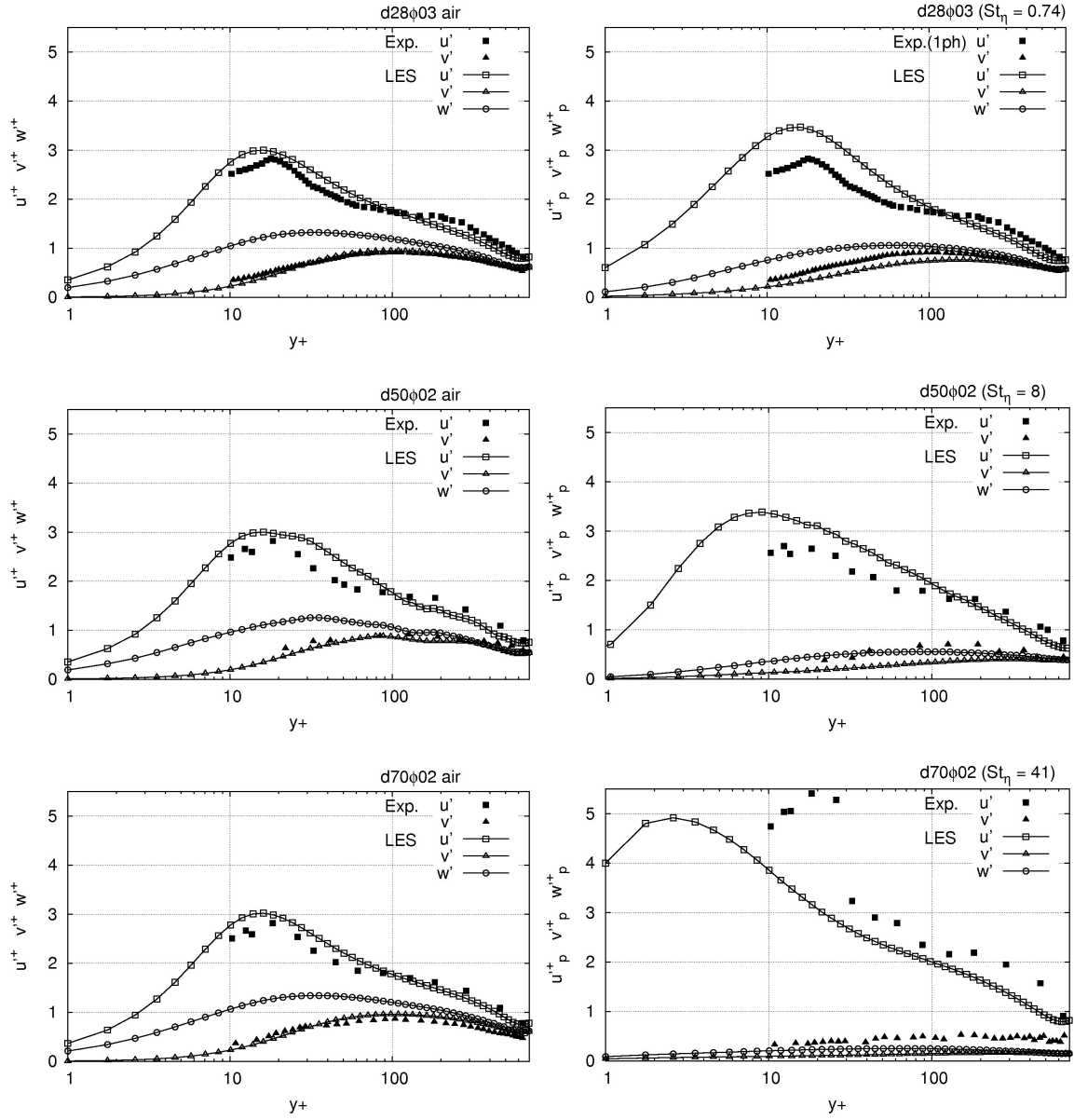


Figure 6.3: Channel flow $Re_\tau = 644$: Air (left) and particle (right) velocity fluctuations for the flows with 2 % mass loading. The different particle classes in the flow are 28 μm Lycopodium ($St_\eta = 0.74$), 50 μm glass ($St_\eta = 8$) and 70 μm copper ($St_\eta = 41$). y^+ is the wall-normal coordinate. Experimental data are taken from Kulick et al. [48].

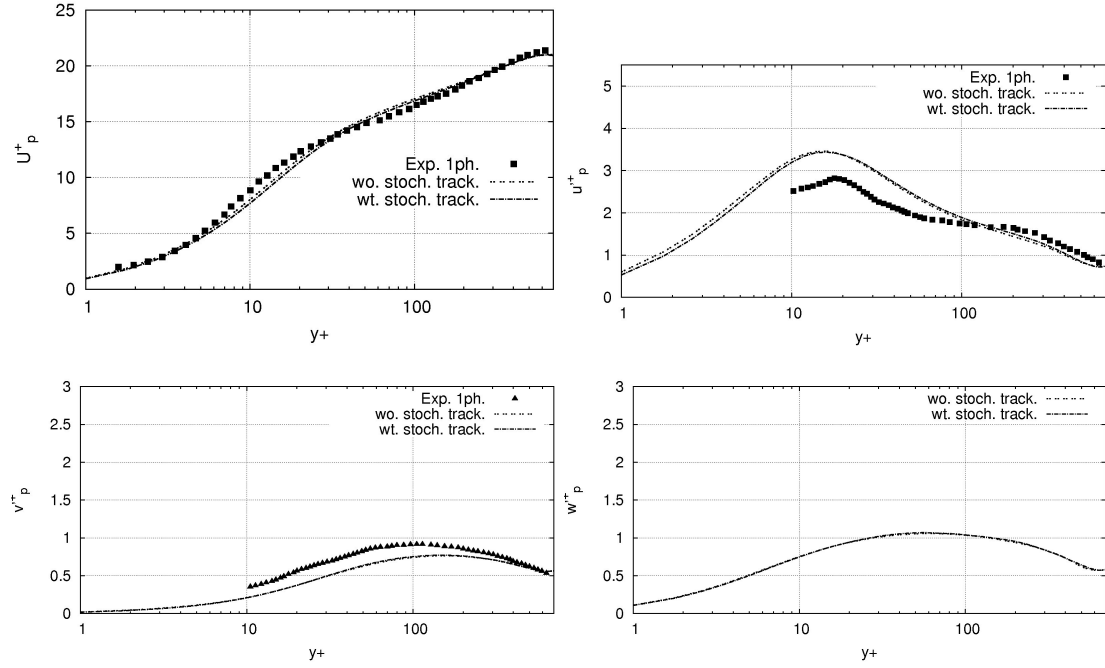


Figure 6.4: Channel flow $Re_\tau = 644$: Particle mean velocity and velocity fluctuations for the flow with $28 \mu m$ Lycopodium particles ($St_\eta = 0.74$) at 2 % mass loading. Comparison with the experimental data from Kulick et al. [48] corresponds to single phase flow measurements.

combined with rough wall boundary conditions. In smooth wall conditions, the particle rotation does not affect the particle velocity.

Within this simulation setup, a smooth wall with elastic particle-wall collisions is assumed. The coefficient of wall restitution is equal to one. Particle rotation is omitted.

According to the investigations of Young and Leeming [116], it is expected that the Lycopodium particles are very sensitive to the structures unresolved by the LES, since they belong to the *diffusion-impaction regime*. Consequently, particle–eddy interaction is essential for correct particle dispersion. The potential error was already discussed in the context of the low REYNOLDS number channel flow, where it is referred to the work of Kuerten and Vreman [45] and Kuerten [46]. A simple stochastic tracking model is applied to investigate the effect of the unresolved structures on the particle velocity statistics. For these, the sub-grid kinetic energy is estimated from the resolved strain rate tensor. Further, isotropy for the unresolved scales is assumed. The fluctuating velocity u'_{sgs} is estimated from the sub-grid stress kinetic energy k_{sgs} following the isotropy assumption. u'_{sgs} is multiplied by a stochastic number (assuming GAUSSIAN distribution) and is finally superimposed with the resolved flow velocity $\tilde{u}_{i,@p}$ at the particle position. Since the flow behavior, in terms of mean and fluctuating quantities, is predicted very well, it can be assumed that the estimated kinetic energy is reasonably well approximated.

A comparison of the results from the simulation with and without the sub-grid stress stochastic dispersion model is shown in Figure 6.4. The influence on the particle velocity seems to be negligible. This leads to the conclusion that either all significant scales are resolved, or the effect of the additional dispersion model impacts other particle properties, as confirmed by a closer study of the particle preferential concentration. This is discussed in detail in the next Section 6.1.2. To draw conclusions on the potential influence of a sub-grid stress model for particle dispersion on

particle velocity statistics, it should be noted that additional simulations with $50\ \mu\text{m}$ and $70\ \mu\text{m}$ particles involving a sub-grid stress model did not produce different velocity characteristics to the simulations without the model. Furthermore, the present results do not affirm the thesis proposed by [45] as aforementioned in the context of the low REYNOLDS number channel flow but certainly are in unison with the findings of Armenio et al. [5]. It should be emphasized, that the present simulation and this performed by Armenio et al. [5] apply comparable spatial resolution of the domain, which is higher than the resolution used by [45].

In general, the simulations involving the Lycopodium and the glass particles provide reliable results in terms of mean and fluctuating velocities. The impact of high particle inertia (which the case with $70\ \mu\text{m}$ represents) and particle–wall collision effects becomes limiting factors for using the simulation as a predictive tool. In flows containing heavy particles, where the particle–wall interaction plays a major role in the formation of the flow pattern, the development of reliable models accounting for the fluid–particle–wall interaction system becomes inevitable.

The last configuration considered in this section is a particle-laden jet flow (Section 4.3). It provides the opportunity to study the particle behavior in a turbulent shear flow without the additional influence of walls. In the following, the particle and the fluid velocities are investigated based on configurations $d40\phi13$ and $d80\phi23$, as in Table 4.13. Here again, the dispersed phase consists of glass beads with a mean diameter of 40 and $80\ \mu\text{m}$, respectively. The carrier fluid is air. The significant difference between this setup and both previously presented channel flows is the high STOKES number St_l , here defined using the integral time scale of the flow. In configuration $d40\phi13$, the value estimated at the jet inlet is $St_l = 9.65$. The corresponding number for configuration $d80\phi23$ is $St_l = 40$. Since the time scale increases quadratically with the axial distance ([37]), the STOKES number for the small particles at the last measurement position approaches a value of $St_l = 8$. For comparison, the STOKES numbers based on the integral time scale in the high REYNOLDS number channel flow configuration are $St_l = 0.57$ (glass particles) and $St_l = 3$ (copper particles).

Verification of the results obtained from the LES is based on comparison with the experimental data from Hardalupas et al. [37]. In all plots the position coordinates (axial (x), radial (r)) are normalized by the jet inlet diameter D . Quantities corresponding to the dispersed phase are denoted by the index p . The axial and the radial velocities are denoted by u and v , respectively. Figure 6.5 shows the centerline mean velocity decay and the axial velocity fluctuations in the same direction for both phases. The axial velocity fluctuations of both phases are normalized by the fluid mean velocity along the jet axis U from the two-phase flow. Since the fluid velocity of the particle-laden jet in the case $d40\phi13$ is not measured, it is plotted against the single phase flow experimental data. Comparison with data from the single phase LES confirms the assumption that the fluid in the particle-laden flow is not visibly affected by the momentum transfer from the dispersed phase. In contrast to the fluid velocity, the particle velocity decay along the jet axis is considerably overestimated from position $x/D \approx 10$ by the simulation. It is important to note, that the data provided do not concern the self-similar region of the jet (Hardalupas et al. [37]). The axial velocity fluctuations of the fluid are relatively well predicted by the LES. Considering the particle velocity fluctuations downstream from position $x/D \approx 5$, it can be stated that their magnitude approximates the experimentally obtained value. Within the jet core region, however, the values are extremely underestimated, which can be explained by the influence of the particle inflow conditions together with a relatively short inlet pipe sec-

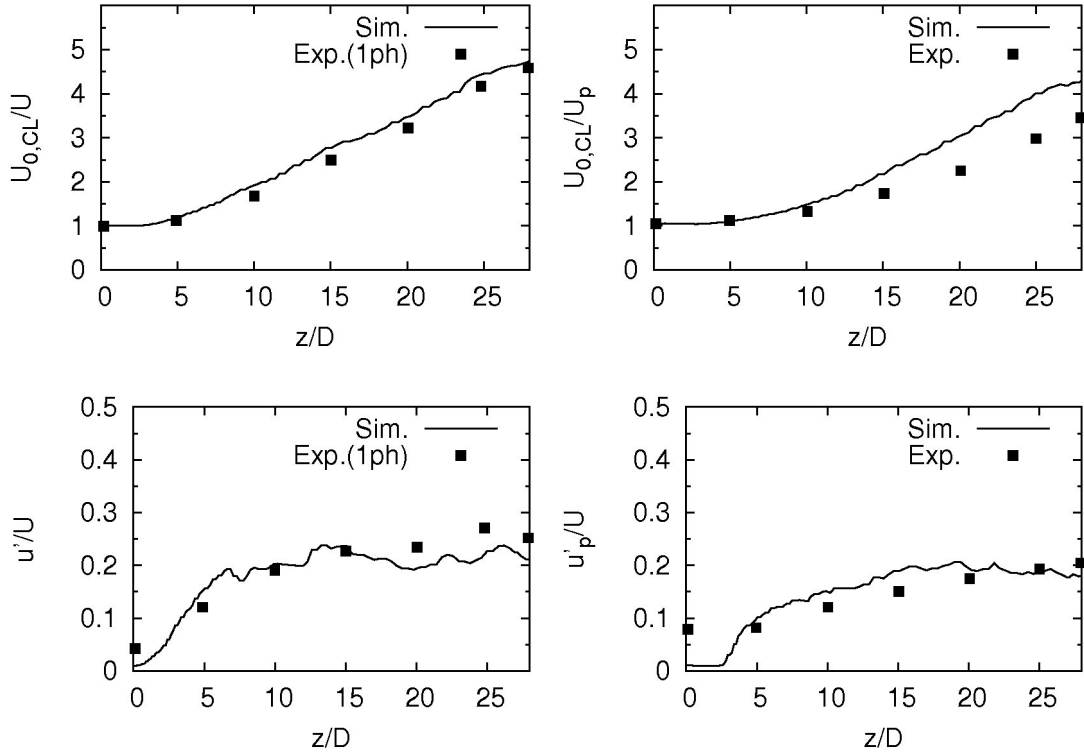


Figure 6.5: Free jet flow $Re_{bulk} = 13000$: Fluid (left) and particle (right) mean axial velocities and the corresponding fluctuations along the jet axis. LES configuration - $d40\phi13$, STOKES number $St_l = 9.65$. Experimental data from Hardalupas et al. [37]. $U_{0,CL}$ is the centerline velocity of the fluid at the jet inlet.

tion. The particles are injected with a velocity equal to the instantaneous fluid velocity at the particle position. Nevertheless, it is possible that the development of the jet shear layer further downstream biases the particle motion significantly. An additional aspect presents the potential influence of particle–wall interactions. Before proceeding with the analysis of this effect, it is useful to have an additional view of the simulation results in terms of their radial velocity profiles. These are shown in Figure 6.6 in terms of the axial mean velocity of the particles and the axial in radial components of the particle velocity fluctuations. The profiles correspond to configuration $d40\phi13$ and present data at four axial positions up to $x/D = 28$. From the particle mean velocity comparison in Figure 6.6 it is obvious that the spreading rate of the dispersed phase is overestimated, which explains why the particle velocity decreases more strongly along the jet axis than it does in the experiment. The axial fluctuations of the particle velocity are well predicted in general. At $x/D = 0.1$, however, the axial particle fluctuations are extremely underestimated by the simulation. The measurements are made very close to the jet exit position and so the velocity profile is assumed to be very similar to the profile within the supplying pipe. Thus, it is appropriate to investigate the particle velocity within the inlet pipe section. At this point, it is useful to translate the issue to a configuration that has a focus on pipe flow. Such an example can be found in the work of Caraman et al. [13]. Moreover, the magnitude of the particle fluctuations obtained from the reference experiment of Hardalupas et al. [37] is very similar to the values obtained in the experiment on particle-laden pipe flow of Caraman

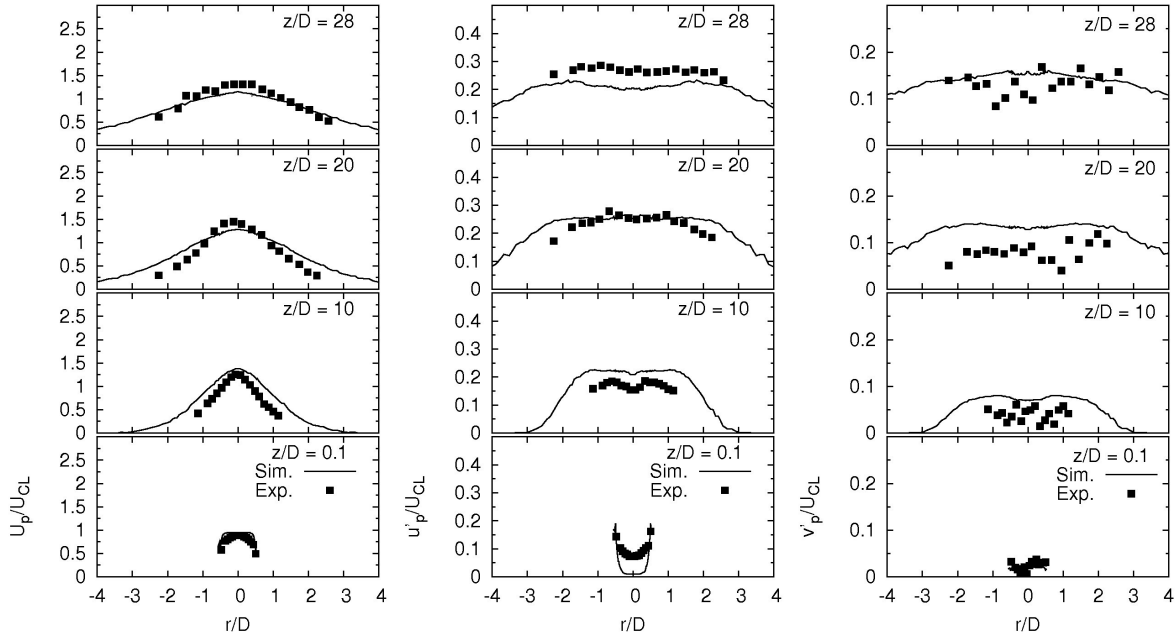


Figure 6.6: Free jet flow $Re_{bulk} = 13000$: Particle mean axial velocities and fluctuations in axial and radial directions. LES configuration - $d40\phi13$ with STOKES number $St_l = 9.65$. Experimental data are from Hardalupas et al. [37].

et al. [13]. The particle mass loading and particle diameter in [13] are comparable to that of Hardalupas et al. [37]. From the information provided in Caraman et al. [13] it is clear that the particle fluctuations are higher than those of the gas phase, also in the region far away from the wall.

There are two aspects, that need to be investigated in context of this LES:

- The artificial injection conditions for the dispersed phase together with the relatively short length of the inlet pipe section.
- The models employed to capture the particle behavior do not include all relevant phenomena.

For the first aspect, it seems that assuming equal inlet velocities for both phases introduces an error. Nevertheless, it is doubtful whether a longer inlet pipe section will lead to the desirable results. Vreman [109] reports a large discrepancy between his simulation results (DNS of a particle-laden pipe flow) and the experiment of Caraman et al. [13]. The DNS is applied to a periodic pipe, therefore, the results of the simulation correspond to a fully developed flow. The particle axial fluctuations obtained from Vreman [109] lead the gas fluctuations, however, they do not reproduce the experimental profile as demonstrated by Caraman et al. [13]. There, the dispersed phase fluctuations are much higher than those predicted by the DNS. Furthermore, the particle velocity fluctuations have a fairly uniform distribution over the pipe cross section according to the experiment, which is not observed in the simulation results provided by Vreman [109].

The issue of additional phenomena seems to be more relevant here. According to the previous findings in this section related to the high REYNOLDS number channel flow, it is evident

that real particle–wall interaction can not be approximated by simplified rebound models, as commonly applied in many studies. The influence of particle–particle collision also becomes significant at higher mass loadings, as in Vance et al. [107] and Yamamoto et al. [115]. Nevertheless, the additional models for particle–particle collision and particle–wall collision, used on different particle types and mass loadings, lead to inconsistent conclusions. The general tendency observed when considering particle–particle collisions is the flattening of the particle mean velocity profiles and up to some degree those for the particle velocity fluctuations ([107], [115]). Additional models considering the wall roughness and the modified particle–wall collision have only limited success in moderate particle mass loadings, as reported by Vreman [109]. It is obvious that until now the best solution for realistic inlet conditions that can guarantee high probability of success is to apply available experimental data as the inlet conditions, especially if relatively short inlet sections are modeled as they are here. Unfortunately, such information about the conditions inside the supplying rig are seldom found in experimental work on free jet flows.

The deficiency in the inlet axial fluctuations of the particles (Figure 6.6) leads to another interesting effect. The radial velocity fluctuations of the particles show a systematic overestimation. This seems to have settled further downstream from axial position $x/D \approx 10$. The reason for this particular behavior is therefore sought in the region close to the jet inlet. With the aid of

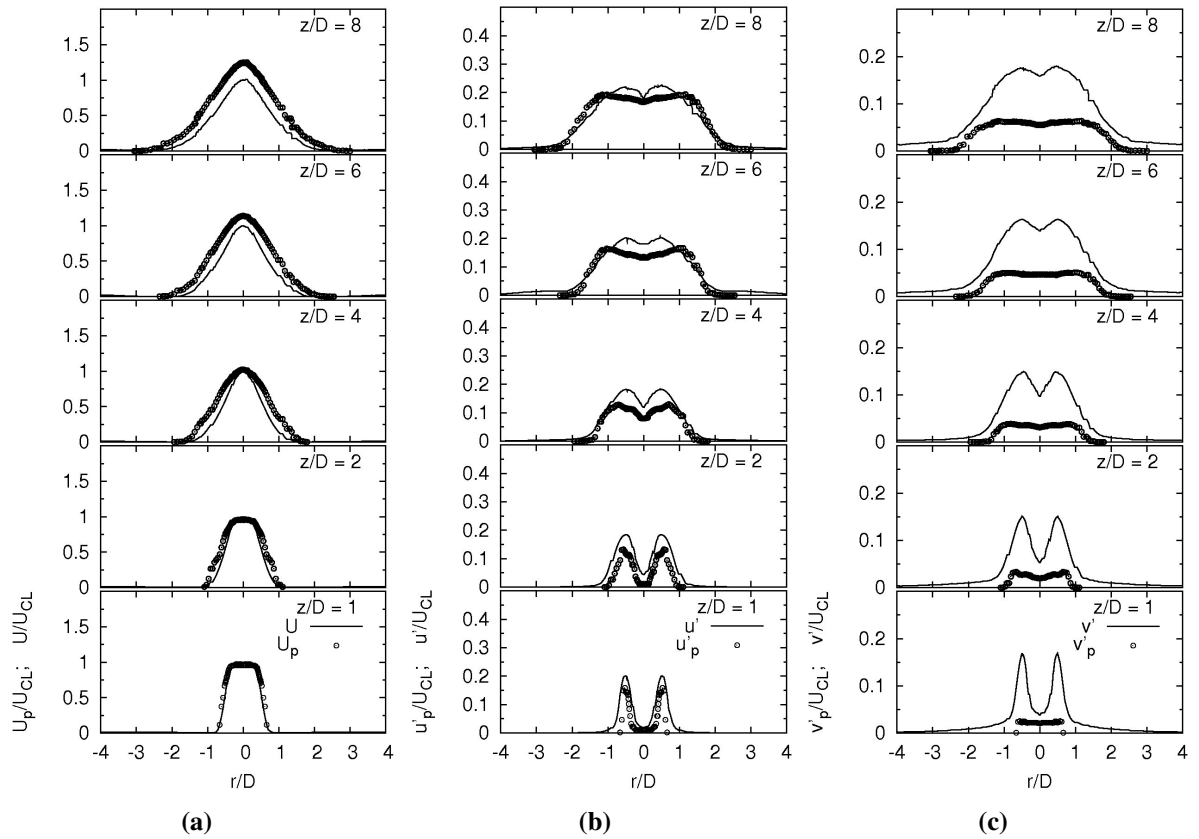


Figure 6.7: Free jet flow $Re_{bulk} = 13000$: Radial profiles of the particle and the gas mean axial velocity and the corresponding axial and radial fluctuations at different axial positions. LES configuration $d40\phi13$, STOKES number $St_l = 9.65$.

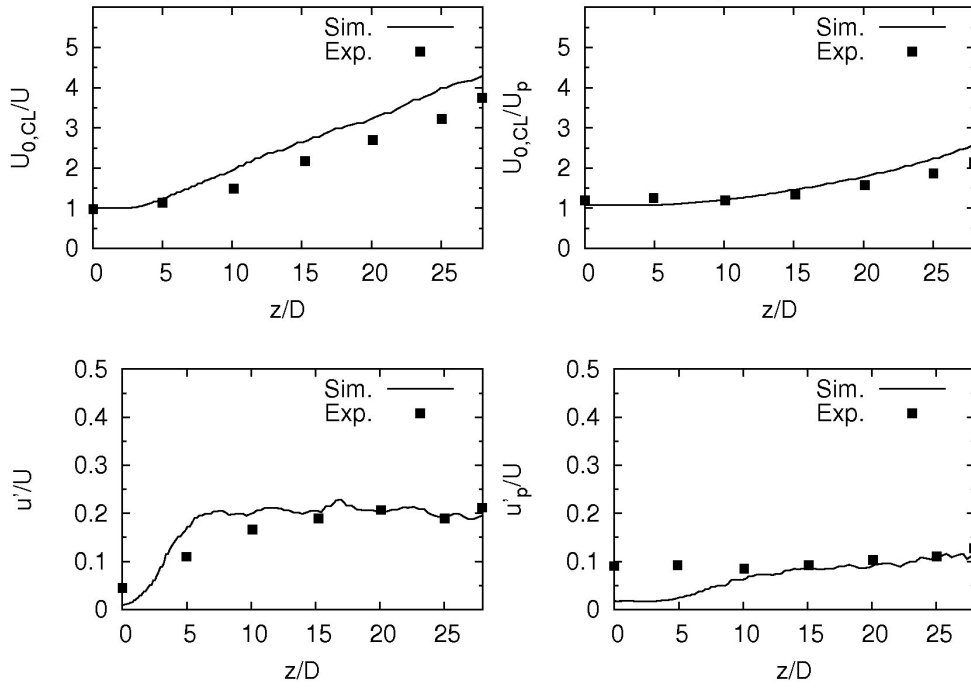


Figure 6.8: Free jet flow $Re_{bulk} = 13000$: Fluid (left column) and particle (right column) mean axial velocities and the corresponding fluctuations along the main jet axis. LES configuration - $d80\phi23$, STOKES number $St_l = 9.65$. Experimental data from Hardalupas et al. [37].

the next plot in Figure 6.7, the competing behavior of particles and gas can be examined. The evolution of the mean axial velocity and the velocity fluctuations in axial and radial direction can be pursued for the region between the jet inlet and an axial position up to $10D$. According to the mean and fluctuating axial velocity profiles in Figure 6.7(a) and 6.7(b), both phases possess quite similar behavior. There is a slight tendency for the particles to lead the air flow, as evident from the mean velocity profiles. The axial fluctuations of the particles are lower in this region. Downstream evolution of the radial fluctuations of both phases, however, is very different. The dispersed phase fluctuations v'_p lag those of the gas phase significantly and the profiles remain relatively flat compared to the corresponding gas profiles. Further downstream, the profiles become more similar in their radial extension. It seems that up to $x/D = 10$, the influence of the carrier fluid fluctuations on the dispersed phase is significant, despite the fact that the particle STOKES number is quite high ($St_l = 9.65$). In conclusion, it is possible that the increased turbulent particle dispersion in the region $x/D < 10$ is the reason for the increased spreading rate of the particle jet further downstream, as observed in the previous plots (Figure 6.6).

Using very similar inlet condition, an LES is performed on the case with $80 \mu m$ beads ($St_l = 40$). The configuration corresponds to case $d80\phi23$ in Table 4.13. In Figure 6.8, the axial mean and fluctuating velocities of carrier and dispersed phase are presented along the jet axis, x . In contrast to the small particles (case $d40\phi13$), the centerline decay of the mean axial velocity for both phases is predicted very well in this configuration. The particle velocity fluctuations are significantly underestimated for $x/D < 10$. However, their value approximates the experimental data further downstream quite well. The radial profiles of the particle mean and

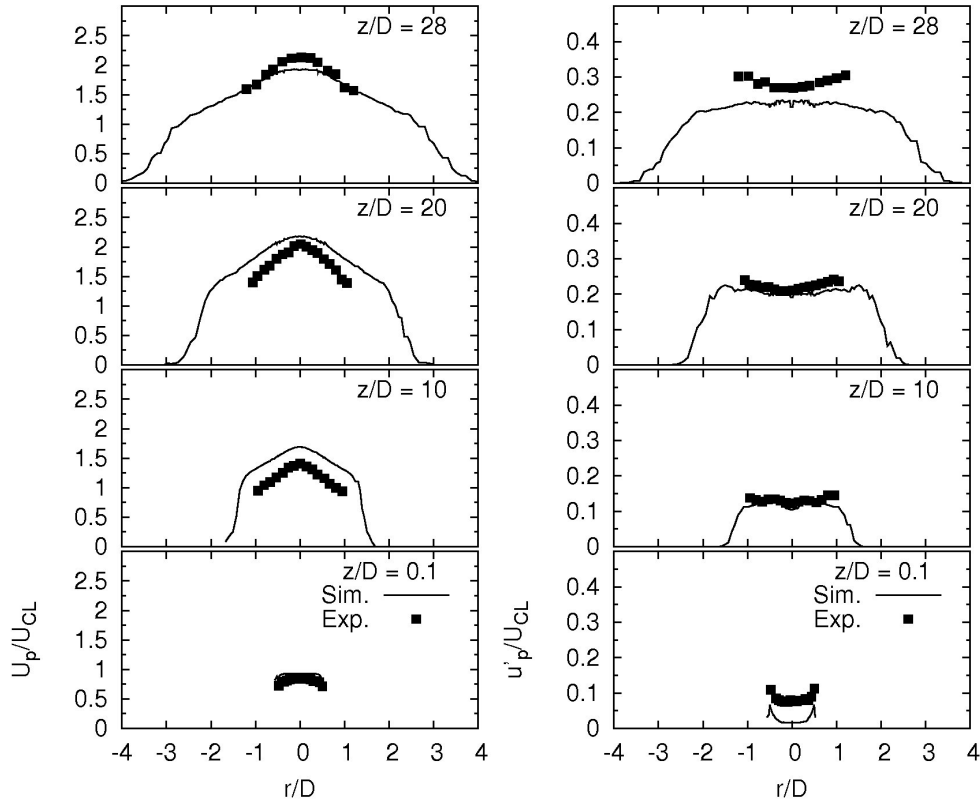


Figure 6.9: Free jet flow $Re_{bulk} = 13000$: Particle mean axial velocities and the corresponding velocity fluctuations. LES on configuration $d80\phi23$ with STOKES number $St_l = 40$. Experimental data from Hardalupas et al. [37].

fluctuating axial velocity, U_p and u'_p , corresponding to case $d80\phi23$, are presented in Figure 6.9. They confirm that the particle jet spreading rate is retained well up to $z/D = 20$ and is slightly overestimated afterwards. The gas phase velocity field is in very good agreement with the experiments. The behavior of the gas phase is the main topic of Section 6.2 and will be discussed in more detail there.

To conclude the discussion on the particle velocity prediction using LES on a free jet flow, a few aspects need to be highlighted. First, the inlet particle conditions are a critical issue in this configuration. The issue of obtaining a more realistic velocity field for the dispersed phase cannot be resolved by considering a longer pipe section, which other authors have found (Vreman [109], Vance et al. [107]), including the discussion of the channel flow configurations above. Considering the relatively high STOKES number of the $40 \mu m$ particles used for the simulation, the significant influence of the carrier fluid on the particle dispersion appears surprising at first. However, the STOKES number considered here is based on turbulent scales along the centerline of the jet. Since the "interface" between the out-coming jet flow and the environment is exposed to strong shear, the rate of turbulence generation in the peripheric region increases rapidly above that in the core flow. The turbulent structures generated on the interface have a much higher intensity than the internal jet structures, and are therefore the relevant structures in the fluid–particle interaction.

6.1.2 Particle Dispersion and Preferential Accumulation

In advanced level computations of particle heat transfer, evaporation and combustion the accuracy of the local particle distribution prediction is vitally important. In the following, the behavior of particle concentration in a turbulent flow is investigated in terms of averaged and instantaneous quantities. In addition, instantaneous concentration plots from flow regions with nearly homogeneous and isotropic turbulence are compared to findings from previous DNS and experimental studies.

6.1.2.1 Local Particle Accumulation

The influence of the STOKES and fluid REYNOLDS number

Typical particle behavior in a turbulent flow is demonstrated in Figure 6.10. The plots represent particle positions in an xz -plane along the centerline in a channel flow (the *midplane*). The different views correspond to particle classes with different STOKES numbers St_η . It should be emphasized that the results presented correspond to simulations on channel flows with two different REYNOLDS number: the low REYNOLDS number flow case with $Re_{bulk} = 2110$ and the high REYNOLDS number flow case with $Re_{bulk} = 13800$. The range of St_η considered here varies from 0.04 up to 19. It is further evident that particle classes with $St_\eta \approx 1$ demonstrate the highest propensity to accumulate. In addition, the particle class with $St_\eta = 0.74$, which is tracked in the high REYNOLDS number flow, fits into the given order well, i.e. according to their visual degree of accumulation. This qualitative observation is in agreement with the investigations of Wang and Maxey [111]. They showed that the maximum preferential accumulation is observed for particles with $St_\eta \approx 1$ and that the degree of accumulation scales with the KOLMOGOROV time scale τ_η . Nevertheless, their findings are based on LAGRANGIAN particle tracking in *homogeneous isotropic* turbulence (DNS), which is unambiguously related to the fact that the turbulent structures with the highest intensity are in the order of the smallest scales (Ruetsch and Maxey [84]). Since this particular observations on the results from the present work are restricted to the channel midplane (i.e. far away from the wall), comparison with findings of Wang and Maxey [111] and similar works is suitable.

To investigate the effect of the flow REYNOLDS number on the behavior of particles with similar STOKES numbers, results from both channel flow configurations are considered and analyzed in parallel. An overview of these, together with the corresponding particle classes in terms of STOKES numbers, is provided in Table 6.1. The data from the high REYNOLDS number channel flow simulation address the configurations with particle mass loading of 2 %, except for the case with Lycopodium particles, where the loading is 3 %. The effect of the dispersed phase on the fluid turbulence is assumed to be negligible.

More quantitative information, compared to the instantaneous plots in Figure 6.10, permits the investigation of probability density functions (PDF) for the particle number density. For this purpose, a procedure for the PDF evaluation, similar to that used in Fessler et al. [31], is used. The reliability of the simulations in predicting of preferential accumulation is assessed in terms of information extracted from the PDFs of both the LES and experimental data from Fessler et al. [31]. To retain similarity with the experiment, a 1 mm thick sheet in the midplane of the channel is considered. The plane is discretized with regular mesh of equidistant square cells (boxes). This mesh is independent from the numerical grid used for the simulations. All

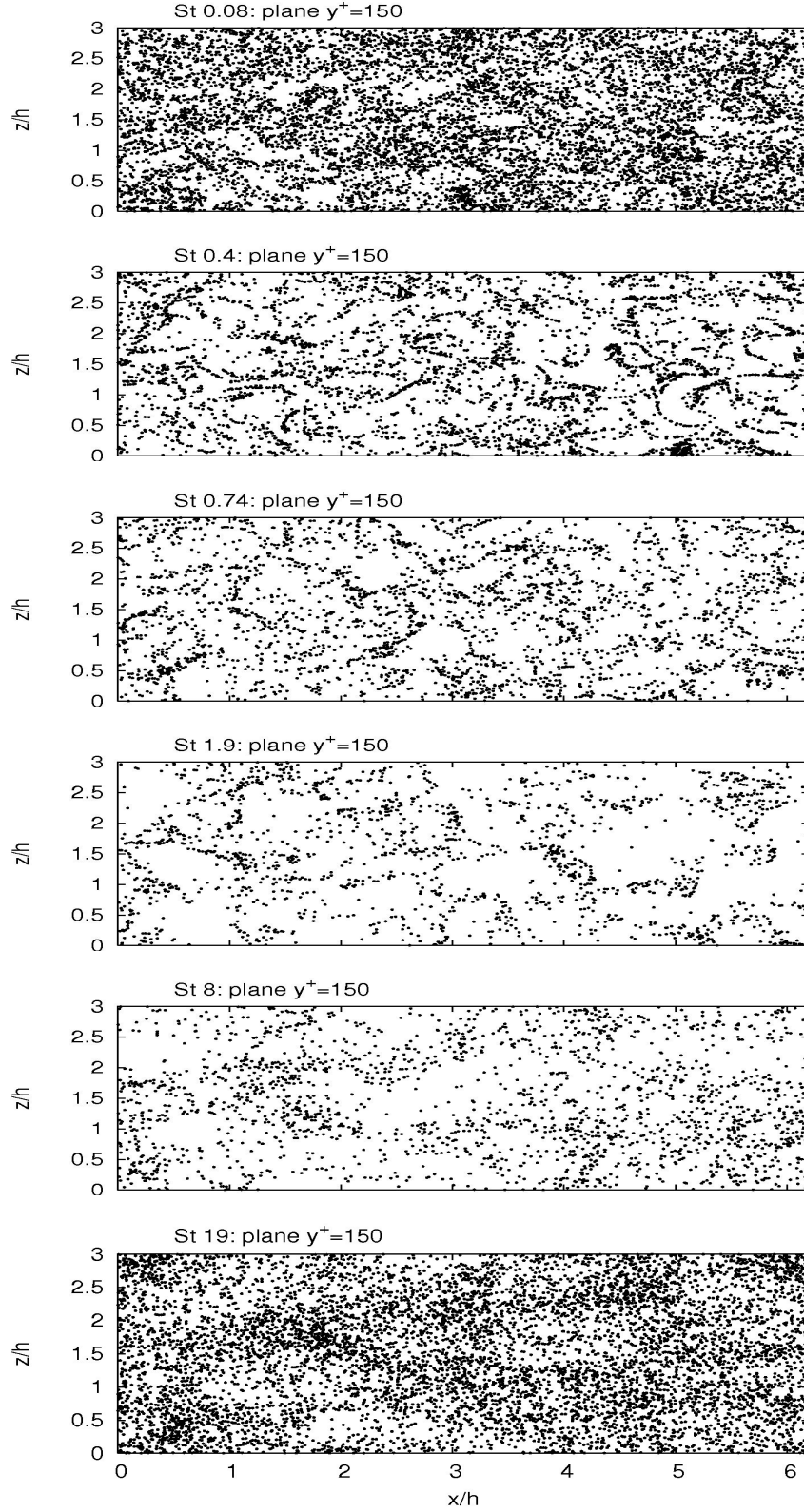
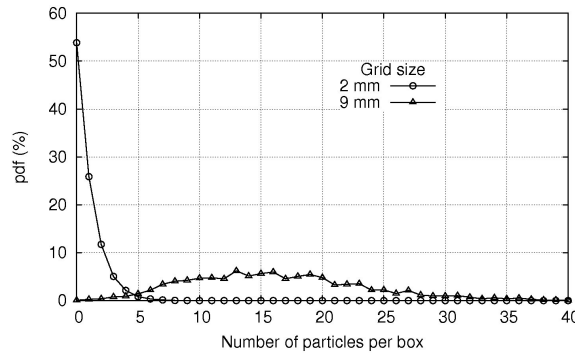


Figure 6.10: Channel flow $Re_\tau = 150$ and $Re_\tau = 644$: Instantaneous particle positions at $y^+ = 150$ (channel midplane). Particles with $St_\eta = 0.08, 0.4, 1.9$ belong to the low REYNOLDS number channel flow simulation. Particles with $St_\eta = 0.74, 8, 19$ belong to the high REYNOLDS number channel flow simulation.

Table 6.1: Configurations used for investigation of local preferential accumulation of particles.

Reference configuration	Case	St_η
Channel flow, $Re_\tau = 150$	St1 ¹⁾	0.08
	St5	0.4
	St25	1.9
Channel flow, $Re_\tau = 644$	$d28\phi03$	0.74
	$d50\phi02$	8
	$d90\phi02$	19

1) STOKES number as defined in Table 4.4.

**Figure 6.11:** PDF of the particle number density for case $d28\phi03$ (channel midplane) estimated for different grids.

particles with spatial coordinates within a particular box are assigned to it and the associated number density is computed. The final PDF is computed from the number densities. The PDF has a different form depending on the grid size. In Figure 6.11, an example of PDFs for the case $d28\phi03$ obtained on grids with cell length of 9 mm and 2 mm is shown. The evaluation of the degree of preferential accumulation is based on the comparison of the calculated PDF with a PDF obtained for the same number of particles, assuming purely random distribution. For randomly distributed particles, the probability $P(n)$ of finding n particles in a particular box is a POISSON distributed quantity. According to this, the random distribution is given by Equation (6.1).

$$P(n) = \frac{e^{-\mu} \mu^n}{n!} \quad (6.1)$$

μ denotes here the mean number of particles per box. The normalized difference D_{dev} is used to quantify the deviation of the simulated distribution from the POISSON distribution. It is defined as the standard deviation σ of the computed distribution and that of a POISSON distribution, $\sigma_{poisson}$, having the same mean value μ .

$$D_{dev} = \frac{\sigma - \sigma_{poisson}}{\mu} \quad (6.2)$$

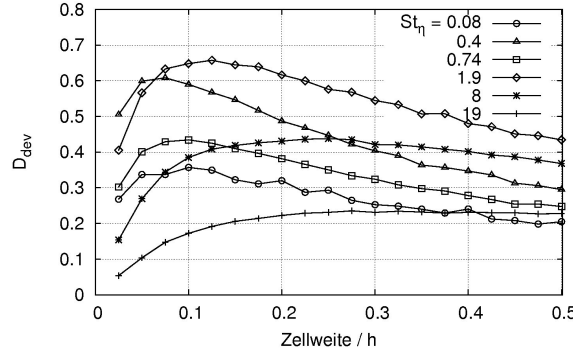


Figure 6.12: D_{dev} , as defined in Equation (6.2) as a function of the grid size for different particle STOKES numbers. Particle classes corresponding to Table 6.1.

D_{dev} is normalized by the mean particle number per box. Positive values for D_{dev} correspond to situations with preferential accumulation, since a large σ value indicates that there are boxes with a very high number of particles and such a with very low number. In a uniform particle distribution, the standard deviation is zero and D_{dev} becomes negative. $D_{dev} = 0$ describe randomly distributed particles.

As already mentioned, depending on the grid size applied for the PDF evaluation, its form can vary greatly because the typical length scale of accumulation varies. Therefore, the PDF with maximum deviation from the POISSON distribution, according to (6.2), represents the degree of particle accumulation most accurately, since it matches the scale present best. The limited a priori information about the optimal grid size implies an iterative process for its estimation.

In the present context, the PDFs of the particle number density are computed for a grid size ranging between 0.5 mm and 10 mm . The estimated degree of *non-randomness* in terms of D_{dev} is shown in Figure 6.12 as a function of the grid size used for the PDF computation. The grid size is normalized with the channel half height, h . The deviation from the POISSON distribution exhibits a local extremum (maximum) for all particle classes. This appears for particles with $St_\eta \leq 1$ for a similar grid resolution of approximately (≈ 0.1). For particles with higher STOKES number, though, this maximum seems to be shifted toward larger box sizes. This can be interpreted as further information related to the scales at which the accumulation occurs. According to conclusions made by Wang and Maxey [111], particles with $\tau_p/\tau_\eta \approx 1$ experience the highest degree of accumulation. Particles with $\tau_p/\tau_\eta \approx 2$ have almost 40 % lower values of D_{dev} . Squires and Eaton [100] confirm maximum accumulation at $\tau_p/\tau_\eta \approx 1$ as well by performing DNS of isotropic turbulence with heavy particles. In contrast to this, the highest degree of non-randomness, according to the LES here, is detected for particles with $\tau_p/\tau_\eta = St_\eta = 1.9$. The investigations of Fessler et al. [31] on the particle dispersion in a channel flow turbulence have shown that the preferential accumulation is most pronounced for particles with $St_\eta = 2.2$. However, this behavior was claimed to be caused by the wider range of scales in the experiment ($t_0/\tau_\eta \approx 22$). In contrast to this, the simulation of Squires and Eaton [100] considers flow with ($t_0/\tau_\eta \approx 10$). Another possible explanation, given by Fessler et al. [31], was that the PDFs obtained from DNS are based on the computational grid and their dependency on the grid size is not further evaluated. The two-phase LES considered here is consistent with the experiment. The second, and to the authors best knowledge, it is a new observation that the findings of Fessler et al. [31] in a high REYNOLDS number flow are

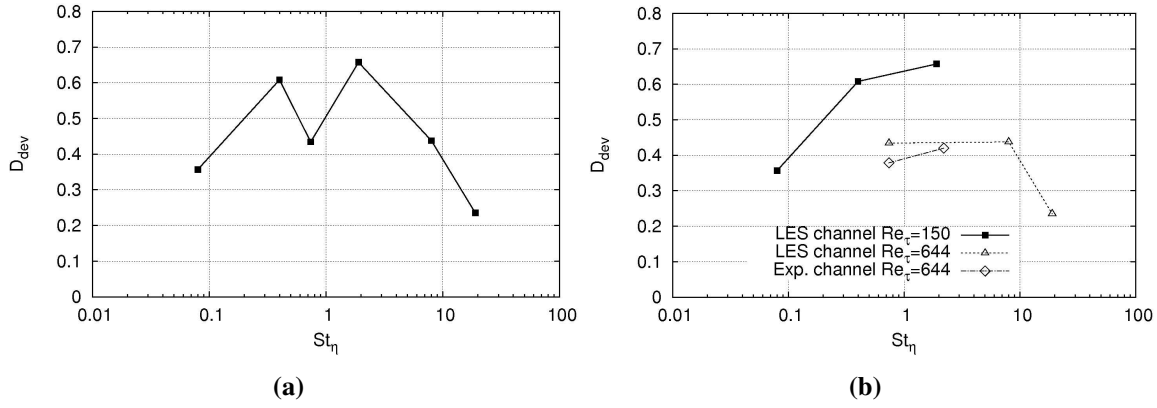


Figure 6.13: Maximum deviation, D_{dev} , from the POISSON distribution (Equation (6.2)) as a function of the particle STOKES number.

herewith reported for very low REYNOLDS number flow. The estimated scale separation for this flow, estimated at $t_0/\tau_\eta \approx 6$, is lower than that used in the flow simulation of Squires and Eaton [100].

The dependency of the maximum value estimated for D_{dev} on the particle STOKES number is presented in Figure 6.13(a). All particle classes are considered in the plot. The maximum value for D_{dev} is the same as estimated in Figure 6.12, i.e. independent from the grid size for which it was detected. There is a significant decrease of D_{dev} for the particle class $St_\eta = 0.74$. An alternative plot of the same data is presented in Figure 6.13(b), which seems to resolve the contradictory behavior of D_{dev} . Separate lines explicitly highlight the data corresponding to the different channel flows. The tendency of particle accumulation is confirmed in both channel flows. Nevertheless, the magnitude of the deviation from the random state shows significant discrepancies, depending on the flow REYNOLDS number. In addition, the magnitude of D_{dev} is given, as detected for the particles with $St_\eta = 0.74$ and $St_\eta = 2.2$ in the experiment of Fessler et al. [31]. The second class denotes maximum degree of accumulation. This particle class is not included in the present simulation set.

It was not possible to obtain a reliable estimation of the local accumulation in the channel from the available database for the dispersed phase in the low REYNOLDS number channel flow (Marchioli and Soldati [54]), since the number of particles used by the authors is too low for that purpose. Marchioli and Soldati [54] computed 10^5 particles, which was sufficient to obtain reliable statistical information in the context of their objectives. The two-phase LES performed here has $15 \cdot 10^5$ particles.

In conclusion, predicting local accumulation of particles according to the results follows the findings from previous works. However, particularly anomalous behavior of D_{dev} (commented in the context of Figure 6.13(a)) leads to the assumption that the influence of the flow REYNOLDS number leads to varying accumulation behavior.

Influence of the Sub-grid Turbulent Dispersion

As discussed in Section 6.1.1 (Figure 6.4), the consideration of a model for turbulent particle dispersion that accounts for the effect of sub-grid velocity fluctuations does not affect the particle velocity statistics, according to the simulations here. Nevertheless, it has been shown (Pozorski and Apte [74], Fede and Simonin [28], Kuerten [46]) that unresolved scales contribute

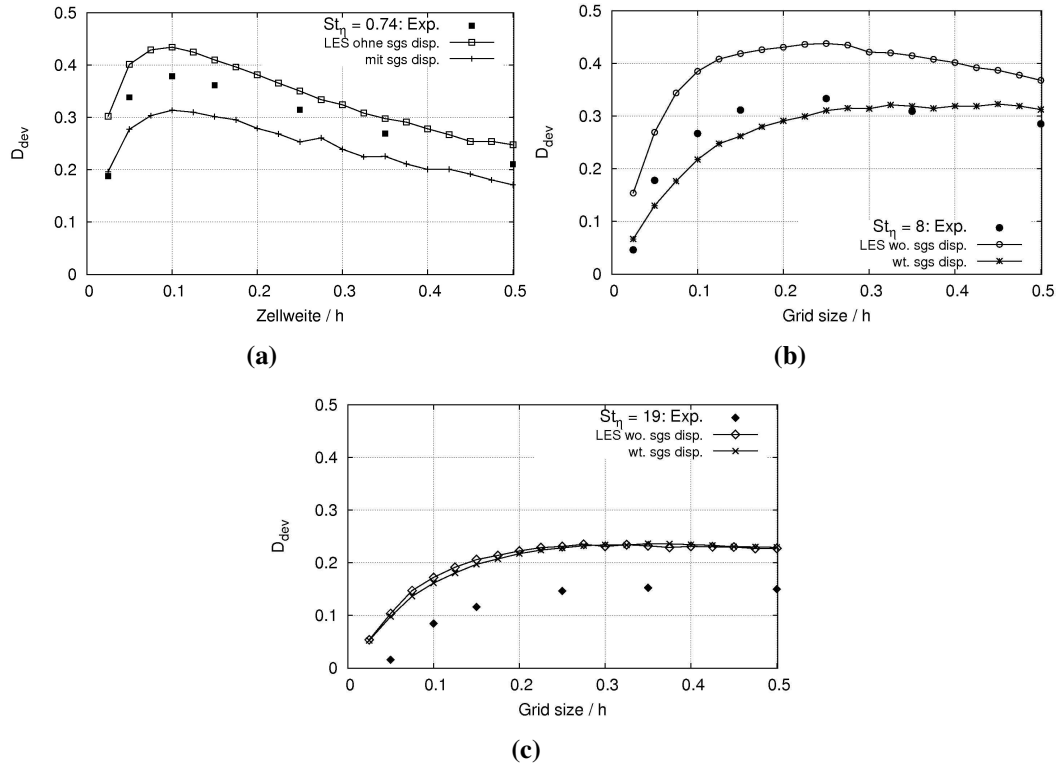


Figure 6.14: D_{dev} , as defined in Equation (6.2), for $St_\eta = 0.74, 8, 19$ (case $d28\phi03, d50\phi02$ and $d90\phi02$ from Table 4.6). Comparison with experimental data from Fessler et al. [31].

to the evolution of the local and the mean particle concentration. In the following, this aspect is investigated in the context of the high REYNOLDS number channel flow with low particle mass loading of 2 %. Figure 6.14 presents D_{dev} , (Equation (6.2)), as estimated for the midplane of the channel as a function of the grid size, used to compute the particle number density. Deviation from the POISSON distribution is evaluated from particle data corresponding to simulations with and without an additional model (Section 2.2.4.3) for the sub-grid stress turbulent dispersion. In Figure 6.14(a), D_{dev} , estimated for both simulations together with the experimental data from Fessler et al. [31], is shown as a function of the grid size. The particle class addressed here has $St_\eta = 0.74$ (configuration $28\phi03$). In general, two issues stand out from this figure. Both simulations predict the evolution of D_{dev} through the different grid sizes estimated from the experiment. Secondly, the increased particle dispersion due to the additional model introduces a large correction in the stochastic particle motion with a tendency to an artificial randomization of the particle positions. This is confirmed by the fact that the experimental data predict a systematically higher preferential accumulation.

Contrariwise, a rough estimate of the relative error between the experiment and the standard simulation, without dispersion model, computed as $(D_{dev}^{les} - D_{dev}^{exp})/D_{dev}^{exp}$ leads to an averaged value of 15 %. Considering the main mechanism for particle accumulation, it is clear that small particles will accumulate if they are heavy enough to be exposed to the centrifugal force due to the eddy rotation, but in the same time, have a response time shorter than the time for crossing the eddy, or the time for the eddy dissipation. Since particle accumulation evidently occurs, it is clear that the large eddy simulation properly resolves the turbulent structures relevant for the ac-

cumulation. From the perspective of the standard LAGRANGIAN particle tracking method, the particle accumulation in a certain volume is not restricted to the particle packing limit. Without an additional control mechanism from the particle tracking point of view accounting for "permitted" and "not permitted" particle positions, depending on the allowed particle volume fraction in the computational cell, the interaction of the particles with the fluid is the only mechanism for their redistribution from regions with high particle concentration. Nevertheless, this mechanism plays an effective role only for particles with sufficiently small residence time and diameter. Otherwise, the particle collision probability in these regions is much higher compared to the collision probability of homogeneously distributed particles at the same mass loading. It turns out that particle–particle collision is the more natural mechanism for particle redistribution. This fact is especially important when transferring conclusions from here to the large-eddy simulation of liquid sprays. The collision there will lead eventually to the coalescence (depending on the relative droplet velocity and the surface tension coefficients) rather than to further randomization of the droplet position. It is therefore crucial to differentiate between turbulent and collision dispersion observed in solid particle flows.

Despite the alternative of applying a particle collision model, a possible correction of the final particle PDF is to perform a posterior particle redistribution (different conditions can be specified) or clip the number to the packing limit for the purpose of data evaluation only. The problem with such an assumption is, however, that it is limited to the instantaneous snapshots of the particle positions. These are taken every 200 simulation time steps. Therefore, the natural dispersion due to collisions can not be captured. Such a method is expected to introduce only a small overall correction and is not applied on the data sets discussed here.

The identical solution from both simulations for the case $St_\eta = 19$ shows the limited area of influence of the dispersion model. The intermediate particle class exhibits the largest deviation between the simulations with and without the model. Furthermore, if the sub-grid stress fluctuations are considered, the discrepancy between experimental and simulation result becomes negligible. However, the comparison with the experimental data from Fessler et al. [31] should be considered with caution, since these correspond to a measurement of flow with mass loading of 40 %. According to the experiment of Kulick et al. [48], the particles do not influence the fluid statistics even at higher mass loading, which means that the particles are exposed to the same interaction with the fluid as those in the low mass loading case. Of course, a higher mass loading certainly leads to an increased particle–particle collision probability, which leads to effective dispersion.

Observations of the dispersion model and its effect on both low-STOKES-number particle classes, suggest that the model will certainly lead to the desired results if direct comparison with an experimental data is possible, however, the appropriate model constant should be estimated for every application and particle type. The model constant for all simulations reported here is set to $C = 0.15$.

Other authors have shown (Oefelein [65]), that this type of models based on eddy–life and particle–eddy interaction time can be successfully extended for LES applications. Segura [91] used several values for the constant in the model proposed by Oefelein [65] in order to facilitate the optimal for each particular configuration.

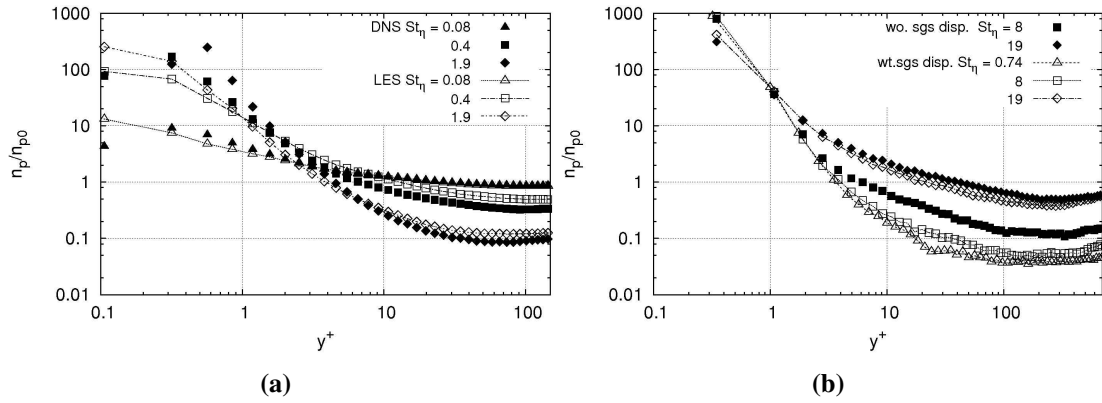


Figure 6.15: Channel flow $Re_\tau = 150$, (a), and $Re_\tau = 644$, (b): Mean particle concentration profiles in wall-normal direction for particles with the STOKES numbers $St_\eta = 0.08, 0.4, 1.9$ (a) and $St_\eta = 0.74, 8, 19, 41$ (b). DNS data in (a) are taken from Picciotto et al. [70].

6.1.2.2 Mean Particle Concentration Profiles

A typical phenomenon in two-phase wall-bounded flows is the accumulation of particles in the near wall region. In the present context, both channel flow configurations exhibit this behavior for most of the particle classes. It is possible to compare the DNS results for the particle concentration in wall-normal direction (Picciotto et al. [70]) with those obtained from the LES. The comparison is presented in Figure 6.15(a). In a similar way, the mean concentration profiles of the high REYNOLDS number channel flow are shown (Figure 6.15(b)). Since concentration data from the experiments of Fessler et al. [31] and Kulick et al. [48] are not available, only results obtained from the two-phase LES are discussed. The wall-normal coordinate is normalized with wall units. The particle number density is normalized by the value corresponding to a homogeneous particle distribution in the same direction. Both configurations demonstrate, that the particle concentration in the wall region is strongly affected by the particle STOKES number, St_η . The main discrepancy between the DNS [70] and the LES is localized in the region below $y^+ = 1$, (Figure 6.15(a)). One significant difference between both simulations is the position for which the particle-wall collision is computed, despite the numerical technique and implementation. In Picciotto et al. [70], the particle reflection at the wall is applied at a distance of $d_p/2$ from the wall. In contrast to this particle-wall collision in the present simulations occurs when the particle center encounters the wall. Therefore it is reasonable to suggest that the particle concentration estimated by the LES overestimates the one from the DNS, especially for the larger particles with $St_\eta = 1.9$. Otherwise, from a practical engineering point of view, the wall region considered is less important, since the viscous sublayer is not resolved for most practical applications. Moreover, the prediction of the mean particle concentration in the near wall region seems to be an issue also for the DNS technique, as reported in Marchioli et al. [56]. Data obtained by independent working groups using DNS, expose significant discrepancies in the prediction of the particle concentration. Marchioli et al. [56] conclude that the combinations of numerical schemes employed by the various codes provide different errors. It is further not clear, which data should be used as a reference.

Form the concentration profiles corresponding to the high REYNOLDS number case, it is evident that particle preferential accumulation near the wall can be observed up to $St_\eta = 19$.

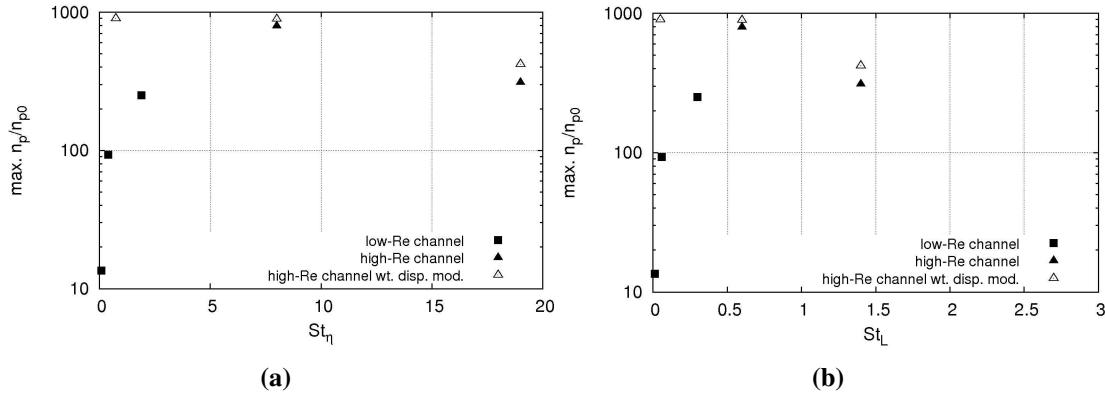


Figure 6.16: Maximum particle concentration in the near wall region as a function of St_η and St_l in a turbulent channel flow. Results from the two-phase flow LES on the high REYNOLDS number and the low REYNOLDS number channel flow.

Concerning the influence of the sub-grid stress dispersion model (the hollow symbols in Figure 6.15(b)), it can be concluded that the particles with $St_\eta = 19$ are not affected by the additional fluid velocity fluctuations, which is an expected result according to the work of Young and Leeming [116]. Otherwise, the intermediate particle class ($St_\eta = 8$) seems to be sensitive to the sub-grid fluctuations. Nevertheless, it has a negligible effect on the maximum near wall concentration. The influence of the model remains mainly beyond the region of $y^+ < 10$. The sub-grid stress velocity fluctuations are computed dynamically, in a similar way to the sub-grid stress tensor τ_{ij}^{sgs} . The fluid sub-grid stress velocity fluctuations are naturally dumped if the dynamic SMAGORINSKY model is used.

The relation between particle STOKES number and the maximum concentration is further analyzed in Figure 6.16. Two fluid scales are used to define the STOKES number - the KOLMOGOROV and the integral scale of the flow, which leads to St_η and St_l , respectively. The particle concentration is normalized by the corresponding initial uniform concentration value. The available data for the mean particle concentration are extracted from the case with Lycopodium particles. It is evident that the near wall concentration denotes a maximum. The representation of the concentration as a function of the STOKES number based on the integral scale is useful (Figure 6.16(b)). According to this figure, the maximum occurs for $0.5 < St_l < 1$. From this information, it is possible to draw parallels to the work of Marchioli and Soldati [53] and Tang et al. [102]. Both groups consider the large streaky structures near the wall as responsible for the particles to reside in these regions.

6.2 Particle Influence on Turbulence

This chapter provide an analysis of the potential of large-eddy simulation to predict the particle influence on the carrier fluid and on the turbulence characteristics of the fluid, in particular. For this purpose, the results from two-phase LES on the channel flow with 2 and 20 % particle mass loading and a free jet flow with 23 and 86 % loading are presented and discussed.

One focus of the study is the isolated turbulence modification due to particles, where the mean

fluid velocity remains unchanged. This is considered in the context of the high REYNOLDS number channel flow. The second focus is the modulation of the fluid turbulence due to overall change of the fluid momentum due to particles. This is the simpler task for modeling techniques, since the change in fluid mean velocity leads naturally to modification of the turbulence and the direct interaction between turbulent structures and dispersed phase is of less importance. The particle-laden jet provides an opportunity to investigate this issue.

6.2.1 Turbulence Modification at a Constant Mean Flow

A summary of the different cases, used for the comparison, is given in Table 6.2. A more detailed outline of all simulation parameters, together with the boundary and initial conditions, can be found in Tables 4.7 and 4.9 in Section 4.3.2. To obtain reliable results for the carrier

Table 6.2: Channel flow $Re_\tau = 644$: Configurations related to turbulence modification.

Case	Material	Mass loading, %
$d70\phi02$	copper	2
$d70\phi20$	copper	20
$d70\phi20 - e0.5$	copper	20
$d150\phi20$	glass	20

phase from LES employing two-way coupling, it is essential to consider all relevant mechanisms responsible for particular flow patterns of the dispersed phase. In the context of the higher mass loading three issues become more important and are considered as follows:

- As discussed in Section 6.1.1, the particle-wall interaction has an important role for the formation of the particle velocity profiles. The fact that the normal coefficient of restitution, measured for a colliding pair copper-copper is estimated at $e = 0.2$ is related to this. The material of the test section, however, is acrylic glass. There is lack of information concerning copper collision with a partner of different material, though, it is clear that the particle-wall collisions are not elastic and this must be considered.
- The role of a rough wall on the instantaneous particle velocity and on the velocity statistics is addressed in the work of Benson and Eaton [9]. It is a critical issue in a particle-laden channel flows and is discussed based on the results from the $d150\phi20$ case.
- Increasing particle mass loading leads to more inter-particle collisions. These are not explicitly considered in this work, however, their potential influence on the particle motion is discussed at the end of this section.

A numerical experiment is performed to investigate the effect of partially elastic particle-wall collisions on the particle velocity field. The restitution coefficient for particles encountering the wall is set to 0.5. The results from this simulation are compared with those from the simulation assuming ideal elastic particle-wall collisions and with the experimental data from Kulick et al.

[48]. The effect of the inelastic collisions on the particle mean and fluctuating velocity profiles is presented in Figure 6.17. The velocity components and the wall-normal channel coordinate in all plots are normalized using wall units.

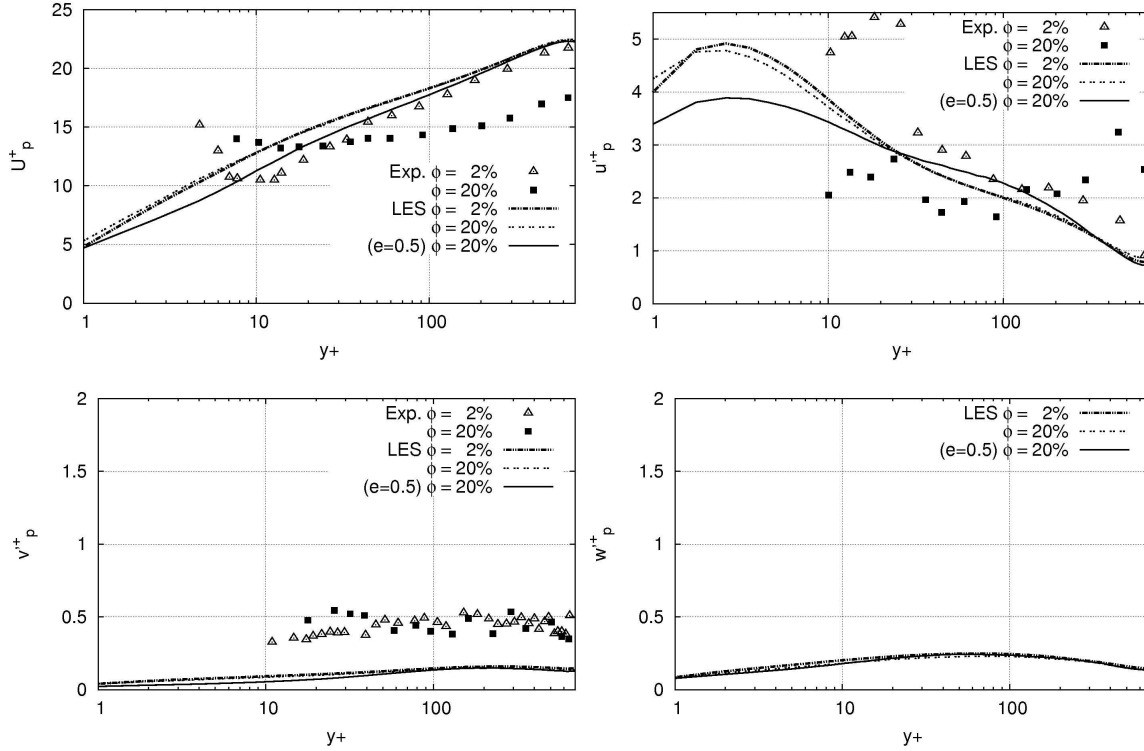


Figure 6.17: Channel flow $Re_\tau = 644$: Dispersed phase mean and fluctuating velocities from simulations with $70 \mu m$ copper particles and different mass loadings, ϕ . Effect of the reduced coefficient of restitution for wall collisions ($e = 1$ and $e = 0.5$) on the particle velocity. Comparison with experimental data from Kulick et al. [48].

The mean particle velocity in the boundary layer region is reduced due to the modified coefficient of restitution. A difference in the axial velocity fluctuations is present throughout the complete cross section of the channel. Very close to the wall, at $y^+ < 30$, the influence is mostly pronounced. The particle spanwise and wall-normal velocity fluctuations are not affected by the new condition. It is apparent that the particle–wall interaction is not the major driver for the development of these velocity fluctuation components. According to the experiment, the mean velocity has a very flat profile, which is exactly opposite to the tendency predicted by the LES with reduced coefficient of restitution. In contrast to this, the streamwise velocity fluctuations are driven into the correct direction for $e = 0.5$, however, the experimental profile is not exactly reproduced. A simulation of the alternative case $d150\phi20$ on the same channel flow configuration is performed to inquire the influence of the particle material on the particle velocity statistics. For this particle class, consisting of glass beads, ideal elastic particle–wall collisions are assumed. This assumption is sufficient in the case of glass beads at low mass loading as shown in Figure 6.3. The particle mass loading and the particle STOKES number for this simulation are retained. Wall-normal profiles of the particle mean and fluctuating velocities are presented together with experimental data from Paris [67] and Benson and Eaton [9] in Figure 6.18. The case simulated here corresponds to the setup from Paris [67]. It is evident that the

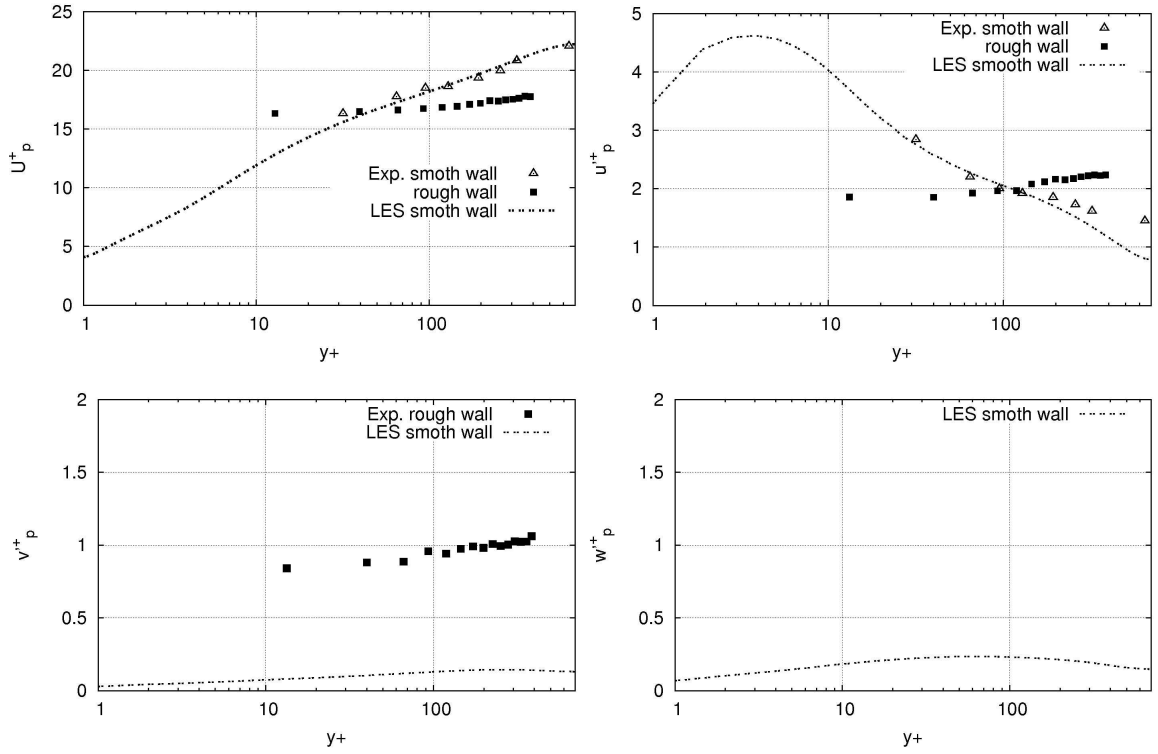


Figure 6.18: Channel flow $Re_\tau = 644$: Dispersed phase mean and fluctuating velocities from simulations with $150\ \mu\text{m}$ glass beads and mass loading $\phi = 20\%$. Effect of the wall roughness on the particle velocity. Comparison with experimental data from Paris [67] and Benson and Eaton [9].

particle velocity profiles do not match the experimental data from Paris [67]. However, the effect on inelastic particle - wall collisions is assumed to be negligible in this simulation because of the coefficient of restitution of glass being close to 1. In addition the plots in Figure 6.18 show data from the experiment of Benson and Eaton [9]. The authors investigated the same particle experimental setup using identical glass beads with $150\ \mu\text{m}$ diameter but lesser mass loading of 15% . The main focus was set on the effect of the wall roughness on the particle velocity properties. The results presented here correspond to the "smooth" wall case from the experiment. It is further important to note that the wall structure of the original development section in the experimental rig, applied in the work of Paris [67], is comparable to the artificial roughness of the wall from the later experiments of Benson and Eaton [9]. The particle velocity components from the present LES are in very good agreement with the particle data from Benson and Eaton [9]. It is possible that for this mass loading the particle volume fraction for the large beads is relatively low and that inter-particle collisions are rare events. It is further evident that for such conditions the particle-wall interaction has a major role for the development of the particle velocity field. The modeling of inter particle collisions constitutes an additional complexity. This phenomenon is not explicitly investigated within the scope of this work, nevertheless, some related findings concerning its relevance in this particular context are reported here. Fevrier et al. [32] and Vance et al. [107] investigated the development of the particle velocity statistics influenced by inter particle collisions using DNS. The authors showed clearly that particle collisions introduce additional dispersion and lead to increased decoupling of the particle from the fluid velocity. This process leads to the flattening of the particle velocity pro-

files and is accompanied by increased fluctuations in the transverse directions (channel flow). Yamamoto et al. [115] presented simulation results from the same channel flow with copper particles, as those presented here. The authors included inter-particle collisions. The relatively uniform profile of the particle mean velocity is well captured in their simulation. The velocity magnitude, however, is significantly overestimated. Additional modeling of the particle-wall interaction is not provided.

The last observation, together with the analysis of the present simulations, lead to the conclusion that an a priori selection of the physical models needed for a particular configuration cannot guarantee reliable results.

Despite the significant deviation of the particle velocity profiles from the experimental data, the question remains unanswered, whether the particle mass loading has an effect on the fluid turbulence. According to the experimental data for case $d70\phi20$, the flow at this mass loading exhibits significant turbulence attenuation. The simulations, though, predict much a lower magnitude of attenuation. Results of the fluid mean and fluctuating velocities related to the present simulations are shown in Figure 6.19. Together with results from the simulations on the $d70\phi20$ and $d70\phi20 - e0.5$ case, data from the LES on the channel with 2 % mass loading are plotted. The experimental measurements are from Kulick et al. [48]. The normalization of the velocity and the spatial coordinate is the same as in Figure 6.17.

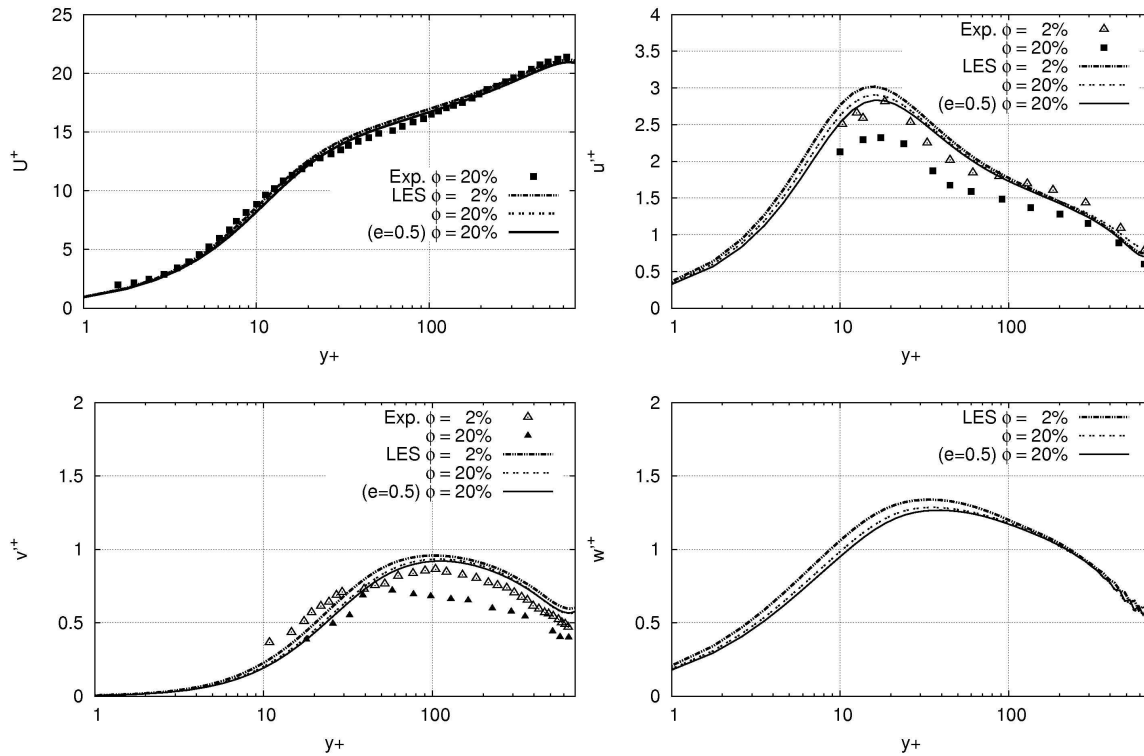


Figure 6.19: Channel flow $Re_\tau = 644$: Gas phase mean and fluctuating velocities from simulations with $70 \mu m$ copper particles and different mass loading ϕ . Comparison with experimental data from Kulick et al. [48].

All simulations satisfy the condition that the gas mean velocity remains unchanged due to the presence of the dispersed phase. Looking at the axial velocity fluctuations, it is obvious that the

simulations with 20 % loading lead to a decrease of the fluid fluctuations. The magnitude of the predicted attenuation at the position of the maximum fluctuations is approximately 50 % less compared to the experimental value. Nevertheless, the position of the maximum at $y^+ \approx 12$ is well captured. The influence on the secondary phase becomes negligible toward the channel centerline, which contradicts the experiment. According to this, the decrease of the fluctuations is almost constant across the channel. The influence on the wall-normal component is also evident but very small. The discrepancy between the simulations and the experiment is much higher for this component. Moreover, the evolution of the profile in the wall-normal direction is not predicted well by the LES. The influence on the spanwise velocity fluctuations seems to be more intensive than this on the wall-normal components, but it is unclear how good the approximation of the real flow is, since no measurements are available. It is evident from the simulation results from the $d70\phi20 - e0.5$ case that the influence of the modified particle-wall interaction on the fluid fluctuations remains quite limited.

The effect of $150 \mu m$ glass beads on the gas phase, as provided by experiment and simulation for the case $d150\phi20$, is presented in Figure 6.20 together with experimental and numerical results from the single phase flow.

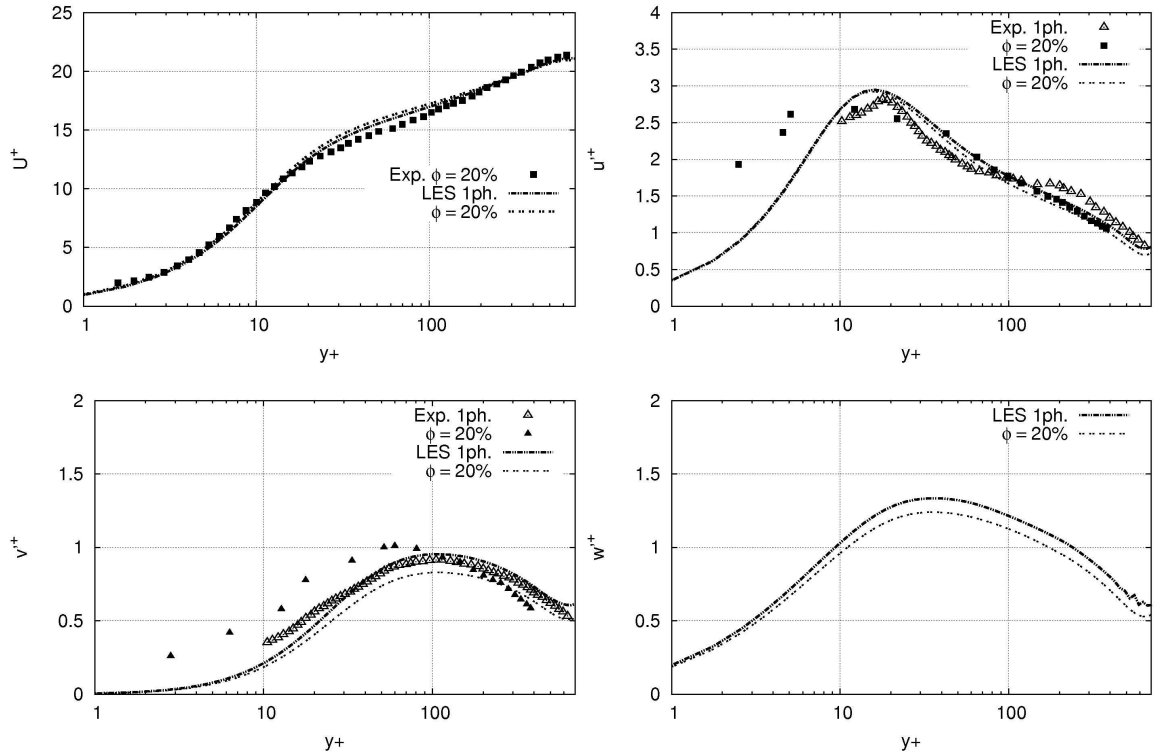


Figure 6.20: Channel flow $Re_\tau = 644$: Gas phase mean and fluctuating velocities from simulations with $150 \mu m$ glass beads and mass loading $\phi = 20\%$. Comparison with experimental data from Paris [67].

The mean velocity is unchanged by the presence of the particles in unison with previous configurations. The axial velocity fluctuations for the single phase and the particle-laden flow in the experiment denote a larger difference for the wall-normal component in the boundary layer region $y^+ < 100$, ([67]). The same component from the simulation is not affected by the particles so close to the wall. The influence of the dispersed phase on the turbulence becomes visible

beyond the boundary layer. The simulation indicates a slight decrease in the axial fluctuations when particles are injected into the flow. The general tendency from the simulation away from the boundary layer is observed in the experiment as well. It is important to remark that Paris [67] applied Particle Image Velocimetry (PIV) for the measurements of this case. The experimental data from Kulick et al. [48], reported above, are obtained using Laser Doppler Anemometry (LDA). Comparison of results from both techniques shows that the velocity characteristics from Paris [67] tend to be higher than the LDA-data, especially in the boundary layer region. The error of the fluctuating velocity is estimated as 8 %. The additional turbulence augmentation estimated for the wall-normal fluctuating component of the particle-laden flow is attested as a possible artefact of the measuring technique in the near wall region. This reasonable suspicion, however, was not proven by additional experiments. The turbulence attenuation outside of the boundary layer is confirmed from both, experiment and simulation.

Concerning the relatively low amount of turbulence attenuation predicted by the simulations in the $d70\phi20$ and $d150\phi20$ cases, it is important to note, that one main feature of the particle velocity field, the mean axial velocity, is not captured well by the simulations. The high relative velocity between both phases contributes significantly for the flow modification. [48] also suggest that the relatively low mean particle velocity is responsible for the significant flow turbulence attenuation underestimation.

6.2.2 Turbulence Modification due to Mean Flow Variation

In this section the prediction of turbulence modification due to overall flow velocity change is studied on the particle-laden free jet flow (Section 4.3) by using two-phase LES. The dispersed phase consists of $80\text{ }\mu\text{m}$ glass beads with a STOKES number, based on the integral time scale at the jet inlet, of $St_l = 41.5$. A main feature of this flow configuration is that the high particle inertia initiates an increase of the carrier fluid mean and fluctuating axial velocity. The flow shows a strong dependency on the particle mass loading. The study here is based on the results from the cases $d80\phi23$ and $d80\phi86$, Table 4.13. Detailed information to the numerical setup is available in Section 4.3.2.

The dispersed phase is initialized at the inlet adopting the instantaneous fluid velocity at the particle position. For case $d80\phi86$, in addition, a correction of the particle initial velocity is made by scaling its magnitude by a factor of 0.75, which is the average of the mean relative velocity between both phases. Though, this rough approximation suits the particle mean velocity profile reasonably well to the experimental measurements. In Figure 6.21 mean and fluctuating velocities of both phases along the jet axis are shown. The axial coordinate is normalized by the jet inlet diameter, the mean fluid and particle velocities are normalized by the jet centerline velocity. The fluctuating velocity is normalized by the mean velocity at the corresponding position. The results for the particle phase in Figure 6.21 suggest the conclusion that both mean and fluctuating particle velocity are well captured by the simulation. Only very close to the jet origin the fluctuating particle velocity exhibits significant deviation from the experimental results. This behavior can be explained by the influence of the inlet boundary conditions. The position of the numerical model is at $-5D$ (according the normalized abscissa). The distance is not sufficient to allow for a fully developed particle flow pattern if the initial guess for the particle velocity at the inlet is very rough as it is for the present case. An extensive discussion on the issue can be found in Section 6.1.1 for the $d80\phi23$ case. Nevertheless the artificial flow

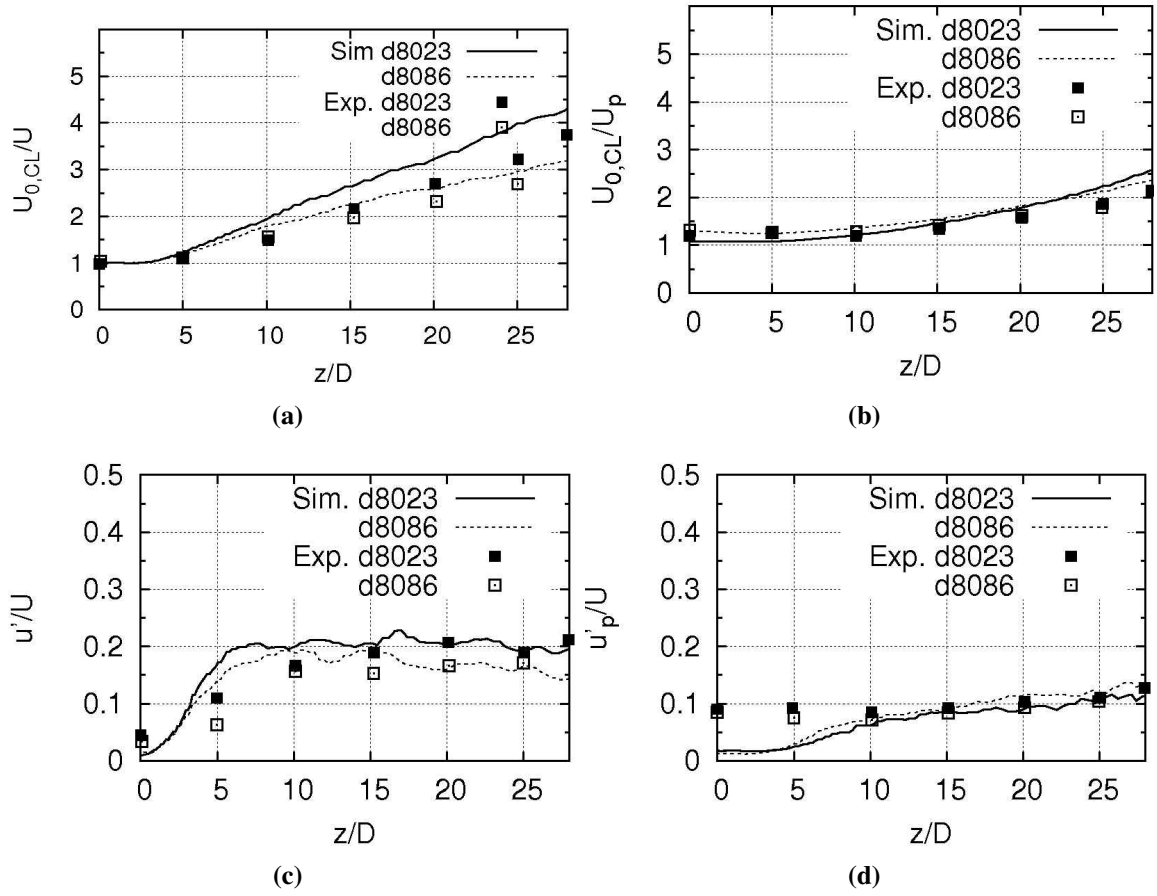


Figure 6.21: Free jet flow $Re_{bulk} = 13000$. Axial mean and fluctuating velocity of the gas (left) and particle (right) phase along the jet axis. $80 \mu m$ particles at 23 % and 86 % mass loading. Comparison with experimental data from Hardalupas et al. [37].

at the jet origin does not affect the particle velocity further downstream because of the strong interaction between gas flow turbulence and particle motion. A common feature of both setups is the nearly similar order of magnitude of particle mean and fluctuating velocity.

The simulation results for the gas phase on the other hand do not allow for a clear interpretation. The flow with the high particle mass loading, $d80\phi86$, is reasonably reproduced by the LES in terms of mean velocity. The simulation results of the low mass loading flow, $d80\phi23$, predict significantly stronger velocity decay along the jet axis than the measured value. Since the only difference in the simulation setup is the injected particle mass, the obvious explanation for the different results is namely the mass loading. It is essential for both setups that the particle volume fraction is above the value of $1e-4$. I.e., accordingly the classification in [16] in both cases a strong influence of the dispersed phase on the gas flow is expected. Similar behaviour of the gas phase is observed in the experiments too. Therefore, it remains an open question, what is the reason for the weak fluid–particle interaction in the $d80\phi23$ -case LES?

Considering the gas fluctuating velocity in Figure 6.21 the simulation results confirm the experimental findings that the higher the particle mass flow rate the lower the fluid velocity fluctuations. Nevertheless, this is an expected result: the particle phase, having higher concentration, accelerates due to drag more effectively the gas phase, which means that the gas mean velocity

increases. Consequently for continuity reasons a decrease of the fluid turbulence occurs. The quantitative prediction of the gas velocity fluctuations remains rather challenging for the LES. Both simulations denote significant overprediction of the fluctuations for $x/D < 10$. For the relatively high particle concentration occurs between fluid and particles very intensive momentum transfer, which is resolved by the simulation as well. The main difference between experiment and simulation emerges from the state of the two-phase flow at the jet origin: As noted above due to the relatively short development section in the numerical model the two-phase flow is still developing. In the experiment on the contrary the measurements are performed on a jet starting from a fully developed two-phase flow in a pipe, Section 4.3.1. The high sensitivity of LES even for single phase round jet flow is widely discussed in the literature, [113].

The analysis of the present simulations leads to the conclusion that initial conditions in a numerical model for the dispersed phase play a major role for the overall reliability of a two-phase flow prediction. The numerical simulation of the preliminary section as a setup of two-phase flow in a periodic pipe represents a possible remedy. The result will provide an instantaneous inlet conditions for the two-phase flow.

Figure 6.22 presents radial profiles of the particle mean velocity and the particle axial velocity fluctuations. The spreading rate of the simulated particle jets differs significantly between the

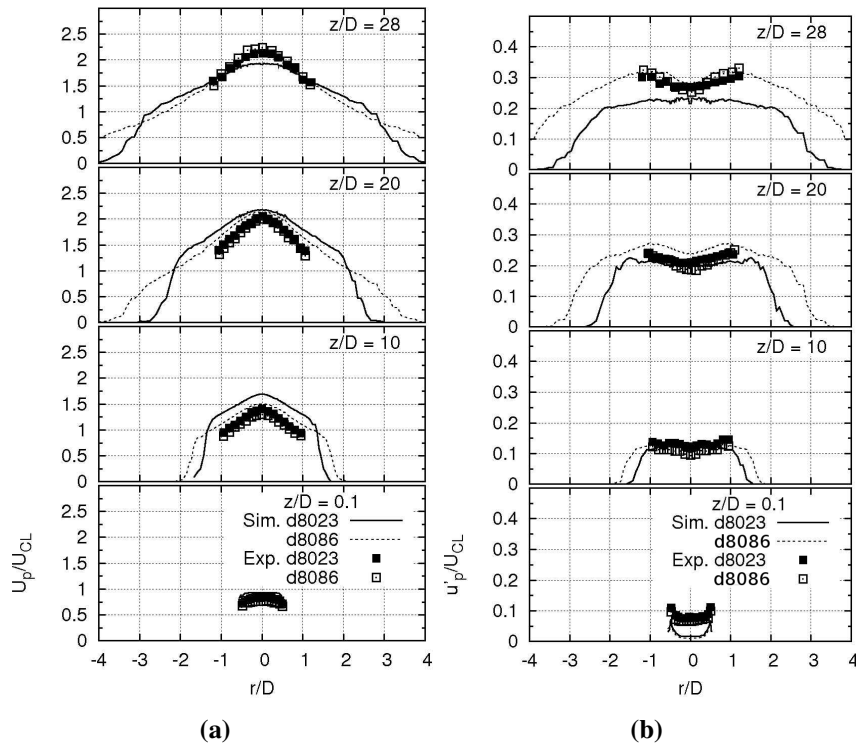


Figure 6.22: Free jet flow $Re_{bulk} = 13000$. Radial profiles of axial mean (left) and fluctuating (right) velocity of the dispersed phase at four axial positions (jet inlet at $x/D = 0$). $80 \mu m$ particles at 23 % and 86 % mass loading. Comparison with experimental data from Hardalupas et al. [37].

cases $d80\phi23$ and $d80\phi86$. The simulated particle mean axial velocity corresponding to the low mass loading flow, decelerates faster downstream than the one in the experiment. Considering the high STOKES number ($St_l = 41$) of the dispersed phase, the impact of the carrier fluid on the particle velocity fluctuation is expected to be weak.

In contrast to the low mass loading case, the particle mean velocity from the 86 % mass loading simulation matches the experimental data well. Based on the computed data for the axial velocity fluctuations of the particles in the case $d80\phi23$, it is evident that a discrepancy between simulation and experiment exists for the axial position $x/D = 28$. In contrast to this, the particle fluctuations for the case $d80\phi86$ are captured very well. This observation can be explained with the positive (in terms of prediction reliability) influence of the high mass loading on the evolution of the particle velocity field.

Nevertheless, the question about the less accurate prediction of the particle velocity for the lower mass loading remains unanswered. There are different conceivable resolutions: errors in the statistical evaluation, insufficient number of samples or neglected relevant physical forces. According to Elghobashi and Truesdell [26] the most important forces acting on heavy, small particles are the drag and the gravitational force, since they prevail with several orders of magnitude over all other forces. Taking into account that the discrepancy between experiment and simulation occurs for $x/D > 25$, as well as the small particle diameter and their high density, it can be assumed that the lift force due to high gradients of the mean particle velocity is negligible. The samples for the dispersed phase have been found to be sufficient, as it is evident from the statistical properties. The statistical evaluation of discrete phase properties is performed in the same generic way as for the carrier phase. However, it is necessary to assess this assumption. This configuration is meshed using a so called *cooper* meshing algorithm. The basic idea of this method is to generate hexahedron meshes by sweeping a surface mesh along a predefined direction. For the present case this is the axial direction. To reduce the number of cells it is a common practice to coarsen the grid in less relevant regions. The coarsening for the jet domain is applied in radial and axial directions. Consequently, the hexahedron cells in the core region (around the jet axis) further downstream are elongated. The face area with a normal vector orthogonal to the axial coordinate is much larger than the area with a normal vector coaxial to the jet axis. Consequently, the probability for a particle to cross the cell in radial direction is much higher than this for axial direction crossing. Therefore, the axial velocity computed from this events is lower.

Within the scope of this investigations, the hypothesis is not proven by additional simulations and it should be considered as a topic for further investigations. The issue will be more pronounced for complex geometries, where the numerical grid quality can not be guaranteed for the whole domain.

The evaluation of the fluid properties is shown in Figure 6.23. The radial profiles of the gas phase velocity are plotted for the single phase and both particle-laden configurations. The comparison with the experiment, except for the single phase flow, is restricted to two axial positions at $x/D = 0.1$ and $x/D = 28$, since no further experimental data are provided. The velocity profiles of the flow, with and without, particles is well captured by the simulations. From the numerical results it is apparent that the acceleration of the mean gas velocity in both simulations precedes this of the velocity fluctuations and is detected first at $x/D = 10$. An increase of the axial fluid fluctuations is captured at $x/D = 20$. One mechanism for the turbulence augmentation is hence the higher mean velocity gradient in the fluid induced by the particles. The anticipated effect of the particles on the gas phase can be approximated from the ratio of particle diameter to flow integral length scale, which is estimated as $d_p/l_f \approx 0.1$ at the jet inlet. The TAYLOR hypothesis is applied for the estimation of the fluid length scale. According to the classification proposed by Crowe [17], the ratio indicates that the particles possibly do not

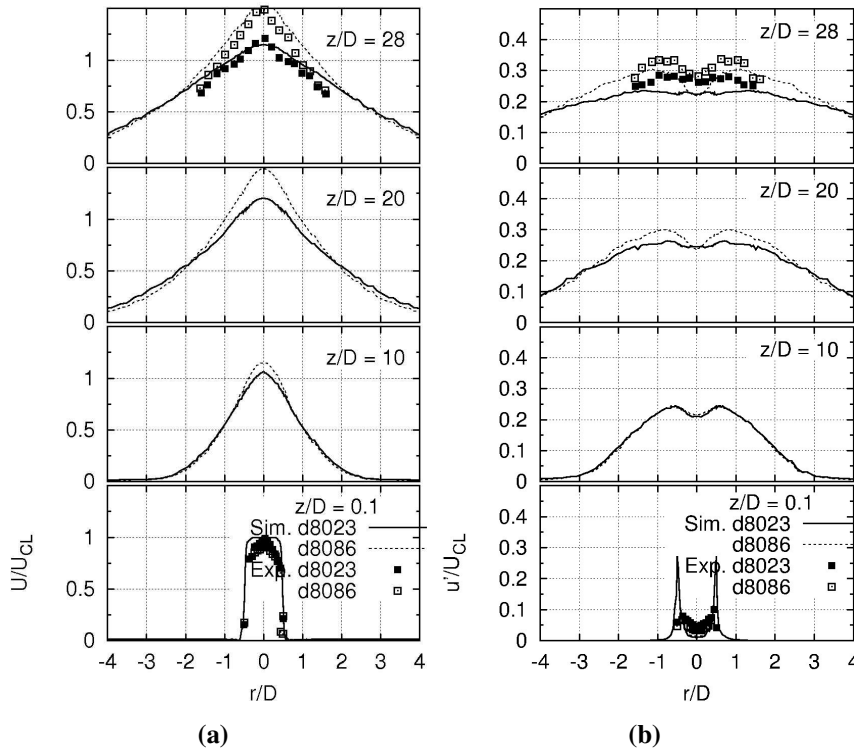


Figure 6.23: Free jet flow $Re_{bulk} = 13000$. Radial profiles of axial mean (left) and fluctuating (right) velocity of the gas phase at four axial positions (jet inlet at $x/D = 0$). The gas flow is laden with $80 \mu m$ particles at 23 % and 86 % mass loading. Comparison with experimental data from Hardalupas et al. [37].

contribute for any turbulence modification. The fluid length scale varies along the jet axis and the local conditions seen by the particles could change. An effective contribution, however, is possible only in the form of turbulence attenuation, since the wake effect induced by large particles must be explicitly modeled.

Considering the possible error sources discussed above, it can be concluded that for jet-type flows realistic inlet conditions for the dispersed phase are essential for the reliability of the simulation close to the jet inlet. Furthermore, explicit consideration of a part of the flow supply section does not guarantee realistic turbulence properties and dispersed phase statistics. Nevertheless, the effect of the turbulence augmentation is well captured, since it occurs further downstream, where the fluid and particle velocities are already uncorrelated to the inlet conditions. The effect of the grid quality on the evaluation of the dispersed phase statistical properties needs to be investigated closely. In general, higher particle mass loadings reduce the effect of the non-conformal mesh due to the higher rate of sampling events.

6.3 Evaporating Spray in a Confined Circular Chamber

The configuration of an evaporating non-reacting spray from Sommerfeld and Qiu [99] exhibits several features, which make it favorable for investigation using LES. The system is operated at standard conditions and no special treatment is required for the boundary conditions. There is a

detailed database on the dispersed phase properties, containing diameter distributions, velocity-diameter correlations and droplet mass flux. The data is collected at a position, which allows for using the dilute spray approximation. Additional breakup and coalescence are assumed to be of lesser importance. The operating temperature is quite low and equilibrium evaporation models are sufficient to capture the process of mass transfer from the droplets to the surrounding ambience.

6.3.1 Previous Large-Eddy Simulations

Moin and Apte [61] and James et al. [41] reported of LES on the configuration from Sommerfeld and Qiu [99] as a part from other spray related investigations. Apte et al. [4] proposed recently a high fidelity two-phase LES on this configuration. The dispersed phase is computed in LAGRANGIAN frame. The simulation is performed using an unstructured code. In this work, special attention is set on the adjustment of the gas phase inlet conditions as well as on the mesh quality in the region around the droplet injection as well as on the near wall resolution. The detailed data provided by the experimental database are applied for the spray inlet injection, which makes the explicit simulation of the nozzle and the primary droplet breakup processes obsolete. The number of the tracked particles in statistically steady state approximates $1 \cdot 10^6$. The computational domain is extended to prevent negative influence of the outlet boundary condition. On the modeling side, the droplet evaporation is approximated using an "uniform-state" equilibrium model ([27], [92]). The effects of the unresolved turbulent scales on the filtered mass fraction and temperature are considered using a correlation of the filtered mixture fraction and its variance based on the presumed PDF approach. The mixture fraction variance is obtained by applying a dynamic procedure, as suggested by Pierce and Moin [71]. The model assumes that the evaporation time scale is smaller than the mixing time scale. The simulation results match the experimental results very well in terms of mean and fluctuating velocities of both phases. In addition, mean and *RMS* values of the droplet diameter are presented together with the liquid mass flow rate.

Hahn et al. [36] applies an EULERIAN-LAGRANGIAN approach in the context of LES to simulate the same configuration. The authors employ a structured, multi-block and body fitted grid code, involving a search free particle tracing algorithm for their simulations. Boundary and initial conditions are similar to those imposed by Apte et al. [4]. Droplet evaporation is captured, again, by an uniform state equilibrium model. Here, the effect of the sub-grid stress mixing processes on the evolution of the vapor mass fraction and the temperature is omitted. The quality of the results reported by Hahn et al. [36] is reasonable, while the number of the droplets tracked is only approximately 1/5 of this computed in Apte et al. [4].

For both simulations, [36] and [4], there is no information, concerning the number of samples collected for the dispersed phase during the calculations.

6.3.2 Present Results

A brief summary of the setup used for the LES simulations here is presented to highlight similarities and differences to the numerical setups adopted by Hahn et al. [36] and Apte et al. [4]. The present simulations are carried out employing an unstructured grid CFD method utilizing an efficient particle search algorithm. The equations for the gas phase are solved applying an

efficient non-iterative Fractional Step time marching algorithm for the pressure-velocity coupling. The method is successfully validated for single phase flows with constant flow properties (Kim and Makarov [43]). The inlet boundary conditions for the dispersed phase are applied as reported by Sommerfeld and Qiu [99]. The total number of particles, tracked in the steady state flow, is approximately $3.7 \cdot 10^6$. The significant difference to the above reported simulations is assumed to result from the minimum droplet diameter considered in the simulation. The filtered fluid velocity is considered in the drag term of the droplet equation of motion. All details of the numerical setup can be found in Section 4.4.

6.3.2.1 Statistical Properties of the Gas Phase

Results from the single and two-phase simulations of the gas phase are presented together in the following section. The experimental data corresponds to single phase flow measurements, since due to a limitation of the available measurement technique, it was impossible to discern between tracer particles and small droplets under evaporating spray conditions. In Figure 6.24 radial plots of the axial mean and fluctuating velocities and the mean radial velocity of the gas at seven axial positions are presented. The comparison between unladen and laden flow shows that

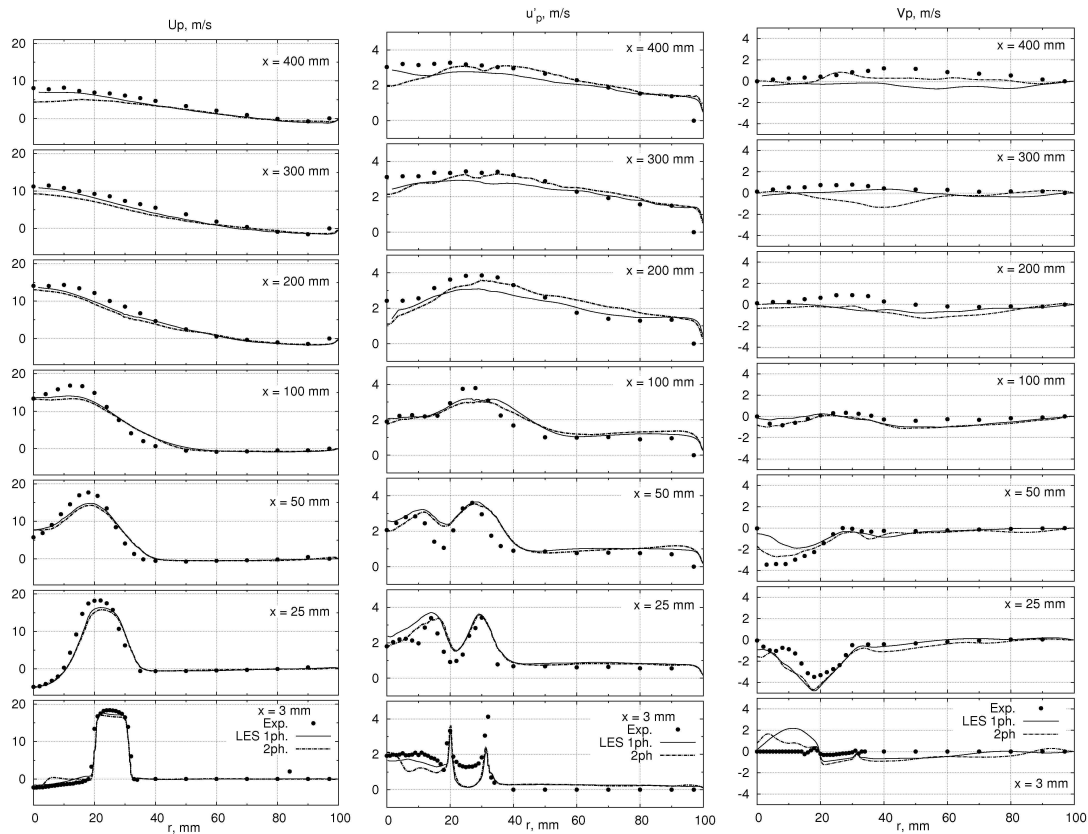


Figure 6.24: Evaporating spray in circular chamber. Gas phase mean and fluctuating axial velocities and mean radial velocity from simulations of single and two-phase flows. Comparison with experimental data from Sommerfeld and Qiu [99].

the influence of the particles on the fluid velocity remains negligible for all velocity components

investigated. The fluctuating velocities in axial and radial directions demonstrate a more evident discrepancy between computational and experimental data in the first measurement plane at 3 mm . The underestimation of the axial fluctuations by the simulation close behind the annular inlet of the hot air is a consequence of the air inlet boundary condition. This does not have a long-distance influence on the component as evident in the next measurement plane at 25 mm . The high radial fluctuations in the first plane (3 mm) are assumed to be a effect of the wall boundary condition defined behind the spray injection. At this position in the experimental rig, the cavity where the hollow cone injector for the spray supply is mounted, ends. It is evident from the mean axial component up to position $x = 25 \text{ mm}$ that the core flow ($r < 10 \text{ mm}$) denotes a recirculation zone. The wall at position $x = 0 \text{ mm}$ forces the flow in radial direction and induces a higher radial velocity.

6.3.2.2 Statistical Properties of the Dispersed Phase

The injection position for the dispersed phase is set to the axial position of 3 mm , according to the experiment. The inlet is represented by ten annular arranged surfaces with the corresponding droplet diameter and velocity distribution. In Figure 4.8 a sketch of the inlet part for the droplets is shown. Due to droplet vaporization and the finite radial dispersion, the number of droplet samples is reduced in radial and axial direction with increasing distance from the injection. The minimum number of samples used for data evaluation is 2000.

Simulation results for the droplet mean and fluctuating axial velocities are shown in Figure 6.25. The data is averaged for all available droplets at the particular position (control volume). The mean axial velocities of the droplets are very well captured by the simulation. The sim-

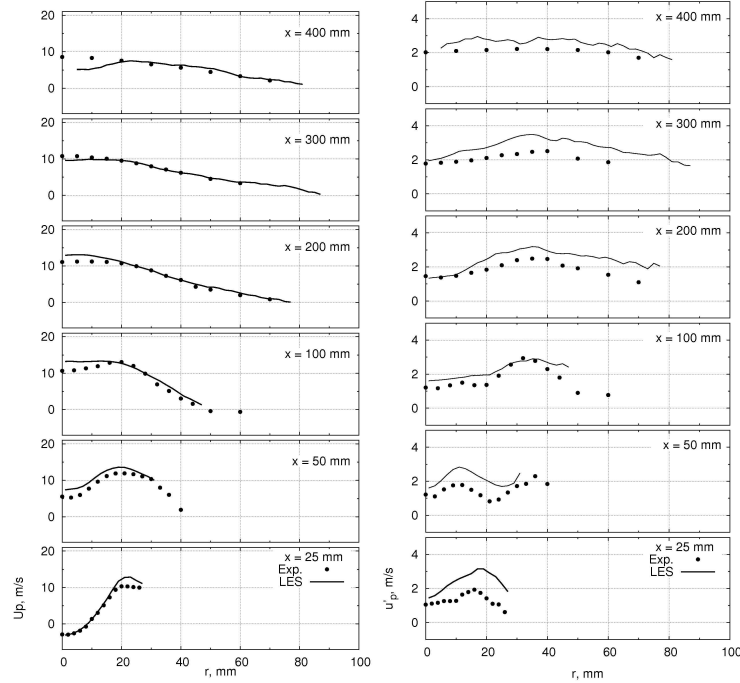


Figure 6.25: Evaporating spray in circular chamber. Liquid phase mean and fluctuating axial velocities compared with experimental data from Sommerfeld and Qiu [99].

ulated profiles, corresponding to the droplet axial velocity fluctuations, at the first and second axial positions overestimate the experiments slightly. Since the average number of samples at these axial positions is always above 10000, statistical errors due to insufficient sampling are assumed to be negligible. It is worthwhile to mention that all droplets detected in the domain are included into the statistical evaluation. A significant amount of them have a diameter below $3 \mu\text{m}$, which is the lower cut-off droplet diameter detectable by the measurement technique. The small droplets behave like the fluid tracer. Their velocity is highly correlated with the fluid velocity fluctuations, which are higher than those measured for the dispersed phase. Since the estimation of the droplet velocity statistics over all droplets does not consider the droplet diameter, it leads to an overestimation of the droplet axial velocity fluctuations. This effect is further amplified due to the recirculation zone in this region. The effect vanishes downstream from the third measurement plane, which is downstream of the recirculation zone.

The effect of the smaller droplets is quite evident from the plots for the droplet mean diam-

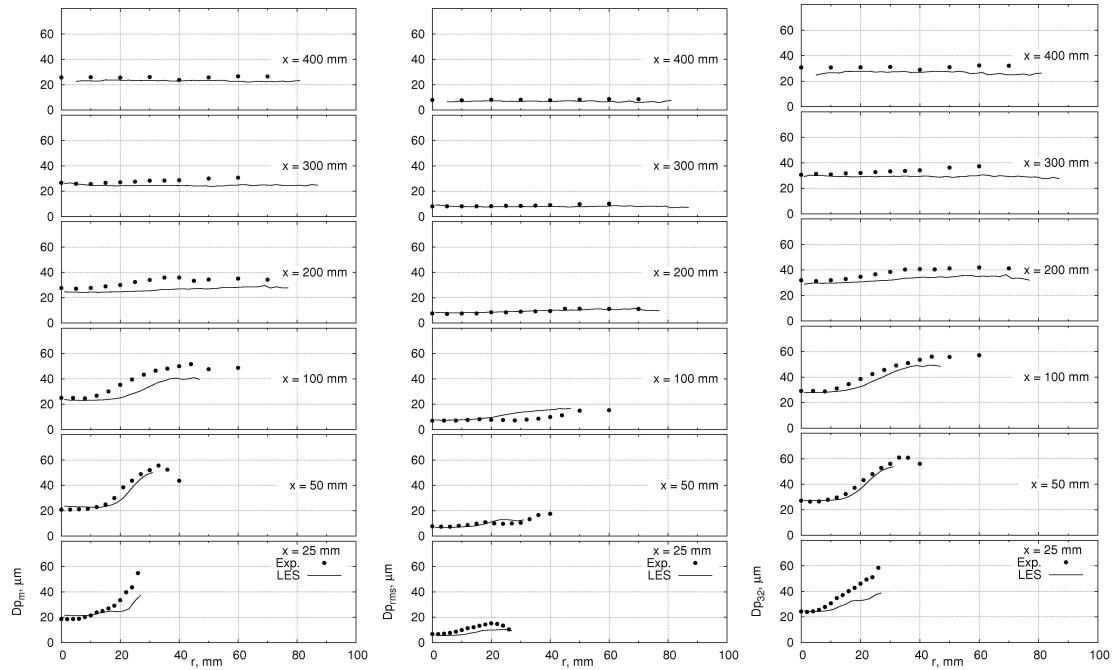


Figure 6.26: Evaporating spray in circular chamber. Liquid phase mean, *rms* and SAUTER mean diameter compared with experimental data from Sommerfeld and Qiu [99].

eter, shown in Figure 6.26. The figure includes also data for the droplet *rms* diameter and the SAUTER mean diameter, d_{32} . The plots confirm the very good prediction of the particle diameter statistics.

Another aspect concerning the reliability of the simulation is the chosen evaporation model. As primarily assumed, an equilibrium model will resolve adequately the evaporation process for the given operating conditions. In order to investigate this in Figure 6.27 are presented fluid and droplet temperature plots extracted from the simulation results. An additional difficulty for such assessment arises from the incomplete data for characterization of the thermodynamic state of the phases. The experimental investigations for the dispersed phase are restricted to velocity and diameter properties. Nevertheless, the investigation of the simulation results will

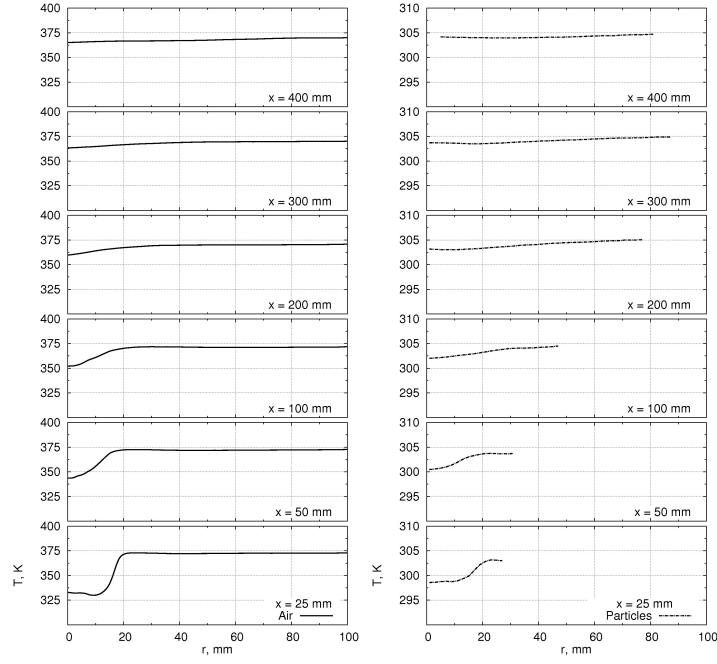


Figure 6.27: Evaporating spray in circular chamber. Radial profiles of the mean temperature of the gas and the liquid phase from the simulation at different axial positions.

give up to certain amount an insight into the evaporation process.

The reader shall consider that the scaling of the ordinate, the temperature axis, of both plots in Figure 6.27 is different. In general the gas temperature leads the droplet temperature for all shown axial positions. The significant temperature drop up to axial position $x = 100 \text{ mm}$ within the regions with high droplet concentration is an natural result of the energy transport toward the colder droplets. More interesting is the accurate tendency prediction of the droplet temperature, i.e. during the evaporation droplets become colder. To remind the reader, the inlet temperature for the liquid phase is 307 K . Very intensive cooling experience the droplets in the region close to the nozzle. Since the gas phase gets colder due to the droplet heating, the thermodynamic state of the droplets changes and following in order to achieve an equilibrium state their temperature decreases. Further downstream the large amount of small droplets is already evaporated and the droplet concentration is therefore significantly reduced. The energy transport from the hot gas to the droplet much lower. The cooling of the liquid phase is not observed.

Looking at the last simulated configuration, it can be concluded that the applied non-iterative Fractional Step method allows for reliable prediction of flows involving two-way coupling for momentum and mass transfer, when moderate variations of the fluid properties are taken into account. Its application to combustion systems needs, however, further validation work. As discussed in previous sections (6.1.1, 6.1.2), the LES provides a reliable prediction of the velocity field for the dispersed phase. The statement can be extended for the prediction of evaporation processes with relatively low rates of mass transfer as well. However, for configurations with high evaporation rates, Masoudi and Sirignano [57] have shown that the interaction between the sub-grid scales and the droplets can lead to modification of the SHERWOOD and NUSSELT numbers. More sophisticated models are required.

7 Conclusion

A systematic analysis of dilute dispersed two-phase flows using LES is presented in this work. The focus of this study is on the reliability of the simulations, which are performed in the context of EULERIAN-LAGRANGIAN approach. Conclusions, based on results from simulations are compared with findings from DNS and experimental investigations of other authors. Since many of the reference findings are mostly derived from a specific setup (numerical or experimental), it is investigated whether they are valid when applied to different flow configurations. Special attention is paid to the identification of weak spots in the EULERIAN-LAGRANGIAN method. The lack of physical models, critical numerical issues and possible invalid interpretations of the results are discussed.

The study builds on results from four configurations. Two plane, particle-laden channel flows with different shear REYNOLDS numbers ($Re_\tau = 150$ and $Re_\tau = 644$) and hence with a different ratio of integral to KOLMOGOROV time scales, $t_l/\tau_\eta = 6$ and $t_l/\tau_\eta = 22$, are computed. Eight particle types, classified on their STOKES number in the range of $St_\eta = \{0.08 \dots 19\}$, are used for the analysis. In addition, a particle-laden jet flow and an evaporating spray in a coaxial chamber are applied within this scope. A tool for in-situ and posteriori data analysis is developed to obtain the statistical properties of the dispersed phase. The coupling of the *non-iterative Fractional Step Method* in the context of unstructured and non-orthogonal meshes, using a second order implicit temporal integration scheme, to LAGRANGIAN particle tracking, including bidirectional interaction between dispersed and continuous phase, is developed and validated within this work.

One major issue of the work is the reliable prediction of particle preferential accumulation and turbulent dispersion. This focus arises from its essential influence on the prediction of ongoing mixing and chemical reaction processes, such as in spray combustion devices. A second emphasis is the flow turbulence modification due to small heavy particles. Two alternative generation mechanisms are investigated: first, the direct influence on turbulent statistics and second, turbulence modification induced by overall momentum change in the fluid due to particles.

The results for local particle accumulation and dispersion can be summarized as follows:

- Using LES to describe the carrier fluid motion explicitly implies that phenomena such as local particle accumulation around large turbulent scales become partially resolved. The level of particle preferential accumulation is investigated in the context of two channel flow configurations. The difference in the standard deviations of the computed number density PDFs and a POISSON distribution presents a parameter for characterization of the preferential accumulation. For the high REYNOLDS number flow the LES is able to reproduce a maximum accumulation for particles with $St_\eta \approx 2$ which is observed in the experiments from Fessler et al. [31]. Moreover, it was possible within the scope of this work to show that this behavior applies for low REYNOLDS number flow as well. The STOKES number exhibiting maximal accumulation contradicts previous findings on particle accumulation in the DNS context ([100], [111]). The authors, however, did not

consider different length scales at which preferential accumulation might possibly occur. In the present work it is evident that the scale of maximum accumulation increases proportional to the St_η . An additional dependency of the magnitude of accumulation on the flow REYNOLDS number is demonstrated by comparing both channel flows. A lower turbulence intensity induces higher levels of particle preferential accumulation.

- A stochastic model accounting for sub-grid stress induced particle dispersion is investigated in the context of the high REYNOLDS number channel flow. It is based on the eddy-life / eddy-crossing time hypothesis. The model leads to a significant decrease in particle accumulation. The main issue detected here is that the model constant seems to be case dependent, since the amount of the unresolved kinetic energy is not apriori fixed in the context of LES, as in the case of turbulent models based on statistical averaging. However, the applied stochastic model does not affect the velocity field statistics (mean and rms) of the dispersed phase.

Following the resulting local particle number density field due to accumulation, it is further apparent that the need for a collisional model in LES context is explicit, even for very low particle mass loading. Considering particle collision will further increase the dispersion of solid particles in a natural way. For liquid particles (droplets) additional physical phenomena such as coalescence must be included in the collision model as well.

The generation of turbulence modification due to small heavy particles is investigated from two perspectives.

- The direct influence of the dispersed phase on the turbulent properties on the high REYNOLDS number channel flow is studied. According to the simulation results, the effect on the turbulence attenuation is apparent only in the region with maximum fluid velocity fluctuations ($5 < y^+ < 50$). The relatively low magnitude of turbulence modification, compared to the experiments from Kulick et al. [48] and Paris [67], is found to be a consequence of the deficit in the prediction of the particle velocities. This deviation is attributed to the lack of an appropriate particle-wall interaction model. To better understand the variety of mechanisms additional detailed experimental investigations on particle-fluid velocity correlations and on the velocity distribution function would be of great support.
- The simulation results from the particle-laden jet flow case with 23 % and 86 % particle mass loading lead to the conclusion that the fluid mean and fluctuating velocities are reasonably well predicted, however, the results corresponding to the high mass loading case are closer to the experimental observation. This tendency is assumed to be a consequence of the inlet boundary conditions adopted for the dispersed phase. This issue appears to be essential for the prediction of the velocity field at moderate mass loading. Nevertheless, the effect of the inlet conditions is not a specific LES issue.

The simulation of a circular chamber with evaporating isopropyl alcohol spray is dedicated to the validation of the chosen numerical method. The latter represents in the scope of multiphase flow LES an effective alternative to standard SIMPLE-like methods regarding highly time consuming computations. This is a combination of a non-iterative time advancement method for the continuous phase accounting for two-way coupling with the discrete phase. The challenge

of the certain configurations arises from the variable continuous phase density. The numerical method is developed primary for flows with constant fluid properties (density and viscosity). The detailed inlet conditions for the dispersed phase, provided by the experiments of Sommerfeld and Qiu [99], are used for this setup. The numerical results have very good agreement with the experimental data for air and droplet mean and fluctuating velocities, as well as droplet diameter statistics. The vital importance of appropriate inlet conditions for the dispersed phase becomes evident. It is expected for this configuration that the droplets exhibit preferential accumulation, however, it is not possible to perform a comparison with experimental data, because this is not provided.

Analysis of the particle velocity statistics leads to the conclusion, common for all cases, that a realistic particle–wall interaction model will improve the prediction of velocity statistics of heavy particles utilizing LES.

It is also important to consider the effect of unstructured and non-conformal meshes on the statistical evaluation of the dispersed phase properties, such as velocity or concentration. Unlike the experimental measurement volume, the computational cells, for which the particle statistics are collected, vary. The negative effect of non-conformal mesh on the statistics is expected to increase for tetrahedron meshes.

From the summary of the simulations it is apparent that the EULERIAN-LAGRANGIAN approach exhibits several deficiencies in the context of LES. These need to be overcome to extract reliable informations from future simulations. The inclusion of an inter-particle collision model is a desirable alternative to tuning an advanced stochastic dispersion model to a specific experiment in order to match the stochastic PDF. For simulations where the particle–wall interaction is important, the effect of rough wall on the particle motion is essential and needs modeling. In addition, numerical grids with good cell quality are essential for reliable statistical properties for the dispersed phase.

Bibliography

- [1] AGARD. *A Selection of Test Cases for the Validation of Large-Eddy Simulations of Turbulent Flows*. Agard Advisory Report 345, Neuilly-Sur-Seine, France, 1998.
- [2] ANSYS FLUENT 12.0 Documentation. ANSYS Inc., 2009.
- [3] S. V. Apte, K. Mahesh, P. Moin, and J. C. Oefelein. Large-eddy simulation of swirling particle-laden flows in a coaxial-jet combustor. *Int. J. Multiphase Flow*, 29:1311–1331, 2003.
- [4] S. V. Apte, K. Mahesh, and P. Moin. Large-eddy simulation of evaporating spray in a coaxial combustor. *Proc. Comb. Inst.*, 32:2247–2256, 2009.
- [5] V. Armenio, U. Piomelli, and V. Fiorotto. Effect of the subgrid scales on particle motion. *Phys. Fluids*, 11:3030–3042, 1999.
- [6] S. Armsfield and R. Street. The Fractional Step method for the Navier-Stokes equations on staggered grids: Accuracy of three variations. *J. Comp. Phys.*, 153:660–665, 1999.
- [7] J. Axerio and G. Iaccarino. Flow asymmetry and vortical structures behind a rotating tire. *Bull. American Phys. Soc.*, 54, 2009.
- [8] T. J. Barth and D. Jespersen. The design and application of upwind schemes on unstructured meshes. Technical Report AIAA-89-0366, AIAA 27th Aerospace Science Meeting, Reno, Nevada, 1989.
- [9] M. J. Benson and J. K. Eaton. The effects of wall roughness on the particle velocity field in fully developed channel flow. *Report No. TSD-150*, 2003. Thermosciences Division, Stanford University.
- [10] M. Boileau, S. Pascaud, E. Riber, B. Cuenot, L.Y.M. Gicquel, T.J. Poinso, and M. Cazals. Investigation of two-fluid method for large eddy simulation of spray combustion in gas turbines. *Flow Turb. Comb.*, 80:291–321, 2008.
- [11] E. J. Boyle and M. Massoudi. A theory for granular materials exhibiting normal stress effects based on enskog’s dense gas theory. *Int. J. Eng. Sci.*, 28:1261–1275, 1990.
- [12] T. M. Burton and J. K. Eaton. Fully resolved simulations of particle-turbulence interaction. *J. Fluid Mech.*, 545:67–111, 2005.
- [13] N. Caraman, J. Boree, and O. Simonin. Effect of collisions on the dispersed phase fluctuations in a dilute tube flow: Experimental and theoretical analysis. *Phys. Fluids*, 15: 3602–3612, 2003.

- [14] I. Celik, M. Klein, M. Freitag, and J. Janicka. Assessment measures for urans/des/les: An overview with applications. *J. Turb.*, 7(48), January 2006.
- [15] A. Clamen and W. H. Gauvin. Effects of turbulence on the drag coefficients of spheres in a supercritical flow regime. *AIChE J.*, 15:184, 1961.
- [16] C. Crowe, M. Sommerfeld, and Y. Tsuji. *Multiphase Flows with Droplets and Particles*. CRC Press, Boca Raton, 1998.
- [17] C. T. Crowe. Modeling turbulence in multiphase flows. *Eng. Turb. Mod. Exp.*, 2:899–913, 1993.
- [18] T. E. Daubert and R. P. Danner. Data compilation tables of properties of pure compounds. Technical report, Design Institute for Physical Property Data. New York: AIChE, 1987.
- [19] S. C. R. Dennis, S. N. Singh, and D. B. Ingham. The steady flow due to a rotating sphere at low and moderate reynolds numbers. *J. Fluid Mech.*, 101:257–279, 1980.
- [20] E. Deutsch and O. Simonin. Large eddy simulation applied to the motion of particles in stationary homogeneous fluid turbulence. *Turbulence Modification in Multiphase Flows*, ASME, 110:35–42, 1991.
- [21] D. Dimitrova and A. Sadiki. Numerical study of bubbling fluidized bed using a kinetic theory for granular materials including normal stress effects. In *Proc. 6th Int. Conf. on CFD in Oil & Gas, Metallurgical and Process Industries SINTEF/NTNU, Trondheim, Norway, 10-12 June, CFD08-081*, 2008.
- [22] D. Dimitrova and A. Sadiki. Analysis of dense two-phase flows based on an eulerian-lagrangian approach using four-way-coupling. In *Proc. of the 7th Int. ERCOFTAG Symp. on Eng. Turbulence Modelling and Measurements, Limassol, Cyprus*, 2008.
- [23] J. Ding and D. Gidaspow. A bubbling fluidization model using kinetic theory of granular flow. *AIChE Journal*, 36:523–538, 1990.
- [24] D. A. Drew and S. L. Passman. *Theory of Multicomponent Fluids*. Springer Verlag, New York, 1999.
- [25] EACC. *European Automotive CFD Conf.* 2007. URL <http://www.eacc.fluent.com/papers.html>.
- [26] S. Elghobashi and G. C. Truesdell. Direct simulation of particle dispersion in a decaying isotropic turbulence. *J. Fluid Mech.*, 242:655–700, 1992.
- [27] G. Faeth. *Prog. Energy Combust. Sci.*, 9:1–76, 1998.
- [28] P. Fede and O. Simonin. Numerical study of the subgrid turbulence effects on the statistics of heavy colliding particles. *Phys. Fluids*, 18:045103, 2006.
- [29] J. H. Ferziger and M. Peric. *Computational Methods for Fluid Mechanics*. Springer Verlag, 3 edition, 2002.

-
- [30] J. R. Fessler and J. K. Eaton. Turbulence modification by particles in a backward-facing step flow. *J. Fluid Mech.*, 394:97–117, 1999.
- [31] J. R. Fessler, J. D. Kulick, and J. K. Eaton. Preferential concentration of heavy particles in a turbulent channel flow. *Phys. Fluids*, 6:3742–3749, 1994.
- [32] P. Fevrier, O. Simonin, and K. D. Squires. Partitioning of particle velocities in gas-solid turbulent flows into a continuous field and a spatially uncorrelated random distribution: Theoretical formalism and numerical study. *J. Fluid Mech.*, 533:1–46, 2005.
- [33] M. Freitag, M. Klein, and J. Janicka. Numerical analysis of the modeling and numerical uncertainties in large eddy simulation using upwind-biased numerical schemes, January 2007.
- [34] J. Fröhlich. *Large Eddy Simulation turbulenter Strömungen*. B. G. Teubner Verlag, Wiesbaden, 2006.
- [35] M. Germano, U. Piomelli, P. Moin, and W. H. Cabot. Dynamic subgrid-scale eddy viscosity model. *Phys. Fluids A*, 3(7):1760–1765, 1991.
- [36] F. Hahn, C. Olbricht, and J. Janicka. Large eddy simulation of an evaporating spray based on an eulerian-lagrangian approach. In *Proc. ILASS 8-10 Sep. Como Lake, Italy*, pages ILASS08–2–9, 2008.
- [37] Y. Hardalupas, A. M. K. P. Taylor, and J. H. Whitelaw. Velocity and particle flux characteristics of turbulent particle-laden jets. *Proc. R. Soc. Lond. A*, 426:31–78, 1989.
- [38] J. O. Hinze. *Turbulence, 2nd ed.* McGraw-Hill, New York, NY, 1975.
- [39] A. T. Hjelmfelt and L. F. Mockros. Motion of discrete particles in a turbulent fluid. *App. Sci. Research*, 16:149–161, 1966.
- [40] D. G. Holmes and S. D. Conell. Solution of the 2d Navier-Stokes equations on unstructured adaptive grids. In *AIAA 9th Computational Fluid Dynamics Conference*, 1989.
- [41] S. James, J. Zhu, and M. S. Anand. Large eddy simulations as a design tool for gas turbine combustion systems. *AIAA J.*, 44:674–686, 2006.
- [42] J. Janicka and A. Sadiki. Large eddy simulation for turbulent combustion systems. *Proc. Comb. Inst.*, 30:573–547, 2005.
- [43] S.-E. Kim and B. Makarov. An implicit fractional-step method for efficient transient simulation of incompressible flows. In *17th AIAA Computational Fluid Dynamics Conference, June 6–9, Toronto Ontario*, pages AIAA Paper 2005–5253, 2005.
- [44] A. N. Kolmogorov. Local structure of turbulence in incompressible viscous fluid for very large reynolds number. *Dokladi Akademiyi Nauk SSSR*, 30:299–303, 1941.
- [45] H. Kuerten and A.W. Vreman. Can turbophoresis be predicted by large-eddy simulation? *Phys. Fluids*, 17:011701, 2005.

- [46] J. G. M. Kuerten. Subgrid modeling in particle-laden channel flow. *Phys. Fluids*, 18: 025108, 2006.
- [47] J. D. Kulick, J. R. Fessler, and J. K. Eaton. On the interactions between particles and turbulence in a fully-developed channel flow in air. Mech. Engng. Rep. MD-66, Stanford Univ., 1993.
- [48] J. D. Kulick, J. R. Fessler, and J. K. Eaton. Particle response and turbulence modification in fully developed channel flow. *Journal of Fluid Mechanics*, 277:109–134, 1994.
- [49] K. Lam and S. Banerjee. On the condition of streak formation in bounded flows. *Phys. Fluids A*, 4:306–320, 1992.
- [50] B. P. Leonard. The ultimate conservative difference scheme applied to unsteady one-dimensional advection. *Comp. Methods Appl. Mech. Eng.*, 88:17–74, 1991.
- [51] D. K. Lilly. A proposed modification of the germano subgrid-scale closure model. *Phys. Fluids*, 4:633–635, 1992.
- [52] E. K. Longmire and J. K. Eaton. Structure of a particle-laden round jet. *J. Fluid Mech.*, 236:217–257, March 1992.
- [53] C. Marchioli and A. Soldati. Mechanisms for particle transfer and segregation in a turbulent boundary layer. *J. Fluid Mech.*, 468:283–315, 2002.
- [54] C. Marchioli and A. Soldati. Dns of particle-laden turbulent channel flow. *Proc. 11th Workshop on Two-Phase Flow Predictions, Merseburg, Germany*, 2005.
- [55] Ch. Marchioli, M. Picciotto, and A. Soldati. Particle dispersion and wall-dependent turbulent flow scales: implications for local equilibrium models. *J. Turb.*, 7:DOI: 10.1080/14685240600925171, 2006.
- [56] Ch. Marchioli, A. Soldati, J. G. M. Kuerten, B. Arcen, A. Tanière, G. Goldensohn, K. D. Squires, M. F. Cargnelutti, and L. M. Portela. Statistics of particle dispersion in direct numerical simulations of wall-bounded turbulence: Results of an international collaborative benchmark test. *Int. J. Multiphase Flow*, 34:879–893, 2008.
- [57] M. Masoudi and W. A. Sirignano. Nonlinear capillary waves on swirling, axisymmetric free liquid films. *Int. J. Multiphase Flow*, 27:1707–1734, 2001.
- [58] F. Mathey and D. Cokljat. Assessment of the vortex method for large-eddy simulation inlet conditions. *Prog. Comp. Fluid Dyn.*, 6:58–67, 2006.
- [59] S. R. Mathur and J. Y. Murthy. A pressure-based method for unstructured meshes. *Num. Heat Trans.*, 31:195–215, 1997.
- [60] R. Mei. An approximate expression for the shear lift force on a spherical particle at finite reynolds number. *Int. J. Multiphase Flow*, 18:145–147, 1992.
- [61] P. Moin and S. V. Apte. Large eddy simulation of realistic gas turbine combustor. *AIAA J.*, 44:698–708, 2006.

-
- [62] S. A. Morsi and A. J. Alexander. An investigation of particle trajectories in two-phase flow systems. *J. Fluid Mech.*, 55:193–208, 1972.
- [63] R. D. Moser, J. Kim, and N. N. Mansour. Direct numerical simulation of turbulent channel flow up to $Re_\tau = 590$. *Phys. Fluids*, 11:943–945, 1999.
- [64] F. Odar and W. S. Hamilton. Forces on a sphere accelerating in a viscous fluid. *J. Fluid Mech.*, 18:302–314, 1964.
- [65] J. C. Oefelein. *Simulation and Analysis of Turbulent Multiphase Combustion at High Pressures*. PhD thesis, The Pennsylvania State University, 1997.
- [66] C. Olbricht. *Numerische Verbrennung technischer Verbrennungssysteme*. PhD thesis, TU Darmstadt, 2009.
- [67] A. D. Paris. *Turbulence Attenuation in a Particle-Laden Channel Flow*. PhD thesis, Stanford University, 2001.
- [68] S. V. Patankar. *Numerical Heat Transfer and Fluid Flow*. DC, Hemisphere, Washington, 1980.
- [69] N. Peters. *Turbulent Combustion*. Cambridge University Press, 2000.
- [70] M. Picciotto, C. Marchioli, M. W. Reeks, and A. Soldati. Statistics of velocity and preferential accumulation of micro-particles in boundary layer turbulence. *Nucl. Eng. Design*, 235:1239–1249, 2005.
- [71] C. Pierce and P. Moin. A dynamic model for subgrid variance and dissipation rate of a conserved scalar. *Phys. Fluids*, 10:3041–3044, 1998.
- [72] H. Pitsch. Large-eddy simulation of turbulent combustion. *Ann. Rev. Fluid Mech.*, 38: 453–482, 2006.
- [73] S. B. Pope. *Turbulent Flows*. Cambridge Univ. Press, 2001.
- [74] J. Pozorski and S. V. Apte. Filtered particle tracking in isotropic turbulence and stochastic modeling of subgrid–dispersion. *Int. J. Multiphase Flow*, 35:118–128, 2009.
- [75] L. Prandtl. über die ausgeprägte turbulenz. *Z. Angew. Math. Mech.*, 5:136–139, 1925.
- [76] H.-H Qiu and M. Sommerfeld. A reliable method for determining the measurement volume size and particle mass fluxes using phase-doppler anemometry. *Exp. Fluids*, 13: 393–404, 1992.
- [77] W. E. Ranz and W. R. Marshall Jr. Evaporation from drops, part i. *Chem. Eng. Prog.*, 48(3):141 – 146, 1952.
- [78] W. E. Ranz and W. R. Marshall Jr. Evaporation from drops, part ii. *Chem. Eng. Prog.*, 48(4):173 – 180, 1952.

- [79] C. M. Rhie and W. L. Chow. Numerical study of the turbulent flow past an airfoil with trailing edge separation. *AIAA J.*, 21:1525–1532, 1983.
- [80] E. Riber, V. Moureau, M. Garcia, T. Poinso, and O. Simonin. Evaluation of numerical strategies for large eddy simulation of particulate two-phase recirculating flows. *J. Comp. Phys.*, doi:10.1016/j.jcp.2008.10.001, 2008.
- [81] L. F. Richardson. *Weather Prediction by Numerical Process*. Cambridge Univ. Press, 1922.
- [82] S. I. Rubinow and J. B. Keller. The transverse force on spinning sphere moving in a viscous fluid. *J. Fluid Mech.*, 11:447–459, 1961.
- [83] R. R. Rudoff and W. D. Bachalo. Measurements of droplet drag coefficients in polydispersed turbulent flow field. *AIAA*, pages 80–0235, 1988.
- [84] G. R. Ruetsch and M. R. Maxey. The evolution of small-scale structures in homogeneous turbulence. *Phys. Fluids A*, 4:2747, 1992.
- [85] G. G. Saffman. The lift on a small sphere in a slow shear flow. *J. Fluid Mech.*, 22:385–400, 1965.
- [86] P. Sagaut. *Large Eddy Simulation of Incompressible Flows*. Springer, 2001.
- [87] O. Sawatzki. Strömungsfeld um eine rotierende kugel. *Acta Mechanica*, 9:159–214, 1970.
- [88] L. Schiller and Z. Naumann. A drag coefficient correlation. *VDI Zeitschrift*, 77:318, 1935.
- [89] H. Schlichting and K. Gersten. *Grenzschicht-Theorie*. Springer Verlag, Berlin, Heidelberg, 9. Aufl. edition, 1997.
- [90] U. Schuman. Subgrid scale model for finite difference simulations of turbulent flows in plane channels and annuli. *J. Comp. Phys.*, 18:376–404, 1975.
- [91] J. C. Segura. *Predictive Capabilities of Particle-Laden Large Eddy Simulation*. PhD thesis, Dep. Mech. Eng., Stanford University, 2004.
- [92] W. A. Sirignano. *Fluid Dynamics and Transport of Droplets and Sprays*. Applied Mathematical Sciences 135. Cambridge University Press, New York, 2005.
- [93] J. Smagorinsky. General circulation experiments with the primitive equations. i. the basic experiment. *Month. Wea. Rev.*, 91:99–164, 1963.
- [94] W. H. Snyder and J. L. Lumley. Some measurements of particle velocity autocorrelation functions in a turbulent flow. *J. Fluid Mech.*, 48:41–71, 1971.
- [95] M. Sommerfeld. Modellierung und numerische berechnung von partikelbeladenen turbulenten strömungen mit hilfe des euler/lagrange-verfahrens. *Int. J. Heat Fluid Flow*, 19:10–22, 1998.

-
- [96] M. Sommerfeld. Theoretical and experimental modelling of particulate flows. Technical Report Lecture Series 2000-06, von Karman Institute for Fluid Dynamics, 2000.
- [97] M. Sommerfeld and H. H. Qiu. Particle concentration measurements by phase-doppler anemometry in complex dispersed two-phase flows. *Exp. Fluids*, 18:187–198, 1995.
- [98] M. Sommerfeld and H. H. Qiu. Spray evaporation in turbulent flow, 1998. URL [http://www-mvt.iw.uni-halle.de/index.php?spray_evaporation\\$](http://www-mvt.iw.uni-halle.de/index.php?spray_evaporation$). Data base.
- [99] M. Sommerfeld and H. H. Qiu. Experimental studies of spray evaporation in turbulent flow. *Int. J. Heat Fluid Flow*, 19:10–22, 1998.
- [100] K. D. Squires and J. K. Eaton. Preferential concentration of particles by turbulence. *Phys. Fluids A*, 3:1169–1178, 1991.
- [101] G. G. Stokes. On the effect of the inertial friction of fluids on the motion of pendulumus. *Trans. Cambr. Phil. Soc.*, 9:8–106, 1851.
- [102] L. Tang, F. Wen, Y. Yang, C. T. Crowe, J. N. Chung, and T. R. Troutt. Self-organizing particle dispersion mechanism in a plane wake. *Phys. Fluids A*, 4:2244–2251, 1992.
- [103] L. B. Torobin and W. H. Gauvin. The drag coefficient of single sphere moving in steady and accelerated motion in a turbulent fluid. *AIChE J.*, 7:615–619, 1961.
- [104] C. Truesdell and R. Toupin. *The Classical Field Theories*, volume III of *Handbuch der Physik*, chapter 1 Part. Springer Verlag, Berlin, 1960.
- [105] P. H. T. Uhlherr and C. G. Sinclair. The effect of free stream turbulence on the drag coefficient of spheres. *Proc. Chemca '70*, 1:1, 1970.
- [106] VDI-Gesellschaft Verfahrenstechnik und Chemieingenieurwesen (Hrsg.). *VDI-Wärmeatlas : Berechnungsblätter für den Wärmeübergang*. Springer Verlag, Berlin, 2002.
- [107] M. Vance, K. W. Squires, , and O. Simonin. Properties of the particle velocity field in gas-solid turbulent channel flow. *Phys. Fluids*, 18:063302, 2006.
- [108] N. B. Vargaftik. *Handbook of Physical Properties of Liquids and Gases*. Taylor & Francis Inc., 2nd edition, 1983.
- [109] A. W. Vreman. Turbulence characteristics of particle-laden pipe flow. *J. Fluid Mech.*, 584:235–279, 2007.
- [110] A. W. Vreman, B. J. Geurts, N. G. Deen, and J. A. M. Kuipers. Large-eddy simulation of a particle-laden turbulent channel flow. *Direct and Large-Eddy Simulation, R. Friedrich et al. (eds.)*, 5:271–278, 2004.
- [111] L. P. Wang and M. R. Maxey. Settling velocity and concentration distribution of heavy particles in homogeneous isotropic turbulence. *J. Fluid Mech.*, 256:27–68, 1993.

- [112] Q. Wang and K. D. Squires. Large-eddy simulation of particle-laden turbulent channel flow. *Phys. Fluids*, 8:1207–1223, 1996.
- [113] B. Wegner. *A Large-Eddy Simulation Technique for the Prediction of Flow, Mixing and Combustion in Gas Turbine Combustors*. PhD thesis, TU Darmstadt, 2006.
- [114] D. C. Wilcox. *Turbulence Modeling for CFD*. D C W Industries, 2000.
- [115] Y. Yamamoto, M. Potthoff, T. Tanaka, T. Kajishima, and Y. Tsuji. Large-eddy simulation of turbulent gas-particle flow in a vertical channel: Effect of considering inter-particle collisions. *J. Fluid Mech.*, 442:303–334, 2001.
- [116] J. Young and A. Leeming. A theory of particle deposition in turbulent pipe flow. *J. Fluid Mech.*, 340:129–159, 1997.
- [117] N. A. Zarin and J. A. Nicholls. Sphere drag in solid rockets - non continuum and turbulence effects. *Comb. Sci. Tech.*, 3:273, 1971.

Lebenslauf

Name	Desislava Nikolova Dimitrova	
Geburtsort	Haskovo, Bulgarien	
Schulbildung	09 / 1992 – 06 / 1997	Fremdsprachengymnasium "Prof. Dr. A. Zlatarov"
Studienkolleg	09 / 1997 – 08 / 1998	Technische Universität Sofia
Studium	09 / 1998 – 08 / 2001	Technische Universität Sofia Fachrichtung: Allgemeiner Maschinenbau
	10 / 2001 – 12 / 2004	Universität Karlsruhe (TH), (seit 2010 Karlsruhe Institute of Technology) Fachrichtung: Allgemeiner Maschinenbau Vertiefungsrichtung: Werkstoffkunde, Thermische Strömungsmaschinen
	12 / 2004	Abschluss zum Diplom-Ingenieur
Beruflicher Werdegang	02 / 2005 – 12 / 2010	Wissenschaftlicher Mitarbeiter, Technische Universität Darmstadt, Fachgebiet Energie- und Kraftwerkstechnik